



UPPSALA  
UNIVERSITET

*Digital Comprehensive Summaries of Uppsala Dissertations  
from the Faculty of Science and Technology 712*

# Computational Studies of Hydrogen Storage Materials

*Physisorbed and Chemisorbed Systems*

PORNJUK SREPUSHARAWOOT



ACTA  
UNIVERSITATIS  
UPSALIENSIS  
UPPSALA  
2010

ISSN 1651-6214  
ISBN 978-91-554-7933-6  
urn:nbn:se:uu:diva-132875

Dissertation presented at Uppsala University to be publicly examined in Å80101, Ångström Laboratory, Lagerhyddsvägen 1, Uppsala, Friday, December 10, 2010 at 10:15 for the degree of Doctor of Philosophy. The examination will be conducted in English.

### Abstract

Srepusharawoot, P. 2010. Computational Studies of Hydrogen Storage Materials. Physisorbed and Chemisorbed Systems. Acta Universitatis Upsaliensis. *Digital Comprehensive Summaries of Uppsala Dissertations from the Faculty of Science and Technology* 712. 90 pp. Uppsala. ISBN 978-91-554-7933-6.

This thesis deals with first-principles calculations based on density functional theory to investigate hydrogen storage related properties in various high-surface area materials and the ground state crystal structures in alkaline earth dicarbide systems.

High-surface area materials have been shown to be very promising for hydrogen storage applications owing to them containing numerous hydrogen adsorption sites and good kinetics for adsorption/desorption. However, one disadvantage of these materials is their very weak interaction with adsorbed hydrogen molecules. Hence, for any feasible applications, the hydrogen interaction energy of these materials must be enhanced. In metal organic frameworks, approaches for improving the hydrogen interaction energy are opening the metal oxide cluster and decorating hydrogen attracting metals, e.g. Li, at the adsorption sites of the host. In covalent organic framework-1, the effects of the H<sub>2</sub>-H<sub>2</sub> interaction are also found to play a significant role for enhancing the hydrogen adsorption energy. Moreover, *ab initio* molecular dynamics simulations reveal that hydrogen molecules can be trapped in the host material due to the blockage from adjacent adsorbed hydrogen molecules.

In light metal hydride systems, hydrogen ions play two different roles, namely they can behave as "promoter" and "inhibitor" of Li diffusion in lithium imide and lithium amide, respectively. By studying thermodynamics of Li<sup>+</sup> and proton diffusions in the mixture between lithium amide and lithium hydride, it was found that Li<sup>+</sup> and proton diffusions inside lithium amide are more favorable than those between lithium amide and lithium hydride.

Finally, our results show that the ground state configuration of BeC<sub>2</sub> and MgC<sub>2</sub> consists of five-membered carbon rings connected through a carbon atom forming an infinitely repeated chain surrounded by Be/Mg ions, whereas the stable crystal structure of the CaC<sub>2</sub>, SrC<sub>2</sub> and BaC<sub>2</sub> is the chain type structure, commonly found in the alkaline earth dicarbide systems.

**Keywords:** Density functional theory, Ab initio molecular dynamics, Ab initio random structure searching, Hydrogen storage materials, Alkaline earth dicarbide

*Pornjuk Srepusharawoot, Department of Physics and Astronomy, Materials Theory, Box 516, Uppsala University, SE-751 20 Uppsala, Sweden.*

© Pornjuk Srepusharawoot 2010

ISSN 1651-6214

ISBN 978-91-554-7933-6

urn:nbn:se:uu:diva-132875 (<http://urn.kb.se/resolve?urn=urn:nbn:se:uu:diva-132875>)

*To My Family*



# List of Papers

This thesis is based on the following papers, which are referred to in the text by their Roman numerals.

- I    **A comparative investigation of H<sub>2</sub> adsorption strength in Cd- and Zn-based metal organic framework-5**  
P. Srepusharawoot, C. Moysés Araújo, A. Blomqvist, R. H. Scheicher and R. Ahuja, *Journal of Chemical Physics* **129**, 164104 (2008).
- II   **Ab initio study of hydrogen adsorption in covalent organic framework - 1**  
P. Srepusharawoot, R. H. Scheicher, C. Moysés Araújo, A. Blomqvist, U. Pinsook and R. Ahuja, *Journal of Physical Chemistry C* **113**, 8498 (2009).
- III   **Li-decorated metal-organic framework 5: A route to achieving a suitable hydrogen storage medium**  
A. Blomqvist, C. Moysés Araújo, P. Srepusharawoot and R. Ahuja, *Proceedings of the National Academy of Science of the U.S.A.* **104**, 20173 (2007).
- IV   **Hydrogen binding in alkali-decorated iso-reticular metal organic framework-16 based on Zn, Mg, and Ca**  
P. Srepusharawoot, A. Blomqvist, C. Moysés Araújo, R. H. Scheicher and R. Ahuja, *International Journal of Hydrogen Energy*, in press (2010)
- V    **Hydrogen as promoter and inhibitor of superionicity: A case study on Li-N-H systems**  
A. Blomqvist, C. Moysés Araújo, R. H. Scheicher, P. Srepusharawoot, W. Li, P. Chen and R. Ahuja, *Physical Review B* **82**, 024304 (2010).
- VI   **Li<sup>+</sup> and H<sup>+</sup> diffusions in lithium amide and hydride: A first-principles study**  
P. Srepusharawoot, C. Moysés Araújo, R. H. Scheicher and R. Ahuja, *In manuscript*.
- VII   **One-dimensional polymeric carbon structure based on five-membered rings in alkaline earth metal dicarbides BeC<sub>2</sub> and MgC<sub>2</sub>**  
P. Srepusharawoot, A. Blomqvist, C. Moysés Araújo, R. H. Scheicher and R. Ahuja, *Physical Review B* **82**, 125439 (2010).

Reprints were made with permission from the publishers.

The following paper is co-authored by me but is not included in this thesis.

• **Application of entropy calculations to the determination of transition temperature in zirconium**

P. Srepusharawoot and U. Pinsook, *Physica Status Solidi B* **242**, 1598 (2005).

# Contents

<b>1</b>	<b>Introduction</b>	9
<b>2</b>	<b>Theoretical Backgrounds</b>	13
2.1	Density functional theory	13
2.1.1	Many body problem	13
2.1.2	The Hohenberg-Kohn theorems	15
2.1.3	Self-consistent Kohn-Sham equation	16
2.1.4	The secular equation	18
2.1.5	Periodic potential system	19
2.1.6	The PAW method	20
2.1.7	Force evaluation	22
2.1.8	<i>Ab initio</i> molecular dynamics	23
2.2	Møller-Plesset perturbation theory	25
2.2.1	Rayleigh-Schrödinger perturbation theory	26
2.2.2	Details of Møller-Plesset perturbation theory	28
<b>3</b>	<b>Hydrogen Storage in Physisorbed Systems</b>	31
3.1	Introduction	31
3.2	Hydrogen storage methods	32
3.2.1	Gaseous storage	32
3.2.2	Liquid storage	32
3.2.3	Solid-state storage	33
3.3	High-surface area materials	35
3.3.1	Metal organic framework -5	36
3.3.2	Covalent organic framework -1	40
3.3.3	Li decorations in metal organic framework -5	46
3.3.4	Alkali functionalization in metal organic framework-16	49
<b>4</b>	<b>Li-N-H Systems</b>	55
4.1	Roles of hydrogen in the Li-N-H system	55
4.2	Thermodynamics of $\text{Li}^+$ and $\text{H}^+$ migrations in $\text{LiNH}_2$	59
<b>5</b>	<b>Ab Initio Random Structure Searching</b>	63
5.1	Alkaline earth dicarbide systems	65
5.1.1	Stability of alkaline earth dicarbide	66
5.1.2	Reaction paths of beryllium and magnesium dicarbide	69
5.1.3	Density of states of beryllium and magnesium dicarbide	70
<b>6</b>	<b>Sammanfattning på Svenska</b>	73
	Acknowledgements	77
	Bibliography	79





# 1. Introduction

Nowadays, computational materials science plays a significant role as a powerful tool for developing new materials in several areas of materials science. It numerically solves various observable quantities of the important materials at atomic level based on the multidisciplinary theoretical concepts. The major advantages of the computational materials science help us to understand atomic behavior in the large class of molecules or solids through theoretical interpretations. In addition, some conditions which are difficult to reach in experiments such as extreme conditions can also be simulated prior to launching the experiment. However, one important factor that should be critically considered in the computational materials science is the “accuracy” of the simulation results. Previously, classical simulations i.e. Newtonian mechanics were successfully shown to be powerful tools in computational materials science because they work well for very large system (order of million atoms), however, the accuracy of these simulations is still problematic. Currently, first-principles methods have been shown to be suitable methods for studying at atomic scale and producing more accurate results compared to the classical methods. In addition, the advancement in computing power leads to possibility to simulate rather large system in which the maximum number of atom is in order of several thousand atoms. Based on these reasons, first-principles methods based on e.g. density functional theory, Møller-Plesset perturbation theory and so on are suitable and accurate choices for studying the nanoscale systems.

In the twentieth century, most of energy supply comes mainly from the fossil fuel based resources e.g. crude oil. Unfortunately, these resources can produce the harmful gases such as CO, CO<sub>2</sub> and SO<sub>2</sub> to the atmosphere resulting in the environmental problems. In addition, tremendous usages of fossil energy resources mainly from transportations and industries lead to depletion of the currently used energy resource. Hydrogen economy is offered as one of the most interesting solution for the future energy resources owing to very abundant element on the earth (in form of water) and pollution-free product. Another reason regarding to hydrogen economy as a promising energy resource is that the mass energy density is higher than that of the current fossil fuels for about three times [1–4]. Although, the volumetric density of hydrogen is indeed low, namely 0.09 kg/m<sup>3</sup> for H<sub>2</sub> gas [5], and therefore large amount of space is needed to store hydrogen. Hence, the hydrogen storage problem is encountered.

To keep hydrogen in the hydrogen storage medium, three important methods are briefly discussed in the follows. Originally, gaseous hydrogen is stored in the high pressure containers. However, this storage method leads to several drawbacks e.g. safety concerns, cost of pressurization, hydrogen embrittlement of hydrogen tank and suddenly drop of pressure during use [6]. Due to these disadvantages, pressurized hydrogen in the container is an inappropriate choice to use as a hydrogen storage medium. The second option for storing hydrogen in the medium is to keep hydrogen in liquid state (with density  $70.8 \text{ kg/m}^3$  at 21 K [5, 7]). Although, the liquid hydrogen can only be existed at cryogenic condition i.e. between 21 – 32 K at ambient pressure [7]. Consequently, a well-shielded vessel is required in order to protect the leakage of liquid hydrogen (about 2-3 % per day for hydrogen vaporization [7, 8]). In addition, the energy needed for cooling the hydrogen to be in the liquid state is about one-third of the total stored energy [9]. Hence storing liquid hydrogen in the medium is not such a good choice as hydrogen storage medium due to these economic issues.

The most promising option for hydrogen storage medium is to keep hydrogen in the suitable solid-state materials so called “solid-state storage”. For this option, hydrogen can be trapped in the materials based on two different mechanisms, namely physisorption and chemisorption. In nature, hydrogen is formed as a molecule. When hydrogen molecules approach to the host material’s surface, they adhere to the surface via weak dispersive interaction or van der Waals interaction [10] and this mechanism is called “physisorption”. Usually, the hydrogen adsorption energy of this mechanism is very weak, namely less than 10 kJ/mol and this results in fast kinetic because of very easy for hydrogen adsorption/desorption. Moreover, several works found that higher surface area materials can yield to higher hydrogen capacity. Consequently, high-surface area materials, for instance metal organic frameworks [11], covalent organic frameworks [12, 13], carbon based materials [14, 15] etc. show to be the promising hydrogen storage materials. However, the major obstacle to use these materials for the hydrogen storage purpose is that mostly hydrogen molecules are desorbed at ambient condition due to very weak interaction between  $\text{H}_2$  and host framework and this results in a rather low hydrogen gravimetric density at this condition. Currently, several approaches such as decorating hydrogen attracting metals [16, 17], catenation [18] and spillovers [19] are used for improving the hydrogen strengthen in the physisorbed systems. Although, the enhanced hydrogen binding energies from these methods are still not satisfied the hydrogen storage requirement for practical applications. Another strategy in the solid-state storage is that hydrogen atoms are trapped in the host framework in form of hydride compound and this approach is called “chemisorption”. In the chemisorption, hydrogen molecules are initially dissociated at the host material’s surface and then atomic hydrogen diffuse into the material to form a hydride when the fully hydrogenated state is reached. However, common drawbacks of the chemisorption materials

are rather high desorption temperature and slow reversibility for the absorption/desorption process due to rather difficult to break the strong ionic or covalent bond between atomic hydrogen and host material for releasing hydrogen. These problems can be improved by doping catalyst or reducing the grain size to nanoscale in order to enhance the adsorption and desorption kinetics [20]. Examples of the chemisorption materials are hydrogen rich compounds such as metal hydride ( $\text{MgH}_2$ ) [21], alanates ( $\text{NaAlH}_4$ ,  $\text{LiAlH}_4$ ) [22, 23], borates ( $\text{LiBH}_4$ ) [24, 25] and Li-N-H systems [26].

In *ab initio* calculations, it is very important for us to know the crystal structure at a particular condition in order to use it as an input for evaluating the quantities of interest. Hence the precision of the initial crystal structure is a very important parameter dealing to accuracy of the simulation results. To obtain the correct crystal structure at a particular condition, several conventional methods such as energy minimization, molecular dynamics and simulated annealing simulations are employed. However, the main disadvantage of these techniques is that very long simulation times to evolve from one local minimum to global minimum is needed resulting in very large consumption in both computational time and resources. Moreover, it is very tough for one to reach the global minimum point for complex system because the number of local minima in the potential energy surface are proportional to number of atoms [27]. Currently, a powerful method so called “*ab initio* random structure searching” or AIRSS was proposed for crystal structure determination [28–30]. This technique is based on a simple strategy that numerous numbers of crystal structures are randomly generated and the ground state configuration is the lowest enthalpy configuration. The AIRSS has usually been used to determine the stable configuration at high pressure phases of various systems, for example silane [28], solid hydrogen [29], ammonia [30], water [31], nitrogen [32], graphite intercalation compound [33], lithium-beryllium alloys [34], tellurium dioxide [35], iron [36] etc.

The outlines for the present thesis are as follows. In chapter 2, the basic concepts of all theoretical backgrounds, namely density functional theory, *ab initio* molecular dynamics method and Møller-Plesset perturbation theory are briefly discussed. In the third chapter, hydrogen storage concepts and the related hydrogen storage properties in the physisorbed systems especially metal organic frameworks and covalent organic frameworks are presented. In addition, functionalized alkali metals into both metal organic framework-5 and metal organic framework-16 are also considered by us. In chapter 4, diffusions of lithium in the Li-N-H systems [26], namely lithium nitride, lithium imide and lithium amide are discussed. Moreover, thermodynamics of  $\text{Li}^+$  and proton diffusions in the mixture between lithium amide and lithium hydride are also considered. Finally, the basic idea of the AIRSS and its application for determining the ground state configurations of the alkaline earth dicarbide systems are explained in chapter 5.



## 2. Theoretical Backgrounds

In this chapter, all theoretical backgrounds used for all of works in this thesis are discussed. In Section 2.1, the major technique used in the most part of this thesis so called “Density Function Theory” will be extensively discussed. Moreover, detailed description of the Møller-Plesset perturbation theory (MP) will be explained in Section 2.2.

### 2.1 Density functional theory

Here, we start with the introduction of many body problem and then goes to the concepts of density functional theory such as the Hohenberg-Kohn theorems and Kohn-Sham equation. In addition, an projector augmented wave approach and the method for evaluating force acting between each ion so called Hellmann-Feymann theorem are explained. Lastly, the *ab initio* molecular dynamics and their physical quantities obtained from this simulation e.g. mean square displacement (MSD), radial distribution function (RDF), bond angle distribution (BAD) and hydrogen density distribution are considered.

#### 2.1.1 Many body problem

In reality, we always deal with the systems containing large number of atoms ( $\approx 10^{23}$  atoms) and hence we can not escape from the many body problems. For many body problem, we focus only on solid containing of  $10^{23}$  atoms. In solid, it contains many electrons and nuclei and the behavior of these particles must be obeyed the time-independent Schrödinger equation

$$\mathcal{H}\Psi(\mathbf{r}, \mathbf{R}) = \mathcal{E}\Psi(\mathbf{r}, \mathbf{R}),$$

where  $\mathcal{H}$ ,  $\mathcal{E}$  and  $\Psi(\mathbf{r}, \mathbf{R})$  are the Hamiltonian, energy eigenvalue and wave function of solid which is related to the probability to find an electron at position  $\mathbf{r}$  and nucleus at position  $\mathbf{R}$ , respectively. In this case, we assume that solid consists of  $N_e$  electrons and  $N_{nuc}$  nuclei and the Hamiltonian of solid can

be written as

$$\begin{aligned}\mathcal{H} = & \sum_{i=1}^{N_e} -\frac{\hbar^2}{2m} \nabla_i^2 + \sum_{I=1}^{N_{nuc}} -\frac{\hbar^2}{2M} \nabla_I^2 + \frac{1}{2} \sum_{i \neq j} \frac{e^2}{|\mathbf{r}_i - \mathbf{r}_j|} \\ & - \sum_{i,I} \frac{Z_I e^2}{|\mathbf{r}_i - \mathbf{R}_I|} + \frac{1}{2} \sum_{I \neq J} \frac{Z_I Z_J e^2}{|\mathbf{R}_I - \mathbf{R}_J|}.\end{aligned}\quad (2.1)$$

The first two terms are the kinetic energy of electrons and nuclei, respectively, and the last three terms refer to the electron-electron interactions, electron-nucleus interactions and nucleus-nucleus interactions.  $\hbar = \frac{h}{2\pi}$ ,  $m$  and  $M$  are the reduced Planck's constant, electron and nucleus mass, respectively.  $Z_I$  is the atomic number of the  $I^{th}$  nucleus,  $e$  is the electron charge and  $\mathbf{r}_i$  and  $\mathbf{R}_I$  are symbolized as the positions of the  $i^{th}$  electron and  $I^{th}$  nucleus. However, it is practically impossible to solve Eq. 2.1 for real solid which has an enormous number of electrons and nuclei. This problem however, can be simplified by using the Born-Oppenheimer approximation. In this approximation, the nuclei are treated as stationary and the electrons move around the nuclei. This is because electrons move faster than nuclei for about two orders of magnitude and hence the kinetic energy of nuclei can be negligible. Moreover, mass of the nuclei is much heavier than that of electron. Consequently, the last term in the Eq. 2.1 can be set to be constant. The Hamiltonian of solid is reduced to

$$\mathcal{H} = \sum_{i=1}^{N_e} -\frac{\hbar^2}{2m} \nabla_i^2 + \frac{1}{2} \sum_{i \neq j} \frac{e^2}{|\mathbf{r}_i - \mathbf{r}_j|} - \sum_{i,I} \frac{Z_I e^2}{|\mathbf{r}_i - \mathbf{R}_I|} + \frac{1}{2} \sum_{I \neq J} \frac{Z_I Z_J e^2}{|\mathbf{R}_I - \mathbf{R}_J|}.\quad (2.2)$$

According to the Born-Oppenheimer approximation, we can explicitly separate the electron and nucleus motion. Hence, the solid wave function can be divided independently into an electron part,  $\Psi_e(\mathbf{r}, \mathbf{R})$ , and a nucleus part,  $\Psi_N(\mathbf{R})$ , as

$$\Psi(\mathbf{r}, \mathbf{R}) = \Psi_e(\mathbf{r}, \mathbf{R}) \Psi_N(\mathbf{R}).$$

The effect from nuclei in electronic problem can be omitted because electron behavior plays an important role in this problem. However, nucleus wave function is able to be added later if our observable properties are related to nuclei. For electrons, the Schrödinger equation can be written as

$$\mathcal{H}_e \Psi_e(\mathbf{r}, \mathbf{R}) = \mathcal{E}_e \Psi_e(\mathbf{r}, \mathbf{R}),$$

where

$$\mathcal{H}_e = \sum_{i=1}^{N_e} -\frac{\hbar^2}{2m} \nabla_i^2 + \frac{1}{2} \sum_{i \neq j} \frac{e^2}{|\mathbf{r}_i - \mathbf{r}_j|} - \sum_{i,I} \frac{Z_I e^2}{|\mathbf{r}_i - \mathbf{R}_I|},\quad (2.3)$$

$\Psi_e(\mathbf{r}, \mathbf{R})$  and  $\mathcal{E}_e$  are the electron wave function and eigenvalues, respectively.

To solve many-electron problems, single electron wave function was initially used for solving Eq. 2.3. In Hatree theory [37], many-electron wave function can be obtained from a product of single-electron wave functions. However, this theory fails to understand electronic properties due to violating the antisymmetric property of the wave functions. An improvement from the Hartree theory is the Hartree-Fock (HF) theory. In the HF theory, the HF wave function was proposed as a determinant of single electron wave functions called “Slater determinant”, explicitly including the antisymmetric property of the wave function. Moreover, the exchange interaction is automatically included in the electron Hamiltonian. Although, this theory has various deficiencies, for example, it excludes correlation effects such as screening effects and so on. In addition, this method is not suitable for using with a large number of electrons due to consumption of large memory resources and computational expensive as well. From all of these drawbacks, density functional theory (DFT) is presented as an appropriate tool for solving the many electron problem. In the followings, a detailed description of the DFT will be discussed.

### 2.1.2 The Hohenberg-Kohn theorems

DFT is a popular method for solving many body problems. In principle, this method is an exact method but, in practical, it uses some approximations for exchange-correlation function. The starting point of this theory comes from the Hohenberg-Kohn theorem [38] consisting of two theorems.

**Theorem 1** For any system of interacting particles in an external potential,  $V_{ext}(\mathbf{r})$ , there is a one to one correspondence between the external potential and ground state density ( $n_0(\mathbf{r})$ ). Moreover, the ground state expectation value of any observable quantity  $A$  is a unique function.

$$\langle \Psi | \hat{A} | \Psi \rangle = A[n_0(\mathbf{r})].$$

This theorem implies that the density parameter is the main variable for DFT instead of the wave function for HF theory.

**Theorem 2** For any external potential applied to an interacting particle system, it is possible to define an universal total energy functional of the particle density, which is written as

$$\mathcal{E}[n(\mathbf{r})] = E_{HK}[n(\mathbf{r})] + \int V_{ext}(\mathbf{r})n(\mathbf{r}) d\mathbf{r},$$

where  $E_{HK}$  is the universal constant which does not relate to any information of the type of nuclei or their positions. This means that it is represented as an arbitrarily universal constant for the interacting system. However, this constant is still unknown. If knowing this constant, we can determine the ground state energy by minimizing total energy with respect to density by using the

variational principle,

$$\left. \frac{\delta \mathcal{E}[n(\mathbf{r})]}{\delta n} \right|_{n=n_0} = 0.$$

The exact ground state energy ( $\mathcal{E}_0$ ) corresponding to the ground state density  $n_0(\mathbf{r})$  is given by

$$\mathcal{E}_0 = \mathcal{E}[n_0(\mathbf{r})].$$

### 2.1.3 Self-consistent Kohn-Sham equation

According to the Hohenberg-Kohn theorem, the density is used as a primary quantity for calculating all observable quantities. Kohn and Sham [39] proposed a new Schrödinger-like equation, called “Kohn-Sham equation”, as a function of the density in 1965. Moreover, this equation maps an interacting system to a fictitious non-interacting system in which the particles moving in an effective field ( $V_{eff}$ ). The energy functional in the DFT can be written as

$$\begin{aligned} \mathcal{E}[n(\mathbf{r})] = & T_0[n(\mathbf{r})] + \frac{1}{2} \int \int \frac{n(\mathbf{r})n(\mathbf{r}')}{|\mathbf{r} - \mathbf{r}'|} d\mathbf{r} d\mathbf{r}' \\ & + \int V_{ext}(\mathbf{r})n(\mathbf{r}) d\mathbf{r} + E_{xc}[n(\mathbf{r})]. \end{aligned} \quad (2.4)$$

The first, second, third and fourth terms of Eq. 2.4 are the non-interacting kinetic energy functional ( $T_0[n(\mathbf{r})]$ ), the electron-electron interaction energy or Hartree energy, the external potential energy due to nuclei and exchange-correlation energy, respectively. By minimizing of Eq. 2.4 with respect to the density, the Kohn-Sham equation (in atomic unit) can be obtained as

$$\left[ -\frac{\nabla_i^2}{2} + V_{eff}(\mathbf{r}) \right] \Psi_i(\mathbf{r}) = \mathcal{E}_i \Psi_i(\mathbf{r}). \quad (2.5)$$

Where the effective potential is given by

$$V_{eff}(\mathbf{r}) = V_{ext}(\mathbf{r}) + V_{hartree}[n(\mathbf{r})] + V_{xc}[n(\mathbf{r})], \quad (2.6)$$

with  $V_{hartree}[n(\mathbf{r})] = \int \frac{n(\mathbf{r}')}{|\mathbf{r} - \mathbf{r}'|} d\mathbf{r}'$  and  $V_{xc}[n(\mathbf{r})] = \frac{\delta E_{xc}[n(\mathbf{r})]}{\delta n}$ .  $\Psi_i(\mathbf{r})$  is the Kohn-Sham orbital which is not the wave function of the system but the density obtained from the Kohn-Sham orbitals is the exact density as the true system. To solve the Kohn-Sham equation, algorithm for solving the self-consistent Kohn-Sham equation is well described in Figure 2.1. First, the density is initially guessed and then the effective potential functional (Eq. 2.6) is calculated from the guessed density. Next, the Kohn-Sham equation is solved in order to get the total energies and the Kohn-Sham orbitals. After that the new density can be obtained from the calculated



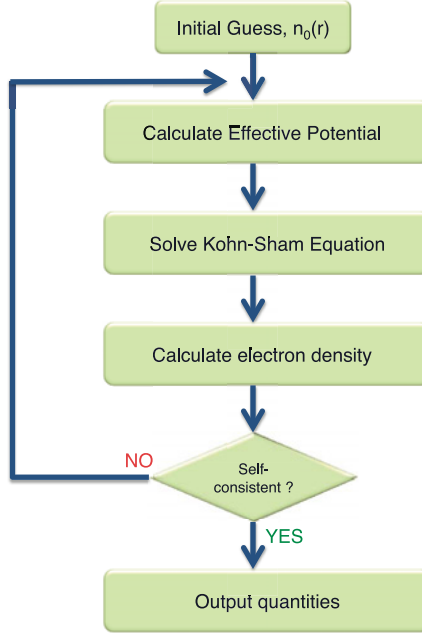


Figure 2.1: Schematic methods for solving self-consistent Kohn-Sham equation adapted from Ref. 40.

Kohn-Sham orbitals and is used as the initial density for the next step. This process runs self-consistently until the convergence of density is reached. Finally, the output quantities are calculated via the converged density.

From Eq. (2.6), the first two terms of the effective potential can be exactly evaluated where the last term ( $V_{xc}[n(\mathbf{r})]$ ) is still unknown. The  $V_{xc}[n(\mathbf{r})]$  contains all unknown terms i.e. many body effect of kinetic energy, correlation effects, etc. Based on the conventional exchange-correlation function, two types of  $E_{xc}$ , namely the Local Density Approximation (LDA) and Generalized Gradient Approximation (GGA) are considered. The exchange-correlation functional can be expressed as

$$E_{xc}[n(\mathbf{r})] = \int_{xc}[n(\mathbf{r})]n(\mathbf{r})d\mathbf{r}$$

where  $_{xc}[n(\mathbf{r})]$  is exchange-correlation density corresponding to the density  $n(\mathbf{r})$ .

### Local density approximation

In the LDA scheme, the exchange-correlation function is derived from the homogeneous interacting electron gas [40, 41]. It works very well for slow varying density, for instance, free electron-like system. Moreover, it can well describe for some other systems i.e. semiconductors and insulators. In metal

organic framework-5 and covalent organic framework-1, they can be surprisingly reproduced the correct trends of the hydrogen adsorption energies obtained from experiment and Møller-Plesset perturbation theory, whereas other exchange-correlation functionals such as GGA with PW91 [42] and PBE [43–45] functionals fail to predict the correct trend of hydrogen physisorption energies [46].

### Generalized gradient approximation

In real systems, the electron density is no longer homogeneous and hence the LDA scheme will be not well described in many cases. There are however, many attempts to improve the LDA by including higher-order terms of the exchange-correlation energy. In the GGA, the exchange-correlation energy contains information from both density and gradient of density ( $\nabla n$ ). By using this idea, many types of GGA functional have been created such as PW91 [42] and PBE [43–45]. In principle, the GGA potential should give a better result compared to LDA because it contains more information of the electron density. However, in practice, it is not always true that the GGA gives a better result than the LDA. There is an attempt to improve the exchange-correlation functional so called hybrid functionals. Detail descriptions of hybrid functionals that are not discussed here are well described in Ref. 47. The examples of hybrid functionals are the B3LYP [48, 49] and B97 [47] and so on.

#### 2.1.4 The secular equation

One important step for the DFT calculations (see Figure 2.1) is a method to solve the Kohn-Sham equation. The method for obtaining the solutions of the Kohn-Sham equation is described as follows. First of all, the Kohn-Sham orbitals are expanded as a linear combination of arbitrary basis functions,  $\varphi_i(\mathbf{r})$ , as

$$\Psi_n(\mathbf{r}) = \sum_{i=1}^Q C_i^n \varphi_i(\mathbf{r}), \quad (2.7)$$

where  $C_i^n$  are sets of coefficients. In principle, we should use  $Q$  to be infinity but, in practice,  $Q$  is always set to be as large as possible in order to increase the accuracy of the Kohn-Sham orbitals. Next, the Kohn-Sham orbitals are substituted into the Kohn-Sham equation (Eq. 2.5) and we get

$$\sum_{i=1}^Q C_i^n \left[ -\frac{\nabla_i^2}{2} + V_{eff}(\mathbf{r}) \right] \varphi_i(\mathbf{r}) = \sum_{i=1}^Q C_i^n \mathcal{E}_i \varphi_i(\mathbf{r}). \quad (2.8)$$

After multiplying Eq. 2.8 with the complex conjugate of the basis function,  $\varphi_j^*(\mathbf{r})$ , and integrating over all real space, we obtain

$$\sum_{i=1}^Q C_i^n \int \varphi_j^*(\mathbf{r}) \left[ -\frac{\nabla_i^2}{2} + V_{eff}(\mathbf{r}) \right] \varphi_i(\mathbf{r}) d\mathbf{r} = \sum_{i=1}^Q C_i^n \mathcal{E}_i \int \varphi_j^*(\mathbf{r}) \varphi_i(\mathbf{r}) d\mathbf{r}, \quad (2.9)$$

where the integral on the left handed side is denoted by the Hamiltonian matrix ( $\mathbb{H}$ ) and the overlap matrix ( $\mathbb{O}$ ) is the integral on the right handed side. Thus Eq. 2.9 can be written in the matrix form as

$$\mathbb{H}\mathbb{C} = \mathbb{E}\mathbb{O}\mathbb{C},$$

which is called the “secular equation”. The Hamiltonian matrix and the overlap matrix are the  $Q \times Q$  matrices. This eigenequation can be numerically solved by several methods (information about numerical methods for solving eigensystem can be found at chapter 11 of Ref. 50). Finally, the  $Q$  eigenvalues and the  $Q$  sets of eigenfunctions are obtained and hence they are used as primary inputs for evaluating the quantities of interest.

### 2.1.5 Periodic potential system

In real solid, it contains various defects such as vacancies, dislocations or stacking faults. Hence we encounter the difficulties to solve the Kohn-Sham equation of real solid. If we considered only a periodic solid i.e. it is invariant under translational and rotational symmetries, we can simplify this complex problem by using the Bloch theorem [51]. In Bloch theorem, the electron wave function of periodic crystal is plane waves multiplied with a periodic function  $u_{\mathbf{k}}^n(\mathbf{r})$  as

$$\Psi_{\mathbf{k}}^n(\mathbf{r}) = u_{\mathbf{k}}^n(\mathbf{r}) e^{i\mathbf{k} \cdot \mathbf{r}}, \quad (2.10)$$

where  $\mathbf{k}$  is a wave vector and  $n$  is a band index. Under Bloch theorem, the wave function and energy eigenvalue must fulfil these conditions

$$\mathcal{E}(\mathbf{k}) = \mathcal{E}(\mathbf{k} + \mathbf{G}), \quad (2.11)$$

$$\Psi_{\mathbf{k}}^n(\mathbf{r}) = \Psi_{\mathbf{k}+\mathbf{G}}^n(\mathbf{r}). \quad (2.12)$$

$\mathbf{G}$  is the reciprocal lattice vector. The maximum value of  $\mathbf{G}$  ( $\mathbf{G}_{max}$ ) is related to the cutoff energy

$$\mathcal{E}_{cut} = \frac{\hbar^2 \mathbf{G}_{max}^2}{2m}.$$

For the periodic function, we define as a summation over plane wave basis sets,

$$u_{\mathbf{k}}^n(\mathbf{r}) = \sum_j C_j^n(\mathbf{k}) e^{i\mathbf{G}_j \cdot \mathbf{r}}. \quad (2.13)$$

By substitution the defined periodic function to Eq. 2.10, the normalized electron wave function can be given by

$$\Psi_{\mathbf{k}}^n(\mathbf{r}) = \frac{1}{\sqrt{V}} \sum_j C_j^n(\mathbf{k}) e^{i(\mathbf{k} + \mathbf{G}_j) \cdot \mathbf{r}}, \quad (2.14)$$

where  $V$  is volume of primitive cell. By inserting this wave function into the Kohn-Sham equation (Eq. 2.5) and multiplying with the complex conjugate of the plane wave basis function and, finally, integrating over the whole volume of the primitive cell, we get

$$\sum_{j'} \mathcal{H}_{j,j'} C_{j'}^n(\mathbf{k}) = \mathcal{E}_n(\mathbf{k}) C_j^n(\mathbf{k}), \quad (2.15)$$

with

$$\mathcal{H}_{j,j'} = \frac{\hbar^2}{2m} |\mathbf{k} + \mathbf{G}_j|^2 \delta_{j,j'} + V_{eff}(\mathbf{G}_j - \mathbf{G}_{j'}), \quad (2.16)$$

and

$$V_{eff}(\mathbf{G}_j - \mathbf{G}_{j'}) = \int_V e^{-i\mathbf{G}_{j'} \cdot \mathbf{r}} V_{eff}(\mathbf{r}) e^{i\mathbf{G}_j \cdot \mathbf{r}} d\mathbf{r}. \quad (2.17)$$

The  $V_{eff}(\mathbf{r})$  is effective potential represented in Eq. 2.6. By diagonalization of Eq. 2.15, we can get the eigenvalues (energies) and eigenstates (Kohn-Sham orbitals) at each  $\mathbf{k}$ -point.

### 2.1.6 The PAW method

In this section, the idea of the Projector Augmented Wave (PAW) method is illustrated. The strategy of this method was adopted from the augmented plane wave method by separating the wave function into two regions: partial wave expansions inside the sphere and envelop function outside the sphere [52]. The envelope function and the partial wave expansion must be matched and differentiable at the sphere boundary. Due to numerous numbers of partial waves close to the atomic core, the all-electron wave function ( $\Psi$ ) should be mapped into a fictitious smooth function or auxiliary wave function ( $\tilde{\Psi}$ ) having a smaller number of the partial wave basis. In the followings, the tilde sign refers to the smooth function. Inside the sphere with volume  $\Omega_R$ , the wave function and smooth wave function can be expanded as a linear combination

of the partial wave basis set, i.e.

$$\begin{aligned} |\Psi(\mathbf{r})\rangle &= \sum_i a_i |\phi_i(\mathbf{r})\rangle, & \text{inside } \Omega_R \\ |\tilde{\Psi}(\mathbf{r})\rangle &= \sum_i b_i |\tilde{\phi}_i(\mathbf{r})\rangle, & \text{inside } \Omega_R \end{aligned} \quad (2.18)$$

while the all-electron partial wave and the auxiliary partial wave outside the sphere are identical,

$$\phi_i(\mathbf{r}) = \tilde{\phi}_i(\mathbf{r}). \quad \text{outside } \Omega_R \quad (2.19)$$

Index  $i$  refers to angular momentum quantum number  $(l, m)$  and atomic site  $R$ . The all-electron partial wave is the solution of the radial Schrödinger equation for an isolated atom and the auxiliary wave function can be chosen from the all-electron partial waves matching to the all electron partial wave outside the sphere. The relation between all-electron wave function and the auxiliary wave function is linked by the transformation operator  $(\tau)$ ,

$$|\Psi\rangle = \tau |\tilde{\Psi}\rangle, \quad (2.20)$$

with

$$\tau = \hat{\mathbf{1}} + \sum_R S_R.$$

From the above equation, we can see that the transformation operator modifies the all-electron wave function containing the exact profile of all properties in the form of the smooth wave function. It makes sense to define the transformation operator as the identity operator ( $\hat{\mathbf{1}}$ ) plus a sum of the atomic contribution ( $S_R$ ) at each particular site  $R$ . The atomic contribution collects the difference between all-electron partial wave and the auxiliary partial wave, i.e.  $S_R |\tilde{\phi}_i\rangle = |\phi_i\rangle - |\tilde{\phi}_i\rangle$ .

Let us define  $|\tilde{P}_i\rangle$  as the projector operator showing the local character of a wave function in the atomic region. Details of the projector operator can be found in Ref. 53. This operator must be orthonormal to the smooth partial wave basis set, namely

$$\langle \tilde{P}_m | \tilde{\phi}_n \rangle = \delta_{m,n}.$$

By using the above property, the smooth wave function can be written as

$$|\tilde{\Psi}\rangle = \sum_i |\tilde{\phi}_i\rangle \langle \tilde{P}_i | \tilde{\Psi} \rangle. \quad (2.21)$$

After applying Eq. 2.21 into Eq. 2.20, the all electron wave function can be evaluated as

$$\begin{aligned} |\Psi\rangle &= |\tilde{\Psi}\rangle + \sum_i (|\phi_i\rangle - |\tilde{\phi}_i\rangle) \langle \tilde{P}_i | \tilde{\Psi} \rangle, \\ &= \left( \hat{\mathbf{I}} + \sum_i (|\phi_i\rangle - |\tilde{\phi}_i\rangle) \langle \tilde{P}_i | \right) |\tilde{\Psi}\rangle. \end{aligned} \quad (2.22)$$

Consequently, the transformation operator is seen to be

$$\tau = \hat{\mathbf{I}} + \sum_i (|\phi_i\rangle - |\tilde{\phi}_i\rangle) \langle \tilde{P}_i|. \quad (2.23)$$

For an arbitrary observable operator represented as  $A$ , the expectation value is

$$\begin{aligned} \langle A \rangle &= \sum_n f_n \langle \Psi_n | A | \Psi_n \rangle, \\ &= \sum_n f_n \langle \tilde{\Psi}_n | \tau^\dagger A \tau | \tilde{\Psi}_n \rangle. \end{aligned} \quad (2.24)$$

The occupation number is symbolized by  $f_n$ . To apply the PAW approach to the Kohn-Sham equation, this equation can be written as

$$(\tilde{\mathcal{H}} - \mathcal{E} \tilde{S}) |\tilde{\Psi}\rangle = 0,$$

where  $\tilde{\mathcal{H}} = \tau^\dagger \mathcal{H} \tau$  and  $\tilde{S} = \tau^\dagger \tau$  are represented as pseudo Hamiltonian and overlap matrix, respectively.

### 2.1.7 Force evaluation

In DFT calculation, the force between ions is determined via the Hellman-Feynman theorem. In addition, the force evaluation method plays an important role in the Born-Oppenheimer *ab initio* molecular dynamics that will be discussed in the next section because the calculated force is used for solving the Newton equation in order to obtain accelerations, from which atomic velocities and positions are derived. These obtained parameters are used as inputs for determining other observable quantities. At this stage, details of Hellman-Feynman or force theorem are briefly discussed. At exact ground state geometry, the total force acting on each atom is, in principle, absolutely zero. To find the interatomic force in a molecule or solid, the force acting on a given nucleus with position  $\mathbf{R}_I$  can be calculated by

$$F_I = - \frac{\partial \mathcal{E}}{\partial \mathbf{R}_I}, \quad (2.25)$$

where the total energy of the system ( $\mathcal{E}$ ) can be expressed as

$$\mathcal{E} = \langle \Psi | \mathcal{H} | \Psi \rangle .$$

$\Psi$  represents as the wave function or the Kohn-Sham orbital in the DFT method and is required to be normalized i.e.  $\langle \Psi | \Psi \rangle = 1$ . By substituting the total energy functional into Eq. 2.25, we get

$$\begin{aligned} F_I &= - \langle \Psi | \frac{\partial \mathcal{H}}{\partial \mathbf{R}_I} | \Psi \rangle - \langle \frac{\partial \Psi}{\partial \mathbf{R}_I} | \mathcal{H} | \Psi \rangle - \langle \Psi | \mathcal{H} | \frac{\partial \Psi}{\partial \mathbf{R}_I} \rangle, \\ &= - \langle \Psi | \frac{\partial \mathcal{H}}{\partial \mathbf{R}_I} | \Psi \rangle - \mathcal{E} \left( \frac{\partial \langle \Psi | \Psi \rangle}{\partial \mathbf{R}_I} \right), \\ &= - \langle \Psi | \frac{\partial \mathcal{H}}{\partial \mathbf{R}_I} | \Psi \rangle . \end{aligned} \tag{2.26}$$

If the basis set depends on the atomic position such as atomic centered Gaussian function, the derivatives of the wave function with respect to atomic displacement do not vanish. As a consequence, Pulay forces arise. However, this force will be zero if the chosen basis set is independent to the nucleus position of the basis function.

### 2.1.8 *Ab initio* molecular dynamics

In condensed matter physics, molecular dynamics simulation (MD) is a very important tool to understand the dynamical properties of materials at a particular temperature. It can be used for calculating the time-dependent quantities of materials such as mean square displacement, radial distribution function etc. Molecular dynamics simulation is a method to solve time evolution of particles or nuclei in the solid or liquid (or even gaseous) phase by numerically solving an equation of motion, Newton's equation of motion in this case. In classical MD (CMD), classical forces acting on each nucleus can be determined from an empirical potential, e.g. Finnis-Sinclair [54], Lennard-Jones or 6-12 and Tersoff [55]. For large systems, the speed of the CMD simulations is very fast but the accuracy of these simulations are problematic due to inability to study the breaking and forming of chemical bonds. However, this problem can be solved by using quantum molecular dynamics (QMD). In this section, we only consider Born-Oppenheimer Molecular Dynamics (BOMD) implemented in the Vienna *Ab initio* Simulation Package (VASP). For BOMD, the electronic force acting on each nuclei is obtained from first-principles calculations such as density functional theory calculations, already mentioned in Section 2.1.7. The nucleus motions must obey the second law of Newton's equation of motion when time is evolved.

$$\begin{aligned} \mathbf{F}_i &= M_i \mathbf{a}_i, \\ -\nabla \mathcal{E}_i &= M_i \frac{d^2 \mathbf{R}_i}{dt^2}, \end{aligned} \tag{2.27}$$

where  $\mathbf{F}_i$  and  $\mathcal{E}_i$  stand for the forces acting on the  $i^{th}$  nucleus (Eq. 2.25) and energy functional obtained from the *ab initio* calculations, respectively.  $M$  is mass of nuclei and  $\mathbf{R}_i$  is the position of the  $i^{th}$  nucleus. However, the BOMD calculations are computationally expensive and limited to small systems, usually containing less than a few hundreds of atoms.

### Mean square displacement

To understand properties such as diffusion coefficient or melting temperature of solid, the mean square displacement (MSD) is a useful tool. The MSD measures how far the configuration, at a particular time, is displaced from an initial configuration. In solid, the MSD should be saturated as a function of time whereas it increases linearly with time for a liquid. The definition of the MSD can be written as

$$\text{MSD}(t) = \left\langle |\mathbf{R}(t) - \mathbf{R}(0)|^2 \right\rangle \cong \frac{1}{t_{\max}} \sum_{i=1}^N \sum_{t_0=0}^{t_{\max}} |\mathbf{R}_i(t+t_0) - \mathbf{R}_i(t_0)|^2,$$

where  $\langle \dots \rangle$  is defined as time averaging over all atoms.  $\mathbf{R}_i(t+t_0)$  and  $\mathbf{R}_i(t_0)$  are positions of atom  $i^{th}$  at a time  $t+t_0$  and  $t_0$ , respectively.  $t_{\max}$  is a maximum time-average, practically set to be half of the total simulation time.  $N$  stands for number of ions. For very long simulation time (usually referred to infinity), the diffusion coefficient ( $D$ ) can be determined by the relation

$$2\delta D = \lim_{t \rightarrow \infty} \frac{d}{dt} \langle |\mathbf{R}(t) - \mathbf{R}(0)|^2 \rangle,$$

where  $\delta$  is the dimension of the system.

### Radial distribution function

The radial distribution function (RDF or  $g(r)$ ) can be obtained from both molecular dynamics simulations and X-ray and neutron scattering experiments. It is used for probing the local configuration of the system of interest and is defined by

$$g(r) = \frac{N_i(r)}{4\pi\rho r^2 dr}.$$

$N_i(r)$  and  $\rho$  stand for total number of atoms inside spherical shell with radius larger than  $r$  and smaller than  $r+dr$  and the average density of the system, respectively. In addition, it will converge to 1 when  $r$  approaches infinity. The coordination number or number of nearest neighbors can be determined by integration of the first peak of the RDF.

### Bond angle distribution

As can be seen above, the RDF is a powerful tool for probing the local environment of the system. Another quantity used for determining the change



of the local geometry is the bond angle distribution (BAD). BAD measures the distribution of angles between the nearest neighbors of the  $i^{th}$  atom. It can be determined by counting the number of atoms at a particular angle ( $N_i(\theta)$ ) from a reference atom,

$$\text{BAD}(\theta) = \sum_{i=1}^N N_i(\theta)$$

where  $\theta$  is scanned from 0 to 180°. For applications of BAD, it has been shown to be very useful for detecting structural phase transition in various materials e.g. SiO<sub>2</sub> [56, 57], GaAs [58] and liquid phosphorus [59].

### Hydrogen density distribution

To obtain the hydrogen binding energy of hydrogen storage materials especially physisorbed systems, it is necessary to know where the hydrogen adsorption sites for materials of interest are. The location of the adsorption sites is directly related to the hydrogen density distribution. The idea of hydrogen density distribution is illustrated as follows. We assume that the hydrogen density distribution,  $\rho(\mathbf{x})$ , of the  $i^{th}$  H<sub>2</sub> center of mass which is located at position  $\mathbf{R}_i$  for a particular time can be written as [60]

$$\rho(\mathbf{x}) = \begin{cases} \sum_i e^{-\frac{1}{2} \left( \frac{|\mathbf{x}-\mathbf{R}_i|}{\sigma} \right)^2} & , \quad |\mathbf{x}-\mathbf{R}_i| \leq 3\sigma \\ 0 & , \quad |\mathbf{x}-\mathbf{R}_i| > 3\sigma \end{cases}$$

where  $\sigma$  is smearing width of a Gaussian function. Figure 2.2 defines the locations of hydrogen molecule center of mass and the corresponding densities for each H<sub>2</sub> center of mass at each given time, denoted by black balls and red curves, respectively. The hydrogen center of mass distribution is determined via the time-averaging of the hydrogen center of mass density distribution of each time step. To get accurate hydrogen density distribution, we would like to emphasize that it should be averaged within a time under thermodynamic equilibrium. The examples of hydrogen density distribution used for determining the hydrogen adsorption sites in metal organic framework-5 and covalent organic framework-1 can be found in Refs. 13 and 60.

## 2.2 Møller-Plesset perturbation theory

In condensed matter physics, several techniques are used for evaluating various observable quantities of materials, for example, DFT [38, 39], configuration interaction (CI) [37], coupled-cluster calculations [37] and so on. For the DFT method, it is proved to be a popular and successful method in both physics and quantum chemistry. However, it has several disadvantages. For example, it is unable to predict the correct bandgap of materials or describe

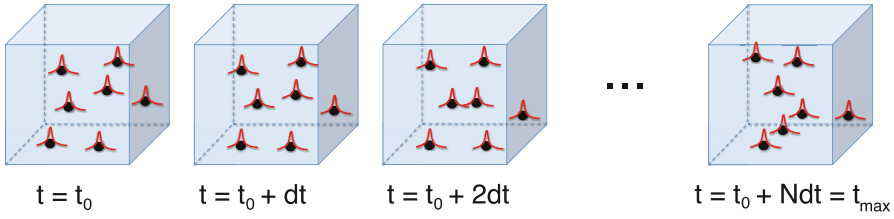


Figure 2.2: Time evolution of hydrogen center of mass density distribution calculated from the *ab initio* molecular dynamics simulations. Black spheres refer to positions of hydrogen molecule center of mass obtained from molecular dynamics simulation. The blue cubic box and red curves represent as the unitcell of the material and the probability to find the  $H_2$  molecule center of mass at a particular time, respectively. The hydrogen center of mass density distribution can be determined by time averaging of the  $H_2$  center of mass density distribution at any given time.

the weak dispersive interaction. Another successful approach used in computational materials science is "Many body perturbation theory" or MBPT [61]. In this section, details of the Rayleigh-Schrödinger perturbation theory and Møller-Plesset perturbation theory are discussed in the following.

### 2.2.1 Rayleigh-Schrödinger perturbation theory

In the MBPT, the total Hamiltonian can be considered as the reference or unperturbed Hamiltonian ( $\mathcal{H}_0$ ) disturbed by small perturbation ( $\mathcal{H}$ ),

$$\mathcal{H} = \mathcal{H}_0 + \mathcal{H} \quad (2.28)$$

is strength of the perturbation, usually set to be 1 and the unperturbed Hamiltonian must satisfy the time independent Schrödinger equation,

$$\mathcal{H}_0 \psi_0 = E^{(0)} \psi_0$$

where  $\psi_0$  and  $E^{(0)}$  are unperturbed wave function and energy, respectively. In Rayleigh-Schrödinger Perturbation Theory (RSPT), the perturbed wave function and energy are expressed as a power series of  $\mathcal{H}$ ,

$$\psi = \sum_{i=0}^{\infty} \psi^{(i)} = \psi_0 + \psi_1 + \psi_2 + \dots \quad (2.29)$$

$$E = \sum_{i=0}^{\infty} E^{(i)} = E^{(0)} + E^{(1)} + E^{(2)} + \dots \quad (2.30)$$

The  $\psi_1$ ,  $\psi_2$ , ... and  $E^{(1)}$ ,  $E^{(2)}$ , ... are first-order, second-order, ... corrections of the wave function and energy, respectively. As the perturbation level is increased from zero order to higher order, the energy and wave function should

take into account the effects behind the reference state. Due to the orthogonal requirement of the wave function, the perturbed wave functions must be orthogonal to the unperturbed wave function, namely

$$\langle \Psi_j | \Psi_0 \rangle = 0; \quad j = 1, 2, 3, \dots \quad (2.31)$$

By substituting the perturbed wave function and energy into time independent Schrödinger equation and then comparing the terms having the same power of  $\lambda$ , the zero, first, second till  $n^{th}$ -order perturbation equations are expressed as

$$\lambda^0: \quad \mathcal{H}_0 \Psi_0 = E^{(0)} \Psi_0, \quad (2.32)$$

$$\lambda^1: \quad \mathcal{H}_0 \Psi_1 + \mathcal{H}' \Psi_0 = E^{(0)} \Psi_1 + E^{(1)} \Psi_0, \quad (2.33)$$

$$\lambda^2: \quad \mathcal{H}_0 \Psi_2 + \mathcal{H}' \Psi_1 = E^{(0)} \Psi_2 + E^{(1)} \Psi_1 + E^{(2)} \Psi_0, \quad (2.34)$$

$\vdots$

$$\lambda^n: \quad \mathcal{H}_0 \Psi_n + \mathcal{H}' \Psi_{n-1} = \sum_{i=0}^n E^{(i)} \Psi_{n-i}. \quad (2.35)$$

According to Eq. 2.32, the zero-order perturbation equation is a Schrödinger equation of unperturbed system. To obtain the first-order energy ( $E^{(1)}$ ), we expand the  $\Psi_1$  as a linear combination of the solutions of unperturbed Hamiltonian ( $\Phi_i$ ),

$$\Psi_1 = \sum_i c_i \Phi_i.$$

where  $c_i$  is an arbitrary coefficient and the  $\Phi_{i \neq 0}$  must be orthonormal to the  $\Phi_0$  or  $\Psi_0$  symbolized as the solution of the unperturbed Hamiltonian. The first-order perturbation equation (Eq. 2.33) can be determined as

$$E^{(1)} = \langle \Phi_0 | \mathcal{H}' | \Phi_0 \rangle. \quad (2.36)$$

This equation implies that the first-order perturbation energy can be obtained by averaging of the  $\mathcal{H}'$  operator by using unperturbed wave function. To obtain the first-order perturbed wave function,  $\Psi_1$ , we must know the  $c_i$  coefficients. These coefficients are able to be calculated by applying  $\langle \Phi_j |$  states ( $j \neq 0$ ) to both sides of Eq. 2.33. we obtain

$$c_j = \frac{\langle \Phi_j | \mathcal{H}' | \Phi_0 \rangle}{E^{(0)} - E^{(j)}}. \quad (2.37)$$

For second-order perturbed energy and perturbed wave function, we can get

$$E^{(2)} = \sum_{i \neq 0} \frac{\langle \Phi_0 | \mathcal{H}' | \Phi_i \rangle \langle \Phi_i | \mathcal{H}' | \Phi_0 \rangle}{E^{(0)} - E^{(i)}}, \quad (2.38)$$

$$\Psi_2 = \sum_i d_i \Phi_i, \quad (2.39)$$

where

$$d_i = \sum_{j \neq 0} \frac{\langle \Phi_i | \mathcal{H}' | \Phi_j \rangle \langle \Phi_j | \mathcal{H}' | \Phi_0 \rangle}{(E^{(0)} - E^{(i)}) (E^{(0)} - E^{(j)})} - \frac{\langle \Phi_i | \mathcal{H}' | \Phi_0 \rangle \langle \Phi_0 | \mathcal{H}' | \Phi_0 \rangle}{(E^{(0)} - E^{(i)})^2}.$$

### 2.2.2 Details of Møller-Plesset perturbation theory

Møller-Plesset perturbation theory (MP) is a special case of the RSPT by replacing unperturbed Hamiltonian ( $\mathcal{H}_0$ ) and the wave function with the Fock operator and the HF wave function ( $\Phi_0$ =Slater determinant)[61], respectively. The Fock operator ( $\mathcal{F}_i$ ) is defined by

$$\begin{aligned} \mathcal{H}_0 &= \sum_{i=1}^{N_e} \mathcal{F}_i, \\ &= \sum_{i=1}^{N_e} \left( \mathbf{h}_i + \sum_{j=1}^{N_e} (\mathbf{J}_j - \mathbf{K}_j) \right). \end{aligned} \quad (2.40)$$

$\mathbf{h}_i$ ,  $\mathbf{J}_j$  and  $\mathbf{K}_j$  are one-electron, Coulomb and exchange operators, respectively. These three terms can be defined by

$$\mathbf{h}_i = -\frac{1}{2} \nabla_i^2 - \sum_{I=1}^{N_{nuc}} \frac{Z_I}{|\mathbf{R}_I - \mathbf{r}_i|}, \quad (2.41)$$

$$\mathbf{J}_i |\phi_j(2)\rangle = \langle \phi_i(1) | \frac{1}{|\mathbf{r}_1 - \mathbf{r}_2|} | \phi_i(1)\rangle |\phi_j(2)\rangle, \quad (2.42)$$

$$\mathbf{K}_i |\phi_j(2)\rangle = \langle \phi_i(1) | \frac{1}{|\mathbf{r}_1 - \mathbf{r}_2|} | \phi_j(1)\rangle |\phi_i(2)\rangle, \quad (2.43)$$

where  $\phi_j(2)$  are the eigenfunction of the  $j^{th}$  electron at position  $\mathbf{r}_2$ .  $N_e$  and  $N_{nuc}$  are denoted by numbers of electron and nuclei in the system, respectively. In the following, we define the two electron integral,  $\langle ij||kl \rangle$ , as

$$\langle ij||kl \rangle = \int d\mathbf{r}_1 d\mathbf{r}_2 \left( \frac{\phi_i^*(\mathbf{r}_1) \phi_j^*(\mathbf{r}_2) \phi_k(\mathbf{r}_1) \phi_l(\mathbf{r}_2)}{|\mathbf{r}_1 - \mathbf{r}_2|} - \frac{\phi_i^*(\mathbf{r}_1) \phi_j^*(\mathbf{r}_2) \phi_k(\mathbf{r}_2) \phi_l(\mathbf{r}_1)}{|\mathbf{r}_1 - \mathbf{r}_2|} \right).$$

For Møller-Plesset perturbation theory, the MP energy can be written as

$$\mathcal{E}_{MP} = E^{(0)} + E^{(1)} + E^{(2)} + \dots$$

Based on the RSPT, the unperturbed energy (zero order, Eq. 2.32) is

$$\begin{aligned}\mathcal{E}_{MP0} = E^{(0)} &= \langle \Phi_0 | \mathcal{H}_0 | \Phi_0 \rangle \\ &= \sum_{i=1}^{N_e} \langle \Phi_0 | \left( \mathbf{h}_i + \sum_{j=1}^{N_e} (\mathbf{J}_j - \mathbf{K}_j) \right) | \Phi_0 \rangle\end{aligned}\quad (2.44)$$

For the first order perturbation energy ( $E^{(1)}$ ), it can be directly obtained via Eq. 2.36,

$$\begin{aligned}E^{(1)} &= \langle \Phi_0 | \mathcal{H}' | \Phi_0 \rangle, \\ &= \langle \Phi_0 | \mathcal{H} - \mathcal{H}_0 | \Phi_0 \rangle,\end{aligned}\quad (2.45)$$

The MP1 energy can be written as

$$\begin{aligned}\mathcal{E}_{MP1} &= E^{(0)} + E^{(1)}, \\ &= \langle \Phi_0 | \mathcal{H}_0 | \Phi_0 \rangle + \langle \Phi_0 | \mathcal{H} - \mathcal{H}_0 | \Phi_0 \rangle, \\ &= \langle \Phi_0 | \mathcal{H} | \Phi_0 \rangle, \\ &= \sum_{i=1}^{N_e} \langle \Phi_0 | \mathbf{h}_i | \Phi_0 \rangle + \frac{1}{2} \sum_{i=1}^{N_e} \sum_{j=1}^{N_e} \langle ij || ij \rangle, \\ &= E_{\text{Hartree-Fock}}.\end{aligned}\quad (2.46)$$

For higher order MP theory, it is important to note that the electron correlation energy will be taken into account at least at the second order of the MP theory because it is well known that the correlation effects are absent in the HF theory. To determine the second-order energy correction, we start with second-order perturbation equation in the RSPT( Eq. 2.38). The matrix elements in Eq. 2.38 link between the HF wave function and all possible excited states. According to Brillouin theorem [37, 61], there is no interaction between the HF states and the state of an electron excited from occupied  $a$  state to virtual  $r$  state  $\Psi_a^r$ , namely  $\langle \Phi_0 | \mathcal{H}_0 | \Psi_a^r \rangle = 0$ . Hence the second-order perturbation energy has to deal with the double excitation states by promoting two electrons from the occupied  $a$  and  $b$  states to the virtual  $r$  and  $s$  states ( $\Psi_{ab}^{rs}$ ). The second-order perturbation energy ( $E^{(2)}$ ) can be written as

$$E^{(2)} = \sum_{a < b}^{occ} \sum_{r < s}^{vir} \frac{\langle \Phi_0 | \mathcal{H}' | \Phi_{ab}^{rs} \rangle \langle \Phi_{ab}^{rs} | \mathcal{H}' | \Phi_0 \rangle}{E^{(0)} - E_{ab}^{rs}}. \quad (2.47)$$

$E^{(0)}$  and  $E_{ab}^{rs}$  are denoted by the ground state energy and the energy of two electron excitation from the occupied  $a$  and  $b$  states to the virtual  $r$  and  $s$  states, respectively. For the MP2 energy, it can be determined by

$$\mathcal{E}_{MP2} = E^{(0)} + E^{(1)} + E^{(2)}.$$

Finally, the higher correction terms of both energies and wave functions in the MP theory can be evaluated by using the same steps mentioned above.

### 3. Hydrogen Storage in Physisorbed Systems

In this chapter, introduction to hydrogen storage problem is briefly addressed in Section 3.1. In Section 3.2, three methods for storing hydrogen, namely gaseous, liquid and solid-state storages are discussed. Results of high-surface area materials presented as promising hydrogen storage materials such as metal organic frameworks and covalent organic frameworks are extensively explained in Section 3.3.

#### 3.1 Introduction

It is a well known problem that the energy demand is increasing due to the enormous growing of industries in the world, whereas the current energy resources such as fossil fuel based resources start to be depleted. Moreover, by-products of most fossil fuels produce pollution affecting directly not only our health but also the environment leading to many severe effects e.g. global warming. Owing to these serious disadvantages, we need to find alternative energy resources which are abundant and environmentally friendly. Hydrogen economy is presumed to be a promising candidate resource for replacing the currently used energy resources because hydrogen can be split from water, very abundant in the world. In addition, non-toxic product, water, is formed from the reaction between protons and oxygen in the fuel cell. Various literatures[1–3] have shown that hydrogen possesses higher gravimetric energy density than the current energy resources such as methane and gasoline for about three times. In other words, one kilogram of hydrogen can produce the same amount of energy as 3 kg of gasoline. However, one major obstacle to use hydrogen as an alternative energy resource is that the volumetric density of hydrogen gas is indeed low,  $0.09 \text{ kg/m}^3$ . Consequently, it requires a large amount of space for storing hydrogen and hence the so-called hydrogen storage problem arises. In the next stage, three different methods to trap hydrogen will be discussed.

## 3.2 Hydrogen storage methods

As already mentioned above, one of the most challenging tasks in hydrogen economy is to investigate a suitable hydrogen storage medium. Currently, there are three important methods to store hydrogen, namely gaseous, liquid and solid-state storage. Detailed descriptions of these three methods are briefly discussed as follows.

### 3.2.1 Gaseous storage

To store hydrogen, keeping gaseous hydrogen in the storage tank is a simple and conventional method used nowadays. However, the well-known problem for this method is that hydrogen gas has very low volumetric density,  $0.09 \text{ kg/m}^3$ . Consequently, it requires tremendous space to store hydrogen inside. From an industrial point of view, a hybrid car needs 4 kg of hydrogen for driving 400 km [1]. This amount of stored hydrogen corresponds to  $45 \text{ m}^3$  of occupied volume at ambient condition. Hence, the storage tank must be extremely large and then it is unable to fit into the conventional storage tank. To improve the volumetric density, the most traditional way can be done by compressing hydrogen gas in the tank leading to gain hydrogen volumetric density. However, the main problem when  $\text{H}_2$  gas is pressurized in the tank is that the walls of the storage tank need to be well shielded for protecting the leakage of hydrogen gas. As a consequence, the tank is rather heavy in comparison to the currently used hydrocarbon tanks resulting in inefficiency for mobile applications. Finally, safety issue, cost of pressurization, hydrogen embrittlement of hydrogen tank and sudden drop of pressure during use are other drawbacks of this storage method.

### 3.2.2 Liquid storage

Based on several drawbacks of gaseous storage as previously mentioned, liquid hydrogen or slush hydrogen has received attention because it possesses higher volumetric density than the gaseous state i.e  $70.8 \text{ kg/m}^3$  for liquid hydrogen compared to  $0.09 \text{ kg/m}^3$  for  $\text{H}_2$  gas [7, 62]. Hence, the same amount of liquid hydrogen occupies smaller space than  $\text{H}_2$  gas. However, liquid hydrogen exists only in a very low and narrow range of temperature, namely 21–32 K [7]. The weak point of this storage method is thus that an enormous amount of energy is needed for cooling down  $\text{H}_2$  to reach the liquid state. In addition, the designed vessels have to be well insulated in order to prevent boil-off of  $\text{H}_2$  coming from the hydrogen evaporation (about few percent per day at room temperature [7, 8]). Disadvantages on the leakage and large amount of energy used for liquefaction make this storage method too expensive to be economic.



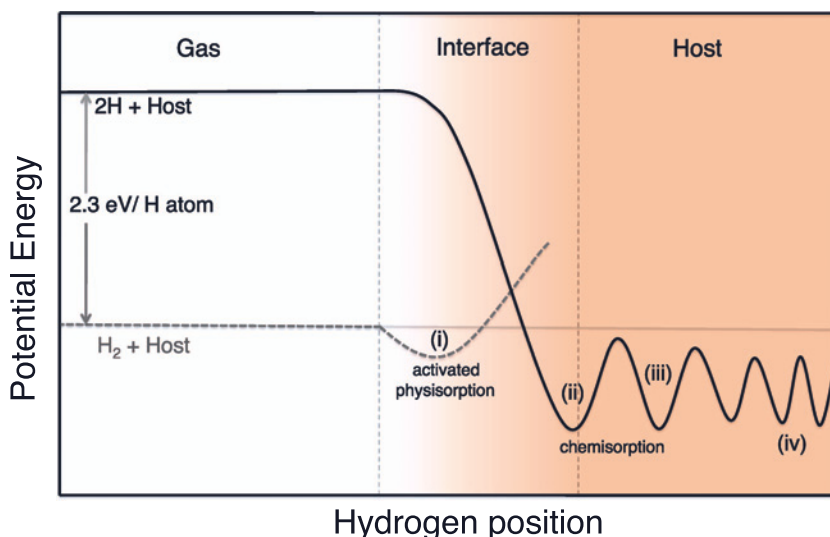


Figure 3.1: Lennard-Jones potential energies of physisorption and chemisorption mechanisms divided into four stages [7, 65]: (i)  $H_2$  physisorbed state. (ii) dissociation of  $H_2$  molecule and bonding of the dissociated hydrogen at host surface. (iii) surface penetration of the hydrogen atoms. (iv) diffusion of hydrogen atoms through the host material forming a new-hydride compound. Adapted from Ref. 65

### 3.2.3 Solid-state storage

As mentioned before, many problems are encountered when using both gaseous and liquid storage as hydrogen storage medium. Consequently, keeping hydrogen in suitable materials, so called “solid-state storage” is expected to be a promising way for hydrogen storage.

For a practical hydrogen storage material, it must satisfy the following requirements (following the requirements for the year 2015 from the U.S. Department of Energy [63, 64]).

- (i) High gravimetric density: 5.5 wt%.
- (ii) High volumetric density:  $40 \text{ kgH}_2/\text{m}^3$ .
- (iii)  $H_2$  delivery temperature:  $-40 - 85^\circ \text{C}$ .
- (iv) Operating pressure: 0.5–1.2 MPa.
- (v) Fast kinetics:  $0.02 \text{ (gH}_2\text{/s)/kW}$ .
- (vi) Low cost and safe.

Unfortunately, there is not any material satisfying all of the above requirements. Currently, mechanisms to store hydrogen in materials can be classified into two types: physisorption and chemisorption. Detailed descriptions of these two mechanisms are presented below.

## Physisorption

At ambient conditions, molecular hydrogen or  $H_2$  is a stable configuration. Once it approaches the host material surface, there is an induced dipole–induced dipole interaction or van der Waals interaction between non-dissociated hydrogen and host as shown in the stage (i) (dotted curve) of Figure 3.1. This is the physisorption mechanism. Physisorption or physical adsorption is a process in which the hydrogen molecule adheres to the host material's surface by weak dispersive interaction. Usually, this interaction strength is very weak, less than 10 kJ/mol. The big advantage of this mechanism is straightforward  $H_2$  adsorption/desorption at ambient condition leading to fast kinetic. On the downside, too weak interaction between trapped  $H_2$  molecules and host framework results in requiring cryogenic temperature/high pressure to hold molecular hydrogen within the host material. Hydrogen physisorption usually occurs in high-surface area materials such as carbon based materials [14, 62, 66–68], metal organic frameworks (MOFs) [11, 16–18, 69–72], covalent organic frameworks (COFs) [13, 73–77], zeolite [15, 78–80], zeolitic imidazolate frameworks [81–83] and so on. Many fruitful theoretical and experimental results for hydrogen storage applications in high-surface area materials are illustrated in the literature. For example, activated carbon (AC) can store hydrogen up to 0.85 wt% at 100 bar of pressure and room temperature [84]. Other carbon based materials can also act as a promising hydrogen storage medium. For single-walled carbon nanotubes, experimental results revealed that hydrogen capacities can exceed 8 wt% at 80 K and 80–100 bar of pressure [85, 86]. Further information on hydrogen storage in carbon based materials are critically reviewed in Refs. 62, 67 and 87. Metal organic frameworks (MOFs) also show promise as hydrogen storage materials because their pore sizes can be tuned due to flexible adjustment of framework components i.e. metal oxide cluster and organic linkers [88]. This is able to increase number of hydrogen adsorption sites and improve the hydrogen adsorption energy as well. Based on both theoretical and experimental studies, MOFs can maximally trap hydrogen about 3.42 wt% at 77 K and ambient pressure in Ni(HBTC)(4,4'-bipy) [89]. In addition, there is evidence that hydrogen uptake of IRMOF-20 is increased by more than 6 wt% at liquid nitrogen temperature and 77.6 bar of pressure [90]. By increasing temperature to 293 K, the amount of  $H_2$  in physisorbed systems is significantly reduced. For instance, hydrogen capacity of MOF-5 is found to be 1.65 wt% at 48 bar and ambient temperature [91]. Moreover, it has been shown that these high-surface area materials are not only used in hydrogen storage applications but also able to be used in various kinds of gas storages, e.g., Ar [92, 93],  $N_2$  [94–96],  $CH_4$  [93, 95, 97, 98],  $CO_2$  [95, 98],  $C_6H_6$  [94] and nitric oxide [99]. To obtain higher hydrogen uptake in high-surface area materials, the interaction energy of these systems must be improved to the ideal hydrogen adsorption energy, 10–60 kJ/mol (see Figure 3.2). Currently, many techniques

are proposed to increase the hydrogen adsorption energy, e.g., catenation [18, 70, 100], spillover [101, 102], decorated hydrogen attracting metals [16, 17, 103–106], open metal sites [46] and so on.

### Chemisorption

When  $H_2$  approaches to the host material's surface, weak dispersive interaction between hydrogen molecule and host framework or physisorption mechanism initially occurs as shown in stage (i) (dotted curve). Hydrogen molecules start to become dissociated if the enthalpy which is related to temperature and pressure in the system is higher than the activation energy barrier. In this phase, dissociated hydrogen atoms bond to metal atoms on the host surface by sharing their electrons (step ii). After hydrogen bonding to metals at the host's surface, hydrogen atoms penetrate to the sub-surface of the host material (step iii). Subsequently, these hydrogen atoms diffuse through the surface and populate the interstitial sites in the host material (step iv). If the hydrogen concentration is high enough, a new hydride-phase compound is formed as a stable phase. The above steps except stage (i) form the so called "chemisorption mechanism". Chemisorption is the chemical reaction between hydrogen and metal in the host framework to form a new stable hydride compound. This mechanism usually exists in light metal hydrides (e.g. LiH [107], NaH [108],  $MgH_2$  [109] and  $CaH_2$  [110]), complex hydrides such as  $LiAlH_4$  [111],  $NaAlH_4$  [20],  $KAlH_4$  [112],  $LiBH_4$  [113],  $KBH_4$  [114], Li-N-H [26],  $LaNi_5H_6$  [64],  $Mg_2FeH_6$  [115] and so on. Based on this mechanism, it is clearly seen that the hydrogen binding energy is very high, above 50 kJ/mol (see Figure 3.2) and hence high temperature and/or pressure are required to desorb hydrogen from the chemisorbed materials. More detailed descriptions of the chemisorption mechanism are found in Refs.1, 2, 7 and 65.

## 3.3 High-surface area materials

High-surface area materials have been shown to be promising materials for hydrogen storage applications due to their good capability to adsorb/desorb hydrogen at ambient condition. However, the hydrogen binding strength is still too low for practical usage. Metal organic frameworks [11, 16, 70, 104, 116] and covalent organic frameworks [73–75] have been discussed as promising hydrogen storage materials. Results for hydrogen interaction energies of materials of interest to us, namely MOF-5 and COF-1 are illustrated in Sections 3.3.1 and 3.3.2, respectively. By considering the magnitude of hydrogen binding energies when physisorbed (as it is the case in high-surface area materials), it is clearly seen that hydrogen interaction energies of the physisorbed systems including MOFs and COFs yield too weak binding in comparison to the ideal hydrogen interaction energy, namely 10–60 kJ/mol. To improve the strength of hydrogen interaction energy in physisorbed systems, decoration

of host materials via hydrogen attracting metals e.g alkali, alkaline earth and transition metals is one promising approach. In Sections 3.3.3, results obtained for Li decoration in MOF-5 are presented. Finally, size-effects of both decorated alkali metals and host frameworks on the hydrogen interaction energy are intensively studied in Section 3.3.4.

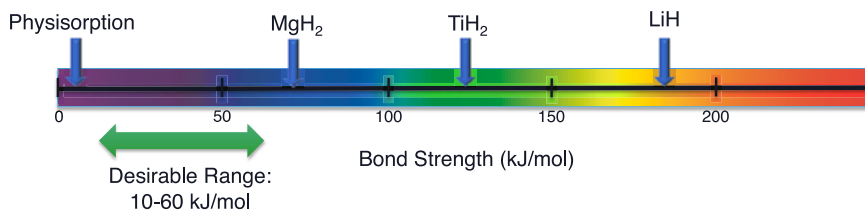
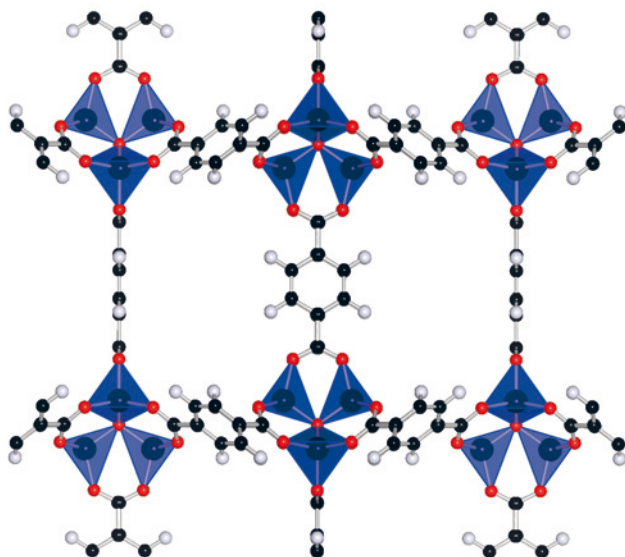


Figure 3.2: Hydrogen binding strengths for both physisorbed and chemisorbed systems. It is clearly seen that physisorbed systems give binding energies below the desirable range, whereas the hydrogen binding energies obtained from chemisorption are above the ideal range of hydrogen interaction energy. Adapted from Ref. 65.

### 3.3.1 Metal organic framework -5

Metal Organic Frameworks or MOFs were successfully synthesized by Yaghi's research group in 2002 [94, 117]. Rosi *et al.* [11] have first shown that metal organic framework-5 (MOF-5) or Zn-based MOF-5 can be used as a hydrogen storage material, reporting about 4.5 wt% of hydrogen at 77 K and ambient pressure. Subsequently, Rowsell *et al.* [71] corrected the hydrogen capacity in the MOF-5 to about 1.3 wt% at the same conditions used by Rosi *et al.* [11]. Here, the MOF-5 or Zn-based MOF-5 is focused upon due to its high surface area (2900 m<sup>2</sup> g), large pore diameter, high thermal stability, low density (0.59 g/cm<sup>3</sup>) and inexpensive production. For MOF-5, it consists of zinc(II) carboxylate metal oxide clusters and 1,4-benzenedicarboxylate (BDC) organic linker forming a cubic periodic framework with 12 Å pore size [118]. The crystal structure of MOF-5 is shown in Figure 3.3. In physisorbed systems, the most important parameter related to the hydrogen storage capacity is the adsorption energy. Therefore, the hydrogen adsorption energies at various adsorption sites in MOF-5 have been calculated as shown in paper I.

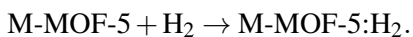
In paper I, we have investigated the hydrogen binding energies of two different MOF-5 systems, namely Zn- and Cd-based MOF-5 (in the following abbreviated as M-MOF-5 (M=Zn and Cd)), by using three different exchange-correlation functionals, namely LDA [41] and GGA with both PW91 [42] and PBE [43] functionals. Cd-MOF-5 is chosen in the current work because of its similar electronic structure with 4*d* valence state of Cd compared to the 3*d* valence state of Zn. Moreover, the common oxidation state of both Cd



*Figure 3.3:* The crystal structure of MOF-5. Color scheme: Zn atoms are located at the centers of the blue tetrahedra. Red, black and white spheres represent O, C and H, respectively.

and Zn is 2+ and their respective Pauling electronegativities are very close to each other, namely 1.65 for Zn and 1.69 for Cd. Consequently, the electronic surrounding environment of Cd-MOF-5 is very similar to that of Zn-MOF-5. The only important difference between these two is the ionic radius. In a 4-coordinated environment, Zn(II) possesses an ionic radius of 0.74 Å, while it is 0.92 Å for Cd(II). This increase in size can, however, be easily accommodated by the porous network via a simple expansion of the lattice through an “outward-movement” of the organic linkers.

To check the stability of both Zn- and Cd-MOF-5 crystal structures, we performed an unconstrained geometry optimization and our results showed that both structures are rather stable because there is no change in their crystal structures after structural relaxation. Moreover, we also found that the Cd-MOF-5 crystal structure is more open than that of Zn-MOF-5. As mentioned before, an important parameter related to the hydrogen gravimetric density is the hydrogen adsorption energy. This adsorption energy describes how strong the interaction between adsorbed hydrogen molecule and host materials is (for physisorption mechanism). Once H<sub>2</sub> adheres on the M-MOF-5 (M=Zn and Cd) surface forming M-MOF-5:H<sub>2</sub>, the chemical reaction is expressed by



The hydrogen adsorption energy ( $\Delta E_b$ ) is defined by

$$\Delta E_b = E(\text{M-MOF-5}) + E(\text{H}_2) - E(\text{M-MOF-5:H}_2),$$

where  $E(\text{M-MOF-5:H}_2)$ ,  $E(\text{M-MOF-5})$  and  $E(\text{H}_2)$  represent as the total energy of the M-MOF-5 system with adsorbed hydrogen molecule, intrinsic M-MOF-5 (M=Zn and Cd) and hydrogen gas, respectively.

To obtain hydrogen adsorption energies at all possible adsorption sites in MOF-5, we have to know where the  $\text{H}_2$  trapping sites are. Based on experimental and computational results [60, 69] of MOF-5, there are four main  $\text{H}_2$  adsorption sites, namely cup,  $\text{MO}_3$ ,  $\text{MO}_2$  (M=Zn and Cd) and hex site. The first three adsorption sites are located near the metal oxide cluster and the hex site is on the center of the hexagonal ring of the organic linker. The cup site is located at the center of the three  $\text{MO}_4$  triangular faces (see Figures 3.4A and 3.4B or Figure 3.13A). When  $\text{H}_2$  is trapped on top of  $\text{MO}_3$  (Figure 3.4C) and  $\text{MO}_2$  (Figure 3.4D) faces at the metal oxide cluster, they are denoted by  $\text{MO}_3$  and  $\text{MO}_2$  sites, respectively. In the current work, we calculated the hydrogen adsorption energies at the adsorption sites near metal oxide cluster by considering two different orientations of  $\text{H}_2$  molecule, namely parallel and perpendicular orientations for each adsorption site. The locations of all considered adsorption sites are graphically displayed in Figure 3.4 and the hydrogen adsorption energies corresponding to these adsorption sites are reported in Table 3.1.

From Table 3.1, it is clearly seen that the hydrogen binding energies are dependent on the used exchange-correlation functional. Since we are dealing with the problem of weak dispersive interaction, the  $\text{H}_2$  adsorption energies should be less than 100 meV. Consequently, we are encountering over-binding for LDA functional and under-binding for both GGA-PW91 and GGA-PBE functionals. This is a well known problem when using DFT to handle the van der Waals interactions. In principle, we should use high accuracy methods such as coupled-cluster or Møller-Plesset perturbation theory to address the weak dispersive issue. These methods work very well for small system (usually less than 50 atoms). In practice, it is almost impossible to perform such high-accuracy calculations due to the rather large cell size of MOF-5 resulting in extremely expensive computational costs for these methods. Due to this restriction, DFT is chosen as a suitable tool to study the hydrogen physisorption mechanism in MOF-5. Regarding the discrepancy in magnitude of the hydrogen physisorption energies calculated from DFT calculations, only the *trend* of the  $\text{H}_2$  adsorption energies is considered in the current work. Based on inelastic neutron experiment [69], the trend of binding strength of Zn-MOF-5 was found as follows:  $\Delta E_b(\text{cup}) > \Delta E_b(\text{ZnO}_3) > \Delta E_b(\text{ZnO}_2)$ . To compare the trend of  $\text{H}_2$  binding energies reported in Table 3.1 compared to the available experimental data [69], our results reveal that LDA reproduces the experimental trends while the trends of hydrogen physisorption energies

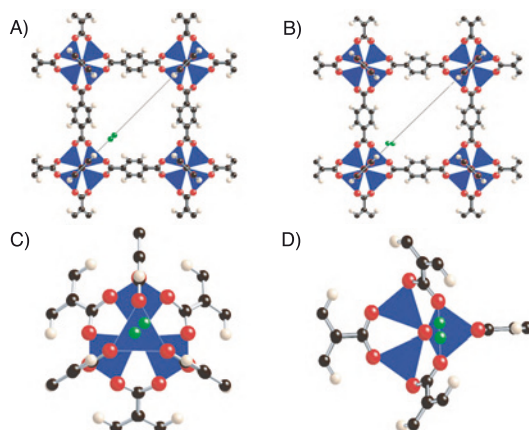


*Figure 3.4:* The  $\text{H}_2$  adsorption sites in M-MOF-5 ( $\text{M} = \text{Zn}, \text{Cd}$ ). Cup site: A) adsorbed  $\text{H}_2$  axis is parallel to the three-fold rotational axis (diagonal line). B) bond of adsorbed hydrogen is perpendicular to the three-fold rotation axis. C)  $\text{MO}_3$  site with  $\text{H}_2$  molecule perpendicular to the three-fold rotation axis. D)  $\text{MO}_2$  site with perpendicular orientation of  $\text{H}_2$  molecule to the two-fold rotation axis. We do not show for other two cases, namely parallel orientation of  $\text{H}_2$  molecule at  $\text{MO}_2$  and  $\text{MO}_3$  sites in which  $\text{H}_2$  bond is parallel to three-fold and two-fold rotation axis, respectively. Zn or Cd are at the centers of blue tetrahedra and O, C, H and adsorbed  $\text{H}_2$  are symbolized as red, black, white, and green spheres, respectively.

calculated from both GGA functionals show a different trend. Owing to this reason, LDA functional emerges as the most suitable functional among those considered here for studying the interaction between a hydrogen molecule and Zn-MOF-5.

By applying the LDA functional to the Cd-MOF-5 system, it is clearly seen that the hydrogen binding energies at the cup site ( with both parallel and perpendicular alignments of  $\text{H}_2$  molecule ) are almost equal for both Zn-MOF-5 and Cd-MOF-5. However, these binding energies are dramatically increased from 110 meV ( $\text{ZnO}_3 \perp$ ) to 149.7 meV ( $\text{CdO}_3 \perp$ ) at  $\text{MO}_3$  sites corresponding to a 25 % improvement of hydrogen binding energies when we changes the host framework from Zn-MOF-5 to Cd-MOF-5. Likewise as for the  $\text{MO}_3$  adsorption site, hydrogen adsorption energy of Cd-MOF-5 at  $\text{MO}_2$  sites is gaining for 24 % compared to Zn-MOF-5. The increment in the binding energies at both  $\text{MO}_3$  and  $\text{MO}_2$  sites can be understood as follows. Due to the more open in crystal structure of Cd-MOF-5 in comparison to Zn-MOF-5,  $\text{H}_2$  can be trapped closer and interacts more strongly with the metal oxide cluster in Cd-MOF-5. In addition, the larger ionic radius of Cd leads to higher polarizability of its electron cloud and results in stronger binding energy because van der Waals interaction is proportional to polarizability. Owing to the significant increase of binding energies and more-open crystal structure, we

EXC-func	H <sub>2</sub> site	$\Delta E_b$ (meV)		
		Zn-MOF-5	Cd-MOF-5	Zn-MOF-5
LDA	cup	125.6	133.3	133 <sup>a</sup>
	cup $\perp$	157.7	160.4	160 <sup>a</sup>
	MO <sub>2</sub>	84.8	97.4	56 <sup>a</sup>
	MO <sub>2</sub> $\perp$	86.5	125.2	108 <sup>a</sup>
	MO <sub>3</sub>	90.2	80.8	86 <sup>a</sup>
	MO <sub>3</sub> $\perp$	110.2	149.7	115 <sup>a</sup>
GGA (PW91)	cup	18.9	22.3	—
	cup $\perp$	32.8	37.0	—
	MO <sub>2</sub>	32.7	29.2	—
	MO <sub>2</sub> $\perp$	23.2	26.4	—
	MO <sub>3</sub>	42.3	42.8	—
	MO <sub>3</sub> $\perp$	21.0	31.8	—
GGA (PBE)	cup	8.4	7.2	9.5 <sup>b</sup>
	cup $\perp$	17.3	21.3	17.9 <sup>b</sup>
	MO <sub>2</sub>	15.8	15.0	20.8 <sup>b</sup>
	MO <sub>2</sub> $\perp$	8.3	9.6	7.5 <sup>b</sup>
	MO <sub>3</sub>	22.4	16.4	20.2 <sup>b</sup>
	MO <sub>3</sub> $\perp$	13.6	17.9	12.5 <sup>b</sup>

<sup>a</sup> LDA results from Ref. 69

<sup>b</sup> GGA-PBE results from Ref. 60

Table 3.1: *Binding energies of H<sub>2</sub> in Zn-MOF-5 and Cd-MOF-5 of all adsorption sites near metal oxide cluster with perpendicular ( $\perp$ ) and parallel (||) orientations for three different exchange-correlation functionals, compared to available results in the literatures.*

expect that Cd-MOF-5 can bind larger amounts of hydrogen in comparison to Zn-MOF-5. This might compensate for the lower gravimetric density due to containing the heavier element Cd.

In summary, the hydrogen binding energies in MOF-5 can be improved by opening the metal oxide cluster, resulting in higher polarizability and closer equilibrium distance between H<sub>2</sub> and the host framework, leading to stronger bonds with the host framework. However, this significant increase in binding energies can still not reach the ideal range of hydrogen binding energy displayed in Figure 3.2.

### 3.3.2 Covalent organic framework -1

To enhance the hydrogen gravimetric density, the host materials should trap as much hydrogen as possible. This property is directly related to hydrogen binding strength and number of hydrogen adsorption sites in the host framework. A major benefit of high-surface area materials is that they possess numerous hydrogen adsorption sites, although the H<sub>2</sub> interaction strength in these ma-



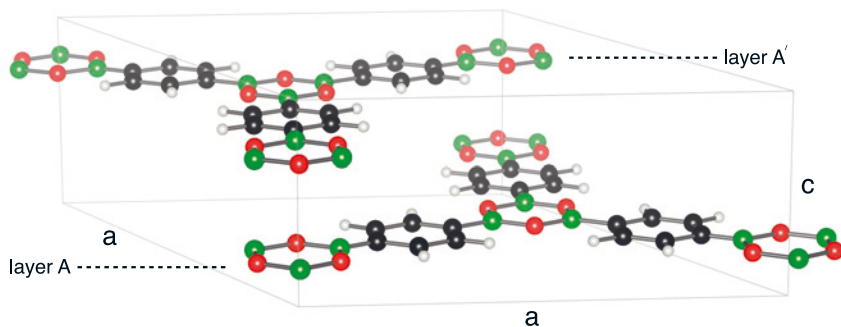


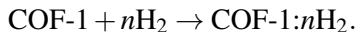
Figure 3.5: The COF-1 crystal structure [12]. It consists of boroxine ( $B_3O_3$ ) rings bonding to three benzene rings forming a periodic framework. COF-1 has two layers, namely a lower layer (layer A) and an upper layer (layer A') with 3.35 Å interlayer distance. Its crystal structure possesses the hexagonal space group  $P6_3/mmc$  with lattice parameters:  $a = 15.65$  Å and  $c = 6.70$  Å. The atoms are symbolized as follows: B, O, C and H atoms are drawn in green, red, black and grey, respectively.

materials is still too weak. Another way for improving the hydrogen gravimetric density is by having host frameworks should be as light as possible. Due to these reasons, high-surface area materials formed from light elements such as Covalent Organic Frameworks or COFs are believed to be good candidates for hydrogen storage materials. In paper II, COF-1 was selected because of its light weight due to being formed from light elements i.e. hydrogen, boron, carbon and oxygen, high thermal stability (up to 600 °C), low density, large pore size (15 Å) and small unit cell size. Experimental results [101] revealed that COF-1 can store up to 1.27 wt% of hydrogen at 77K and ambient pressure and the hydrogen capacity is reduced to 0.26 wt% at 100 bar of pressure and room temperature. The crystal structure of COF-1 is shown in Figure 3.5.

In this section, we present results from our theoretical investigations on the hydrogen binding strengths for various hydrogen loadings in COF-1 by using density functional theory (DFT) and second-order Møller-Plesset perturbation theory (MP2). In our DFT calculations, the LDA exchange-correlation functional was chosen because the COF-1 structural parameters obtained from this functional are found to be in better agreement with experimental results than those obtained from calculations using the PBE functional. In addition, paper I has shown that LDA is found to be the most suitable exchange-correlation functional among those considered since it reproduces the correct experimental trend of hydrogen physisorption energies in MOF-5. However, it is a well known problem that the DFT-LDA method fails to get the correct magnitude of hydrogen interaction energy due to over-binding issues. In view of this deficiency of DFT-LDA, only the *trend* of hydrogen adsorption energies is considered in the current work. A much more reliable method for treating weak dispersive interaction is the second-order Møller-Plesset perturbation theory

or MP2 (basic descriptions of the MP2 method are explained in Chapter 2). This is the reason why the MP2 method is chosen as reference in this work. However, the required large computational resource is the major drawback of the MP2 technique and hence it is not suitable for large systems such as MOFs and COFs. A traditional way for reducing the computational expense to an acceptable level is to consider only a small cluster of the system of interest. In this work, we have chosen this approach to calculate the MP2 binding energies at various adsorption sites of COF-1. Moreover, these reported binding energies have been corrected for the basis set superposition error (BSSE) correction with the counterpoise method [119, 120].

When hydrogen molecules adsorb on the COF-1 surface, the adsorption process between  $n\text{H}_2$  molecules and COF-1 is expressed as



The hydrogen binding energy can be simply evaluated via

$$\Delta E_b = E(\text{COF-1}) + nE(\text{H}_2) - E(\text{COF-1:nH}_2),$$

where  $E(\text{COF-1:nH}_2)$ ,  $E(\text{COF-1})$  and  $E(\text{H}_2)$  represent the total energy of the COF-1 framework with  $n\text{H}_2$  adsorbed inside, intrinsic COF-1 and free  $\text{H}_2$  molecule, respectively. Next, the adsorption sites of the COF-1 are investigated. Due to the similarity in crystal geometry between graphene and COF-1, model adsorption sites of graphene are applied for COF-1. The adsorption sites and the hydrogen binding energies corresponding to these adsorption sites of COF-1 are presented in Figures 3.6 and 3.7, respectively. We would like to note that hydrogen adsorption energies reported here are the  $\text{H}_2$  binding energies with hydrogen molecule axis perpendicular to the COF-1 layer. This is because the head-on configuration is more favorable than the parallel orientation of  $\text{H}_2$  molecule in which the  $\text{H}_2$  molecular axis is oriented parallel to the COF-1 layer.

According to the  $\text{H}_2$  adsorption energies reported in Figure 3.7, DFT binding energies at  $\text{B}_3\text{O}_3$  ring show exactly the same trend as the MP2 binding energies, namely oxygen site > B–O bridge site > hollow site > boron site. For  $\text{C}_6\text{H}_4$  ring, results of binding energy trend from MP2 calculation are slightly different from the DFT calculations. This disagreement is due to the proximity between hydrogen molecule adsorbed at the hollow site and hydrogen atom at the upper layer (layer A' in Figure 3.5) in our DFT calculations resulting in strong repulsive interaction between these two and, therefore, DFT binding energy at site 7 ( see Figure 3.7) drops. In our MP2 calculations, this repulsive interaction between  $\text{H}_2$  and layer A' is absent leading to different trends of  $\text{H}_2$  adsorption energies between DFT and MP2 methods for the sites on the benzene ring.

As shown in Figure 3.7, a hydrogen molecule prefers to be trapped at the adsorption sites on benzene ring due to higher binding energies than the sites

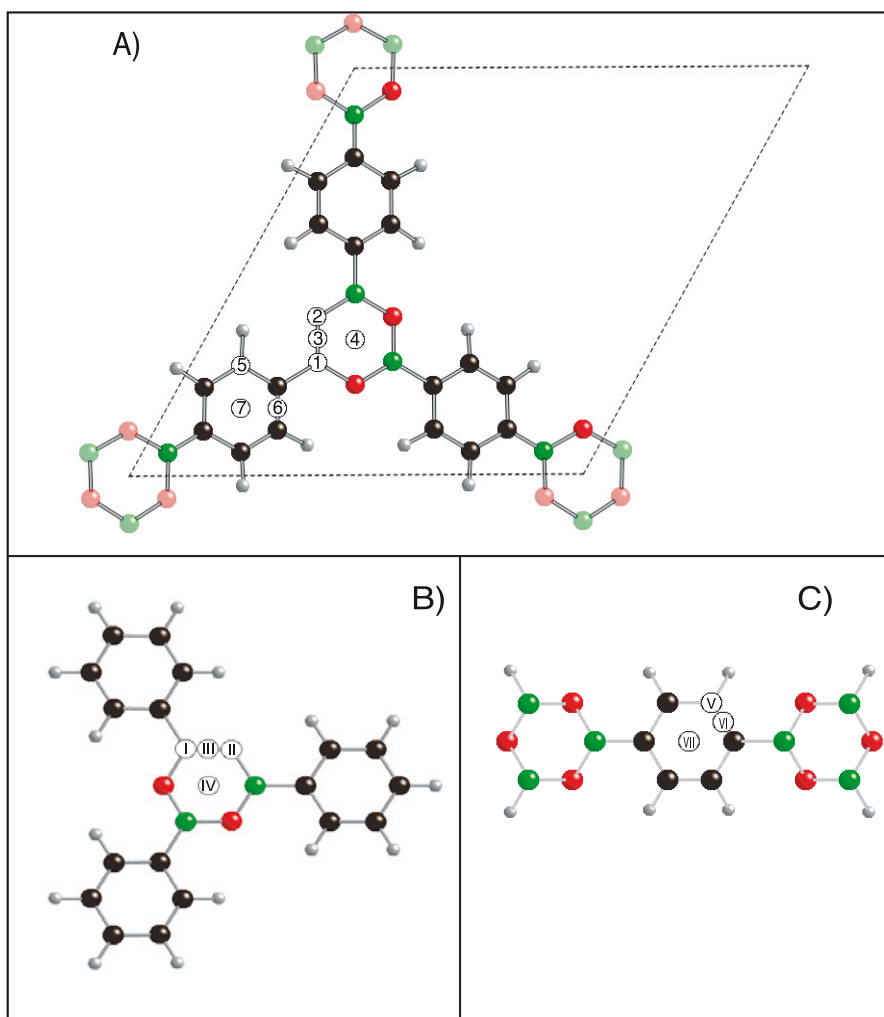


*Figure 3.6:* A) Hydrogen adsorption sites of COF-1 in the periodic framework (DFT calculations). Numbers 1–4 are denoted as the adsorption sites on B<sub>3</sub>O<sub>3</sub> ring : 1 boron site, 2 oxygen site, 3 B–O bridge site and 4 hollow site. 5–7 correspond to: 5 carbon site, 6 C–C bridged site and 7 hollow sites of benzene ring, respectively. B) and C) Hydrogen trapping sites for MP2 calculations (cluster model). In B<sub>3</sub>O<sub>3</sub> cluster, I–IV are the boron site, oxygen site, B–O bridge, and hollow sites, respectively. V–VII indicate carbon site, C–C bridge, and hollow sites of benzene cluster.

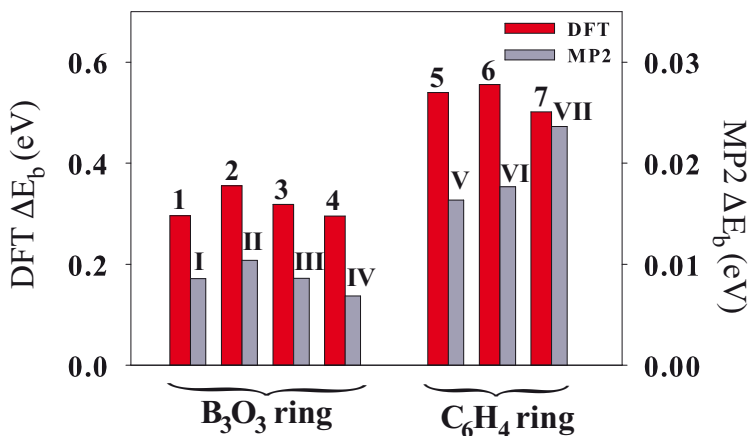


Figure 3.7: The hydrogen adsorption energies for a hydrogen molecule trapped in the COF-1 at all considered adsorption sites on both B<sub>3</sub>O<sub>3</sub> and C<sub>6</sub>H<sub>4</sub> rings (a detailed description of the adsorption sites is given in Figure 3.6). The dark red and light blue bars are the hydrogen adsorption energies calculated by DFT and MP2 methods, respectively.

on boroxine ring. To clarify this finding, we performed *ab initio* MD simulations by initially placing a H<sub>2</sub> molecule at an oxygen site which possesses the highest binding energy site in the B<sub>3</sub>O<sub>3</sub> ring. We found that hydrogen shifts to the benzene ring, which is the higher binding energy place, when time is evolved. Moreover, we also tested the case of introducing a hydrogen molecule on the C–C bridge site of benzene ring which possesses the highest binding energy site. Our molecular dynamics results show that H<sub>2</sub> remains trapped on the benzene ring. These results confirm that a H<sub>2</sub> molecule prefers to be trapped at the site on benzene ring rather than on boroxine ring at low hydrogen loading due to higher binding energies of the sites on the benzene ring.

As can be seen in Figure 3.5, hydrogen molecules are trapped at the pore of COF-1 and hence it can be distributed more than one H<sub>2</sub> molecule adsorbed at the particular adsorption site in the COF-1 host. In the current work, 3H<sub>2</sub>, 12H<sub>2</sub> and 24H<sub>2</sub> of hydrogen loadings are chosen, and the averaged hydrogen adsorption energies of all considered hydrogen loadings are determined as shown in Figure 3.8. For 3H<sub>2</sub> loading, the binding energy is the averaged value of those when the molecules are distributed either over the three oxygen sites of the B<sub>3</sub>O<sub>3</sub> ring or over three alternating carbon sites of the benzene ring. This averaging process will be used for comparison with the subsequent case of adsorbed 12H<sub>2</sub> and 24H<sub>2</sub> molecules in the system in which hydrogen molecules are simultaneously distributed over the sites on both B<sub>3</sub>O<sub>3</sub> and C<sub>6</sub>H<sub>4</sub> rings. In case of 12H<sub>2</sub> loading, layer A is fully decorated by three hydrogen molecules on B<sub>3</sub>O<sub>3</sub> ring and three H<sub>2</sub> molecules are trapped on each of

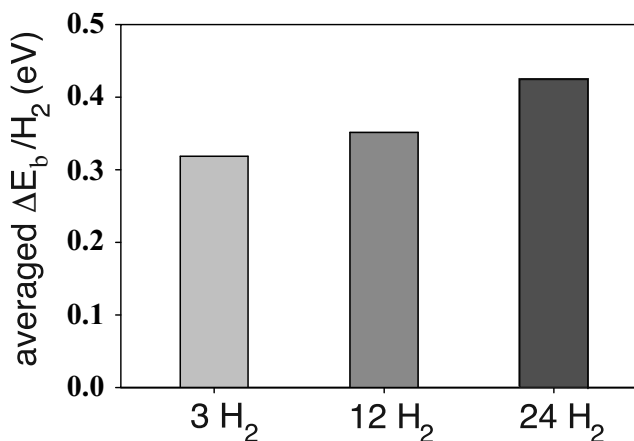


Figure 3.8: The averaged hydrogen adsorption energies per  $\text{H}_2$  with  $n\text{H}_2$  loadings ( $n = 3, 12$ , and  $24$ ) in the COF-1 host.

the three benzene rings. For  $24\text{H}_2$  loading,  $12\text{H}_2$  are introduced on both layer A and A' simultaneously. The locations of adsorption sites can be clearly visualized by the hydrogen center of mass distribution plot seen in Figure 3.9 (a detailed description of this plot is given in Chapter 2).

As seen from Figure 3.8, the averaged binding energies increase when the hydrogen loadings rise. This increment in hydrogen physisorption energies from  $3\text{H}_2$  to  $12\text{H}_2$  loadings is related to the attractive  $\text{H}_2\text{-H}_2$  interaction. When increasing the numbers of hydrogen loading from  $12\text{H}_2$  to  $24\text{H}_2$ , the averaged binding energies are found again to increase. We believed that this gaining of hydrogen adsorption energies might be related to the interaction from the induced charge of COF-1 host due to the adsorbed  $\text{H}_2$  molecules. Consequently, increasing of electrostatic interaction between adsorbed  $\text{H}_2$  and atoms on both layers is observed and this leads to the observed rise in hydrogen adsorption energy for  $24\text{H}_2$  loading.

To study dynamic behavior of hydrogen molecule under different hydrogen loadings, we performed *ab initio* molecular dynamics at 77 K for  $3\text{H}_2$ ,  $12\text{H}_2$  and  $24\text{H}_2$  cases. As previously mentioned for single hydrogen molecule adsorption, a hydrogen molecule is likely to trap at the sites on benzene ring due to it possessing higher binding energy than the other sites. However, by increasing the number of hydrogen loadings from  $1\text{H}_2$  to  $3\text{H}_2$  in which all  $3\text{H}_2$  are adsorbed at the oxygen sites, our MD simulations revealed that all three hydrogen molecules are able to be trapped at their initial adsorption sites. This situation also occurs in cases of both  $12\text{H}_2$  and  $24\text{H}_2$  distributed in COF-1 when MD simulations are performed. This is because the unavailability of binding sites for adsorbing  $\text{H}_2$  molecules leads to a decrease in  $\text{H}_2$  mobility resulting in trapping of hydrogen molecules at their initial adsorption sites.

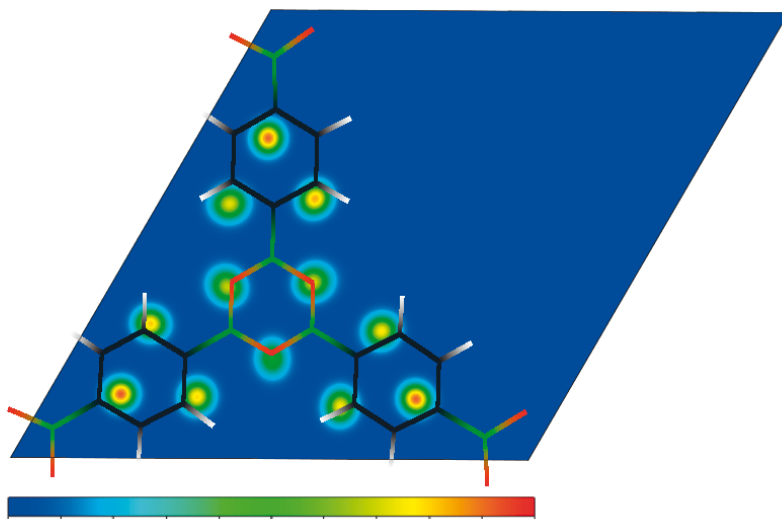


Figure 3.9: The time-averaged hydrogen center of mass density distribution in the (001) plane at  $T=77$  K. The colors specify the magnitude of the  $H_2$  distribution and change on a linear scale from blue (corresponding to zero hydrogen density) to red (corresponding to the highest recorded hydrogen density). The atom colors specifying the elements of the COF-1 framework are identical to those used in Figure 3.5.

In conclusion, adsorptions of hydrogen molecules in the COF-1 have been theoretically investigated by first-principles calculations. Our results show that the DFT-LDA method gives the same trend to the MP2 method. By increasing the hydrogen loading from  $3H_2$  to  $24H_2$ , the binding energies are found to rise due to the effects from the  $H_2$ - $H_2$  interaction and the induced charge on the COF-1 framework. Finally, *ab initio* MD revealed that the hydrogen molecules are able to be trapped at their initial adsorption sites for high hydrogen loadings because of the blockage of other hydrogen molecules trapped at adjacent adsorption sites leading to a reduction in hydrogen mobility.

### 3.3.3 Li decorations in metal organic framework -5

As shown in the previous sections, the hydrogen binding energies in MOF-5 and COF-1 do not satisfy the hydrogen storage requirements. Hence, we should investigate new strategies for improving the hydrogen adsorption energy. In paper III, we proposed the method for improving the hydrogen adsorption energy by introducing Li atoms on the BDC linker of MOF-5 in order to create isolated Li charged state for interacting with hydrogen molecules. Consequently, the enhancement in hydrogen adsorption energy due to the electrostatic interaction between charged Li and  $H_2$  occurs. When Li atoms are introduced in MOF-5, two possible configurations might be formed: (i) decorated

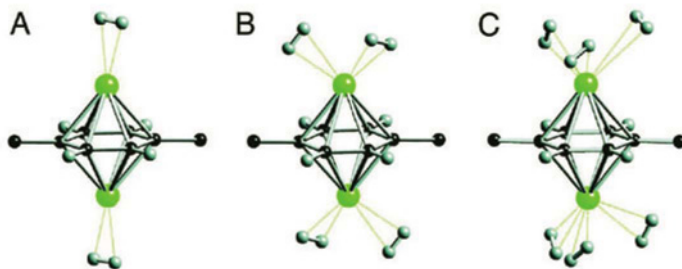


Figure 3.10: Optimized geometries of Li decorated MOF-5. A–C) 1H<sub>2</sub>, 2H<sub>2</sub> and 3H<sub>2</sub> adsorbed per Li atom, respectively. Black, green and white balls represent carbon, lithium and hydrogen, respectively.

Li atoms formed as a Li cluster at center of MOF-5 pore, or (ii) decorated Li atoms adsorbed on the BDC linker of the MOF-5. To clarify the stability of these possible configurations, total energy calculations were performed and our results reveal that the latter gives lower total energy than the former by 0.25 eV/Li. Hence, Li atoms are likely to be adsorbed on the BDC linker rather than forming a Li cluster at center of MOF-5 pore. According to the electronic structure of the BDC linker, it can maximally hold two Li atoms per BDC unit. The optimized geometries of Li decorations on BDC linker with various hydrogen loadings, namely 1–3H<sub>2</sub> per Li atom are displayed in Figure 3.10.

To investigate the interaction strength between Li and H<sub>2</sub> molecules, the hydrogen binding energy can be evaluated as

$$E_b = E(\text{Li:MOF-5}) + nE(\text{H}_2) - E(\text{Li:MOF-5:nH}_2)$$

where  $E(\text{Li:MOF-5})$ ,  $E(\text{Li:MOF-5:nH}_2)$  and  $E(\text{H}_2)$  denote the total energy of Li decorated MOF-5,  $n\text{H}_2$  molecules trapped on Li-functionalized MOF-5 and free hydrogen molecule, respectively. We found that one Li atom can maximally adsorb three hydrogen molecules with hydrogen binding energies of 18 kJ/(molH<sub>2</sub>) for  $n=1$ , 16 kJ/(molH<sub>2</sub>) for  $n=2$  and 12 kJ/(molH<sub>2</sub>) for  $n=3$ , respectively. In addition, these hydrogen adsorption energies reported by us are about 2–3 times higher than that of H<sub>2</sub> molecule directly adsorbed on the MOF-5 surface which is about 5 kJ/(molH<sub>2</sub>) [118]. To investigate the nature of the enhancement of these hydrogen adsorption energies, self-consistent Bader charge analysis [121] was carried out and shows that Li loses about 0.9e. Based on this evidence, the improvement in hydrogen physisorption energies in Li decorated MOF-5 comes from the charge-quadrupole and charge-dipole interactions between Li and H<sub>2</sub> molecules.

To check that Li and H<sub>2</sub> are able to remain trapped at their initial adsorption sites when the temperature is increased, the pair distribution functions (PDF) of the C<sub>6</sub><sup>com</sup>–Li, Li–H<sub>2</sub><sup>com</sup> and Zn–H<sub>2</sub><sup>com</sup> (see abbreviations in Figure 3.11) pairs

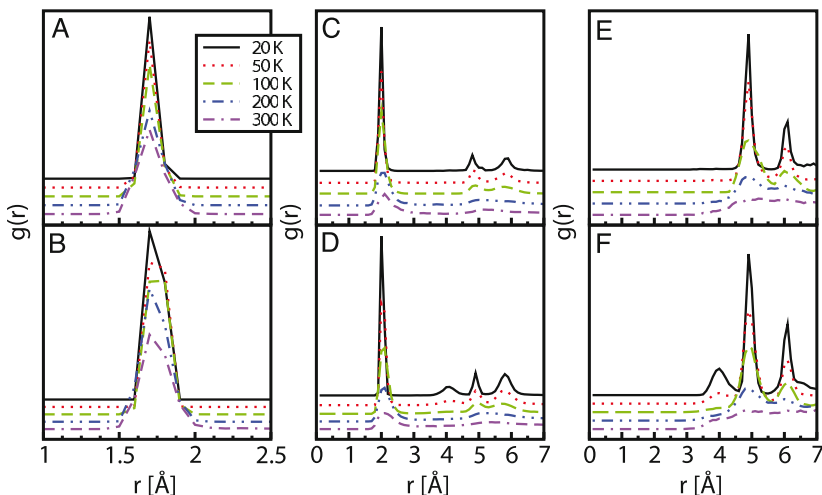


Figure 3.11: Temperature dependent pair distribution functions (PDF) of Li trapped on the BDC linker of MOF-5. For  $5\text{H}_2$  per formula unit, A) PDF of  $\text{C}_6^{\text{com}}\text{-Li}$ . C) PDF of  $\text{Li-H}_2^{\text{com}}$ . E) PDF of  $\text{Zn-H}_2^{\text{com}}$ . For  $18\text{H}_2$  per formula unit, B) PDF of  $\text{C}_6^{\text{com}}\text{-Li}$ . D) PDF of  $\text{Li-H}_2^{\text{com}}$ . F) PDF of  $\text{Zn-H}_2^{\text{com}}$ . The  $\text{C}_6^{\text{com}}$  and  $\text{H}_2^{\text{com}}$  are symbolized as the center of mass of hexagonal ring and hydrogen molecule, respectively.

with two different hydrogen concentrations, namely  $5\text{H}_2$  and  $18\text{H}_2$  loadings per formula unit have been calculated from *ab initio* molecular dynamics simulations. As seen in Figures 3.11A and 3.11B, Li atoms are shown to be able to strong attach to the MOF-5 host (about  $1.7 \text{ \AA}$ ) upto  $300 \text{ K}$  for both considered hydrogen loadings. At room temperature, Figures 3.11C and 3.11D show that hydrogen molecules are still able to remain trapped on Li atoms. By considering the PDF of  $\text{Zn-H}_2^{\text{com}}$ , the first peak is found at  $r = 4.7 \text{ \AA}$  for  $5\text{H}_2$  loading (Figure 3.11E) corresponding to the distance between Zn and  $\text{H}_2^{\text{com}}$ . After increasing hydrogen capacity from  $5\text{H}_2$  to  $18 \text{H}_2$ , there is an extra peak at  $3.8 \text{ \AA}$  (Figure 3.11F). This is due to other  $\text{H}_2$  molecules trapped at another population site of the MOF-5. Finally, the hydrogen capacity can be calculated by integrating the first peak of PDF as seen in Figure 3.11D and we found that hydrogen capacities for the case of  $18\text{H}_2$  loading at  $200 \text{ K}$  and  $300 \text{ K}$  correspond to  $2.9$  and  $2.0 \text{ wt\%}$ , respectively. At ambient condition, the amount of hydrogen uptake found by us is the highest hydrogen storage capacity reported in the MOF-5.

Our conclusion is that Li decorations on the BDC linker of MOF-5 is a promising route towards improved hydrogen adsorption strength. The results obtained by us show that Li atoms carry a charge of about  $+0.9e$  per Li atom and they strongly bind hydrogen molecules with hydrogen adsorption energies of  $18$ ,  $16$  and  $12 \text{ kJ/(molH}_2\text{)}$  for  $n=1$ ,  $2$  and  $3\text{H}_2$  trapped on Li, respectively.



Finally, hydrogen capacities of this system calculated from *Ab initio* molecular dynamics simulations with 18H<sub>2</sub> loading are 2.9 wt % and 2.0 wt% at 200 and 300 K, respectively.

### 3.3.4 Alkali functionalization in metal organic framework-16

As shown in the previous section, functionalizing high-surface area materials with Li can improve the hydrogen binding energy. Not only Li but also other metals such as Ca [106, 122, 123], Ti [105] and Mg [124] are shown to be able to improve the hydrogen adsorption energy. Moreover, effects from the size of the host framework might play an important role in enhancing the hydrogen binding energy. These aspects motivate us to investigate in more detail the effects from both decorated metals and host framework size on the hydrogen binding energy as presented in paper IV.

In paper IV, we theoretically studied the hydrogen adsorption energies when three types of alkali metals (Li, Na and K) are functionalized into three different iso-reticular metal organic framework-16 systems (MOF-16), namely Zn-MOF-16, Mg-MOF-16 and Ca-MOF-16 and then investigated which combination gives the highest hydrogen binding energy from these configurations.

Iso-reticular metal organic framework-16 or Zn-MOF-16 consists of metal oxide clusters, exactly identical to the metal oxide cluster in MOF-5, but the organic linker is slightly different, namely triphenyldicarboxylate (TPDC) struts for MOF-16 as opposed to 1,4 benzenedicarboxylate (BDC) for MOF-5. MOF-16 is chosen in the current work due to having the largest BET surface area in the metal organic framework series [70, 94, 125] leading to many adsorption sites in the MOF-16 unit cell i.e. a total of 38 adsorption sites (20 sites near the metal oxide cluster and 18 sites on the TPDC linkers) and fast adsorption/desorption both decorated metals and hydrogen molecules. The BET surface area is the surface area of a material calculated from the Brunauer, Emmett, and Teller theory [126]. However, the volumetric density is still too low for this material in comparison to, e.g., MOF-5. This is the deficient of the MOF-16 compared to the MOF-5. The MOF-16 crystal structure is displayed in Figure 3.12.

To investigate the adsorption sites in MOF-16, the model adsorption sites of MOF-5 are used. Due to the close similarity in crystal geometry between MOF-5 and MOF-16, the adsorption sites near the metal oxide cluster of MOF-16 are exactly identical to the adsorption sites near the metal oxide cluster of MOF-5, namely cup, MO<sub>3</sub> and MO<sub>2</sub>. At the organic linker, we defined the adsorption site at the center of the benzene ring adjacent to the metal oxide cluster as hex1 site. The hex2 site is defined as an adsorption site on the center of the middle benzene ring of the TPDC linkers. These adsorption sites of M-MOF-16 (M=Zn, Mg and Ca) are displayed in Figure 3.13. In the present work, we first introduce the alkali metal at particular adsorption site and then subsequently place H<sub>2</sub> molecules (ranging from 1H<sub>2</sub> to 4H<sub>2</sub>) on the alkali

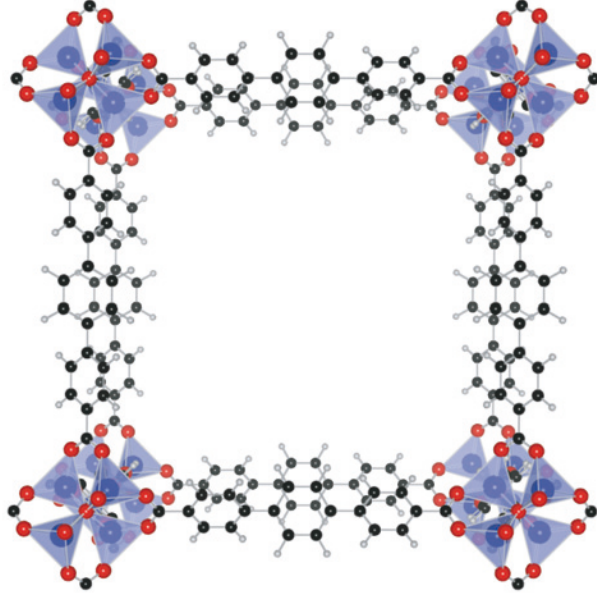


Figure 3.12: Crystal structure of MOF-16. The metal atoms M (M = Zn, Mg and Ca) are located at the center of the blue transparent polyhedra. Oxygen, carbon, and hydrogen atoms are shown as red, black, and white spheres, respectively.

metal. Consequently, we have to consider both the alkali metal binding energy ( $\Delta E_{am}$ ) and hydrogen adsorption energies ( $\Delta E_b$ ), and these energies can be calculated as

$$\Delta E_{am} = E(\text{M-MOF-16}) + E(\text{am}) - E(\text{am:M-MOF-16}),$$

$$\Delta E_b = E(\text{am:M-MOF-16}) + nE(\text{H}_2) - E(\text{am:M-MOF-16:nH}_2),$$

where  $E(\text{am:M-MOF-16})$ ,  $E(\text{M-MOF-16})$  and  $E(\text{am})$  denote the total energies of alkali metal trapped at a particular adsorption site in M-MOF-16 host, intrinsic M-MOF-16 and the alkali metal, respectively. Moreover, we defined the total energy of  $n\text{H}_2$  adsorbed on am:M-MOF-16 structure as  $E(\text{am:M-MOF-16:nH}_2)$  and the total energy of free hydrogen molecule is symbolized by  $E(\text{H}_2)$ . Both alkali metal binding energies and hydrogen adsorption energies ranging from  $1\text{H}_2$  to  $4\text{H}_2$  loadings at all considered adsorption sites are presented in Figures 3.14 and 3.15, respectively. To check the accuracy of our results, the equilibrium distances as well as hydrogen binding energies at hex2 site calculated by us are compared to other closely relevant systems e.g. Li decorated MOF-5 [16, 127] as presented in Table 1 of Paper IV. We found that our results are in very good agreement with the available data for both DFT and MP2 results of Li-functionalized MOF-5.

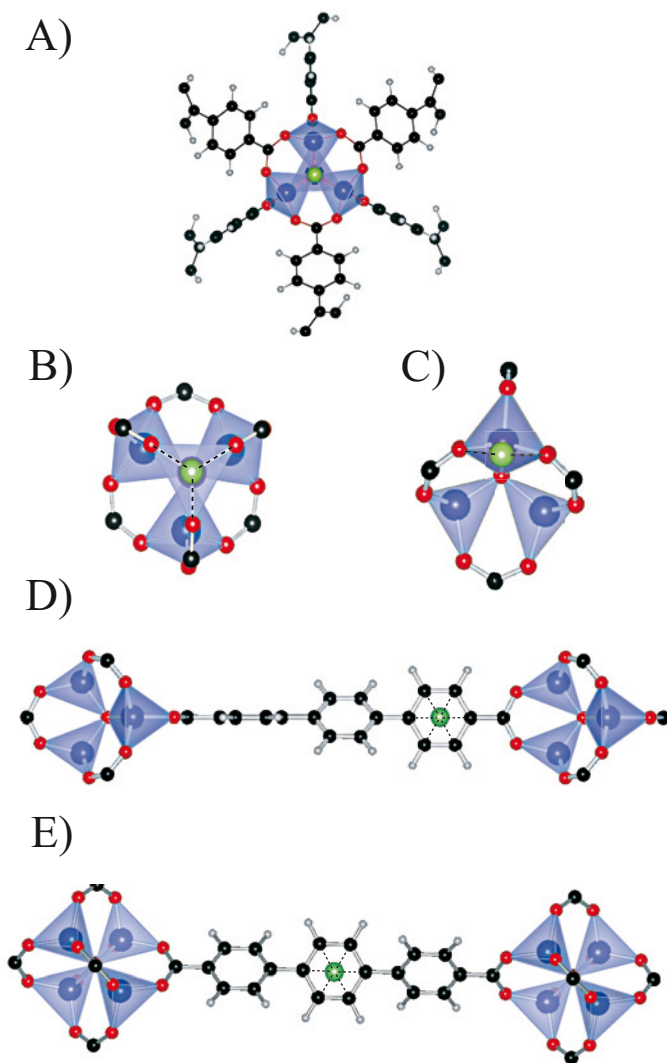


*Figure 3.13:* Metal binding sites in M-MOF-16 ( $M = \text{Zn}, \text{Mg}$  and  $\text{Ca}$ ). A) Cup site which is at an adsorption site on the center of three  $\text{MO}_4$  tetrahedra. B)  $\text{MO}_3$  site. C)  $\text{MO}_2$  site. D) Hex1 site. E) Hex2 site. The colors indicate the various elements in the M-MOF-16 framework as follows: metal atom  $M$  (blue spheres at center of transparent tetrahedra), oxygen (red), carbon (black), hydrogen (white), and metal binding sites (green).

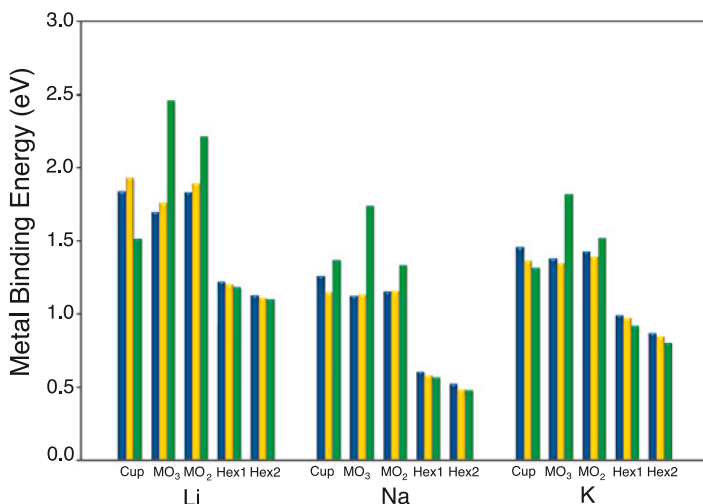
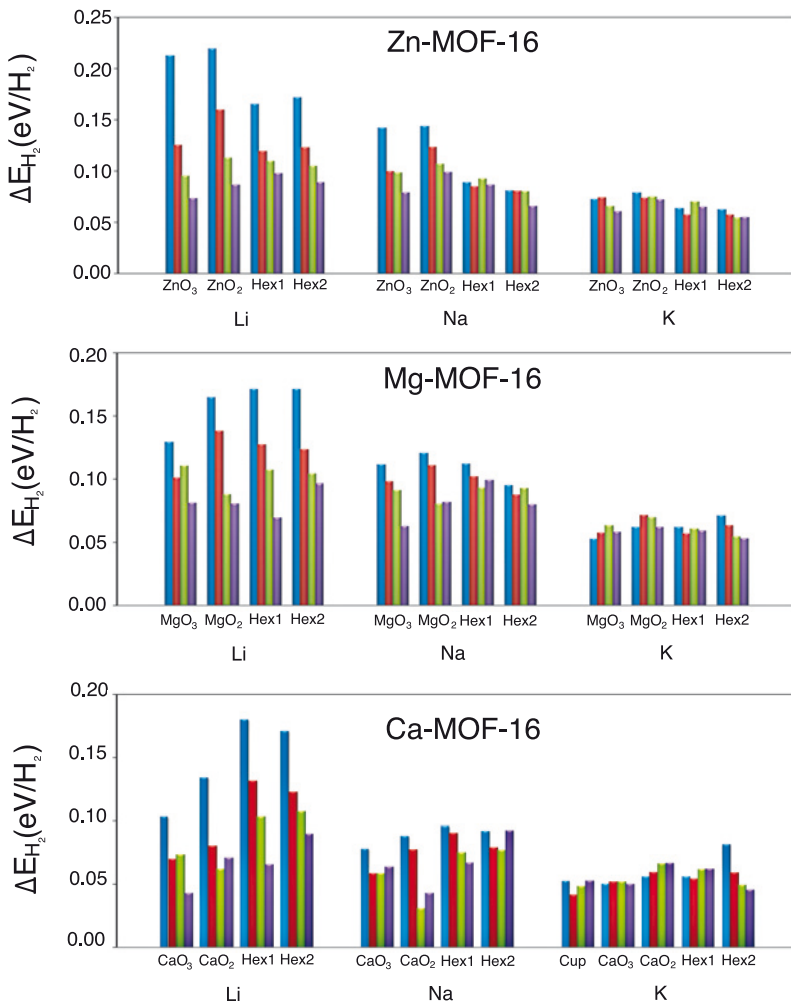


Figure 3.14: Metal binding energies ( $\Delta E_{am}$ ) of Li, Na, and K decoration in Zn-, Mg-, and Ca-MOF-16 at all studied adsorption sites (a detailed description of these adsorption sites is graphically given in Figure 3.13). The heights of blue, yellow and green bars indicate the magnitude of the metal binding energies corresponding to Zn-, Mg-, and Ca-MOF-16, respectively.

For an alkali metal initially trapped at the ideal cup site, we found that it moves to a location in between the ideal cup site and ideal MO<sub>2</sub> site with the deviation distances between these sites provided in Table 2 of paper IV. This is because the ideal cup site is rather far from the host frameworks, leading to weak interaction between alkali metal and host material. Consequently, the alkali metal starts to deviate from the ideal cup site, so that the atomic orbitals between metal and host materials can overlap. We would like to emphasize that the  $\Delta E_{am}$  of cup site reported in Figure 3.14 are the metal binding energies after performing the full optimization. As shown in Figure 3.14, it is clearly seen that metal binding energies at the adsorption sites near metal oxide cluster are higher than those at the organic linker sites due to the large distortion of the host framework when the alkali metal is trapped close to the adsorption site, resulting in a lowering of the total energy.

By considering the metal binding energy as a function of the size of alkali metals, our results reveal that Li yields the strongest metal binding energy among Na and K. This is because Li is trapped closest to the host and hence more overlapping of Li states to the host framework's states is found in our density of states plots in comparison to Na and K (see supporting information of Paper IV). Moreover, our results also revealed that the metal binding energies of K are always higher than those of Na, opposite to the trend of electronegativity and atomic radius. This finding is not only observed in MOF-16 but also in graphite [128] and single-walled carbon nanotubes [129]. To un-



*Figure 3.15:* Hydrogen adsorption energies ( $\Delta E_{H_2}$ ) at different levels of hydrogen loading ( $n=1-4H_2$ ) adsorbed on Li, Na, and K decorations at all studied adsorption sites of Zn-, Mg-, and Ca-MOF-16. The colors label the different degrees of hydrogen loading:  $1H_2$  (blue),  $2H_2$  (red),  $3H_2$  (green), and  $4H_2$  (purple). Except for K-decorated Ca-MOF-16, other alkali metals exhibit large deviations from the ideal position of cup site (see Table 2 of paper IV) and therefore the corresponding binding energies of these cases are omitted here.

derstand this result, the density of states of all considered alkali adsorption cases in MOF-16 is investigated and our density of states plots revealed that valence states of K give stronger overlapping with the host material states than those of Na. Moreover, we found that the lower  $p$  states of K also contribute to the metal binding energy but this contribution is not found in Na due to rather deep-lying Na  $2p$  states.

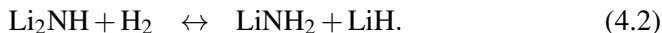
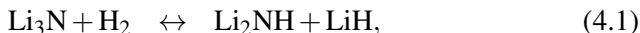
By considering the metal binding energies at the sites close to metal oxide cluster as a function of the size of the host framework,  $\text{MO}_2$  and  $\text{MO}_3$  adsorption sites of Ca-MOF-16 are found to be the highest metal binding energies because of the most distorted crystal structure among both Zn- and Mg-MOF-16. Due to the almost equivalent in crystal geometries of Zn-MOF-16 and Mg-MOF-16, the metal binding energies of these host frameworks are almost equal, however, there is no relationship at the cup site between metal binding energies and size of host framework. For the adsorption sites on the organic linker, the distortion of the metal oxide cluster does not affect much the alkali adsorption in the organic linkers, leading to almost equal metal binding energies. We found that the metal binding energies yield the following trend:  $\Delta E_{am}(\text{Zn-MOF-16}) > \Delta E_{am}(\text{Mg-MOF-16}) > \Delta E_{am}(\text{Ca-MOF-16})$ .

In terms of hydrogen adsorption energy as a function of alkali metal size (Figure 3.15), Li gives the highest hydrogen binding energy followed by Na and K. This finding is in good agreement with experimental results reported by Mulfort *et al.* [130]. Moreover, our results reveal that a decrease in the hydrogen binding energies for the adsorption sites near the metal oxide cluster is found when the size of the metal oxide cluster is increased, whereas they are found to be almost indifferent for the adsorption sites at the organic linker. For instance, by trapping a single  $\text{H}_2$  molecule on Li decorating the  $\text{MO}_2$  site of M-MOF-16 ( $M = \text{Zn, Mg, and Ca}$ ), hydrogen binding energies drop from 0.21 to 0.16 eV, and from 0.16 to 0.13 eV when the host material is changed from Zn-MOF-16 to Mg-MOF-16, and from Mg-MOF-16 to Ca-MOF-16, respectively, whereas the hydrogen adsorption energies of the sites on the TPDC linker are seen to remain constant, namely about 0.17 eV. Among the studies of the three alkali metals decorated in three different host systems, we found that Li-decoration in Zn-MOF-16 appears to be the best choice to obtain the highest hydrogen adsorption energy.

To summarize, DFT calculations have been carried out to investigate the best combination of three different host frameworks and decorating alkali metals, with both metal binding energy and hydrogen adsorption energies being the criteria. Our results reveal that metal binding energies of Li are the highest followed by K and Na. Among all studied frameworks, Ca-MOF-16 gives the highest metal binding energy due to the most distorted host in comparison to Zn- and Mg-MOF-16. By considering the hydrogen binding energies from all studied combinations, Li-decoration in Zn-MOF-16 is found to be the best choice among the nine combinations studied by us.

## 4. Li-N-H Systems

Currently, materials containing highly mobile ions or superionic materials have been shown much attention especially in electrolytes of fuel cell and hydrogen storage applications [26, 131–138].  $\text{Li}_3\text{N}$  is one example of the light element superionic solids in which Li is very mobile. In addition, both theorists and experimentalists [139–145] have paid considerable attention to this compound as a promising hydrogen storage material due to the rather high reported hydrogen capacity (about 9.3 wt% [26]). The hydrogenation reaction of this compound is the following two-step reversible reactions [26]



According to Eq. 4.1, lithium nitride ( $\text{Li}_3\text{N}$ ) is hydrogenated to form lithium imide ( $\text{Li}_2\text{NH}$ ) and lithium hydride ( $\text{LiH}$ ) at temperature 170 – 210 °C [140, 145]. Further hydrogenation of the  $\text{Li}_2\text{NH}$ , the lithium amide ( $\text{LiNH}_2$ ) and  $\text{LiH}$  are formed (Eq. 4.2) at 255 °C. In the reverse reaction,  $\text{LiNH}_2$  starts to non-stoichiometrically decompose to  $\text{Li}_2\text{NH}$ , and  $\text{H}_2$  is released at temperature less than 200 °C. Finally,  $\text{Li}_2\text{NH}$  is transformed back to  $\text{Li}_3\text{N}$  at a rather high temperature, namely 320 °C. For the above reactions, we would like to emphasize that they are reversible without requiring any catalyst.

In this chapter, we investigate the Li diffusions by means of the mean square displacement, diffusion coefficient and bond angle distribution of the  $\text{Li}_3\text{N}$ ,  $\text{Li}_2\text{NH}$  and  $\text{LiNH}_2$  via the *ab initio* MD simulations as discussed in Section 4.1. Moreover, theoretical investigation on the reaction mechanism of the dehydrogenation step in Eq. (4.2) due to  $\text{Li}^+$  and proton migrations inside  $\text{LiNH}_2$  and between  $\text{LiNH}_2$  and  $\text{LiH}$  is discussed in Section 4.2.

### 4.1 Roles of hydrogen in the Li-N-H system

In paper VI, we investigate the Li and N diffusions in three different compounds in the Li-N-H system, namely  $\text{Li}_3\text{N}$ ,  $\text{Li}_2\text{NH}$  and  $\text{LiNH}_2$ . As mentioned before, the last two compounds can be obtained from stepwise hydrogenation of  $\text{Li}_3\text{N}$ . For initial configurations, the  $\text{Li}_3\text{N}$  and  $\text{LiNH}_2$  crystal structures possess  $P6/mmm$  and  $\bar{1}4$  space groups, respectively. Detail descriptions of these structures can be found in Refs. 146 and 147. In  $\text{Li}_2\text{NH}$ , the crystal structure is chosen from the high-temperature phase (space group  $\text{Fm}\bar{3}m$  [136]). How-

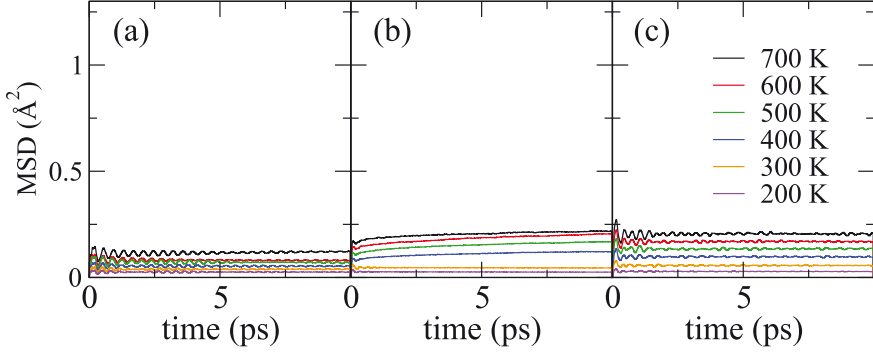


Figure 4.1: Mean square displacements of N in the a)  $\text{Li}_3\text{N}$ , b)  $\text{Li}_2\text{NH}$  and c)  $\text{LiNH}_2$ . Note that the scales on y-axis for all panels are identical.

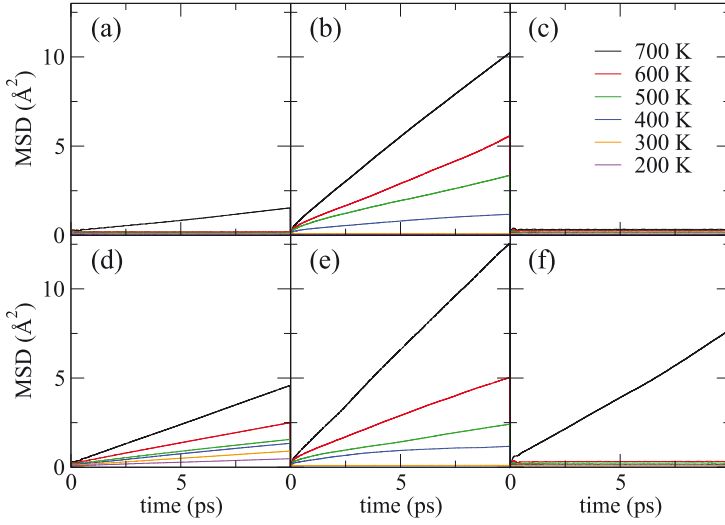


Figure 4.2: Temperature dependence mean square displacements of Li diffusions in a)  $\text{Li}_3\text{N}$ , b)  $\text{Li}_2\text{NH}$  and c)  $\text{LiNH}_2$ . The MSD of Li with insertion one Li vacancy. d)  $\text{Li}_3\text{N}$ . e)  $\text{Li}_2\text{NH}$  and f)  $\text{LiNH}_2$ . The vertical scales are identical scale for all six panels.



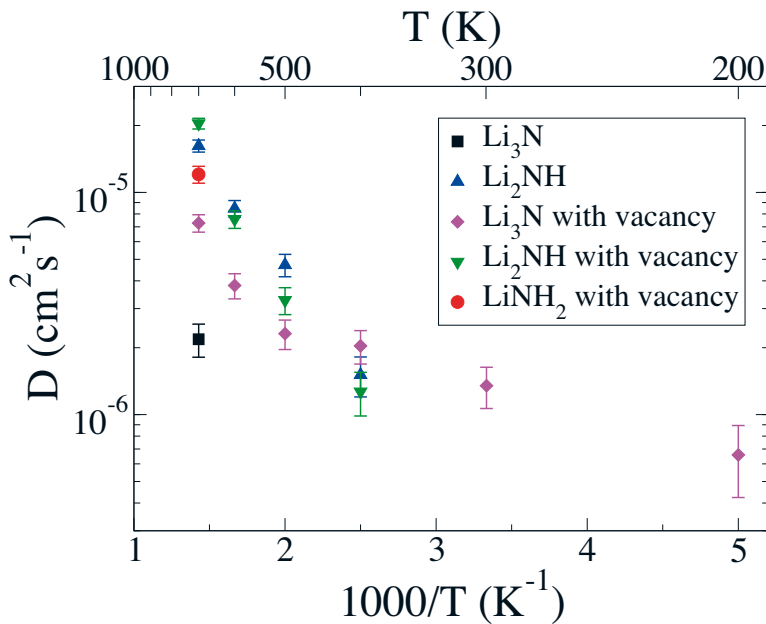


Figure 4.3: Diffusion coefficients calculated from the MSD of the  $\text{Li}_3\text{N}$ ,  $\text{Li}_2\text{NH}$  and  $\text{LiNH}_2$  with and without introduction of a Li vacancy.

ever, we found that the structure after 10 ps of equilibrate time does not relate to the initially chosen structure. Hence all extracted results after thermodynamics equilibration are unaffected by the initial crystal structure. To investigate the Li movement, the first-principles molecular dynamics simulations at temperature ranging from 200 to 700 K are carried out in order to obtain the temperature dependent MSD, diffusion coefficients and BAD of these three compounds. Detailed description of these calculated quantities was already illustrated in Section 2.1.8.

From Figure 4.1a–c, it is clearly seen that the MSD of N in these three compounds are flat for the whole range of temperature which indicates that N stays at their initial positions (or oscillates around the equilibrium positions), whereas lithium ions are mobile, as shown in Figure 4.2a and 4.2b.

In  $\text{Li}_3\text{N}$ , N carries a charge state of 3- and has strong Coulomb attraction to Li ions. Moreover, full occupation of Li ions in the  $\text{Li}_3\text{N}$  leads to difficulty for Li movement from one site to another site. At  $T = 700$  K, Li is able to overcome the energy barrier to leave the equilibrium position, and a Frenkel defect is created, which allow for the adjacent Li ion to hop. This can be clearly seen by the MSD plot as show in Figure 4.2a. If a Li vacancy is created either by applying external force or inhomogeneity of the  $\text{Li}_3\text{N}$ , Figures 4.2c and 4.3 confirm that there is a dramatical improvement of the Li mobility because the finite slope of the MSD plots is observed at much lower temperatures (less

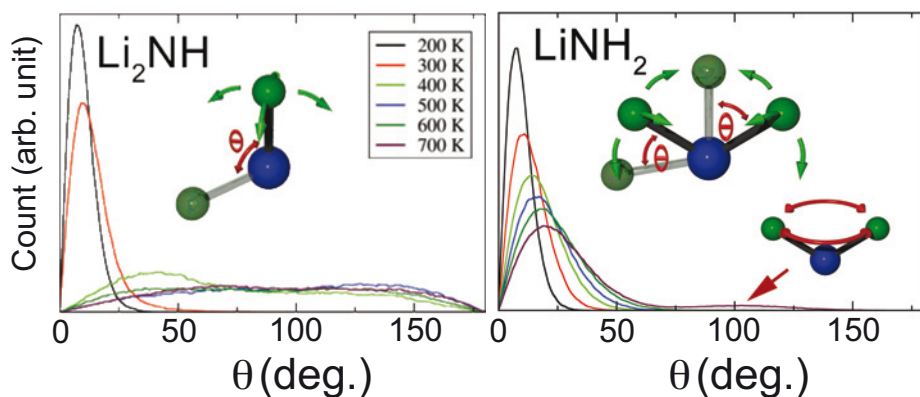


Figure 4.4: Bond angle distribution plots of the N–H bond in  $\text{Li}_2\text{NH}$  (left panel) and  $\text{LiNH}_2$  (right panel). Angle  $\theta$  refers to the angle of N–H bond deviated from the zero kelvin N–H orientation as present in both panels.

than 200 K), whereas Li ions start to be mobile at 700 K for the homogeneous  $\text{Li}_3\text{N}$ .

In  $\text{Li}_2\text{NH}$ , it can be comparable to the  $\text{Li}_3\text{N}$  by replacing one Li in the  $\text{Li}_3\text{N}$  with H anchored to N by forming  $\text{NH}^2$  unit. This leads to a more open space structure where lithium can diffuse. The increment of open space in the  $\text{Li}_2\text{NH}$  enhances the Li diffusion compared to the  $\text{Li}_3\text{N}$  as presented in Figures 4.2b and 4.3. At temperatures below 400 K, the partially positive hydrogen in the  $\text{NH}^2$  unit is aligned in a particular direction in order to minimize the electrostatic interaction between the  $\text{Li}^+$  ions and  $\text{NH}^2$  units. As a consequence, Li ions do not start to migrate at these temperatures as shown in Figure 4.2b. Above 400 K, both MSD and BAD results consistently showed that Li is very mobile (Figure 4.2b) and hydrogen in the  $\text{NH}^2$  units freely rotates around nitrogen atom (Figure 4.4). This is presumably because the partially positive charge of hydrogen in the  $\text{NH}^2$  units promotes the  $\text{Li}^+$  diffusion through momentum transfer between  $\text{Li}^+$  and  $\text{NH}^2$  (in form of electrostatic interaction between  $\text{Li}^+$  and  $\text{H}^+$  in the  $\text{NH}^2$  unit). For this case, H acts as a “promoter”, leading to enhance the Li mobility. As can be seen from both MSD (Figure 4.2e) and diffusion coefficient (Figure 4.3) plots, there is no any enhancement of Li diffusion in the  $\text{Li}_2\text{NH}$  after introducing a Li vacancy.

Compared to  $\text{Li}_3\text{N}$ ,  $\text{LiNH}_2$  consists of one Li and the two other Li are replaced by two H connected with N to form  $\text{NH}_2$ . This might, in principle, get more free space for Li movement and leads to increasing in Li mobility. However, the situation in the  $\text{LiNH}_2$  is different from the  $\text{Li}_2\text{NH}$  due to the effects from the H orientation. In the  $\text{LiNH}_2$ , a Li ion is tetrahedrally surrounded by the  $\text{NH}_2$  units and each unit possesses two partially positively charged hydrogen ions and one negatively charged nitrogen ion. From our MD simulations,

we found that H ions are still rotated in the  $\text{NH}_2^-$  units (see Figure 4 in paper V) but their rotations are not as free as the  $\text{NH}_2^-$  units in the  $\text{Li}_2\text{NH}$  due to repulsive interaction of each hydrogen ion leading to blockage of Li diffusion. This results in difficulty for Li to escape from the surrounding  $\text{NH}_2^-$  units. As a consequence, mobility of Li is dropped due to the obstacle of the H ions of the  $\text{NH}_2^-$  units. This leads to the final conclusion that hydrogen ions in  $\text{LiNH}_2$  act as an “inhibitor”, reducing the Li mobility as presented in Figure 4.2c. Finally, we also found in Figure 4.2f that insertion of a Li vacancy in the  $\text{LiNH}_2$  shows a small improvement of Li diffusion.

In summary, we demonstrate the Li diffusion by using *ab initio* molecular dynamics simulations and found that existence of hydrogen in  $\text{Li}_2\text{NH}/\text{LiNH}_2$  leads to two different situations: H acts as “promoter” and “inhibitor” of Li diffusions in the  $\text{Li}_2\text{NH}$  and  $\text{LiNH}_2$ , respectively. In  $\text{Li}_2\text{NH}$ , we found that H ion supports the Li diffusion through the momentum transfer between Li and  $\text{NH}_2^-$  units, while H ions in the  $\text{LiNH}_2$  hinder the Li mobility because Li is blockaded by the surrounded  $\text{NH}_2^-$  units yielding to reduction of Li mobility.

## 4.2 Thermodynamics of $\text{Li}^+$ and $\text{H}^+$ migrations in $\text{LiNH}_2$

In previous section, it was shown that the roles of hydrogen on Li diffusion in  $\text{LiNH}_2$  and  $\text{Li}_2\text{NH}$  are completely different, namely hydrogen atoms acting as inhibitor and promoter for Li migrations in  $\text{LiNH}_2$  and  $\text{Li}_2\text{NH}$ , respectively. However, other points of interest for this system are thermodynamic and kinetic studies of  $\text{Li}^+$  and  $\text{H}^+$  diffusions in the mixture between  $\text{LiNH}_2$  and  $\text{LiH}$  in order to understand the reaction mechanism in dehydrogenation step of Eq. 4.2. Currently, two models for describing this reaction mechanism from two different experiments are suggested. Chen *et al.* [148] proposed that reaction between  $\text{H}^-$  (from  $\text{LiH}$ ) and  $\text{H}^+$  (from  $\text{LiNH}_2$ ) results in forming the  $\text{H}_2$  and the  $\text{Li}_2\text{NH}$  can be formed by reaction between the  $\text{Li}^+$  (from  $\text{LiH}$ ) and  $\text{N}^-$  (in  $\text{LiNH}_2$ ). Another approach suggested by Ichikawa *et al.* [142] and David *et al.* [145] is that the non-stoichiometric mechanism of Eq. 4.2 are discussed as follows. First,  $2\text{LiNH}_2$  decomposes to  $\text{LiLiNH}_2^+$  and  $\text{NH}_2^-$  due to the  $\text{Li}^+$  movements inside the  $\text{LiNH}_2$ . Next, proton ( $\text{H}^+$ ) moves back from the  $\text{LiLiNH}_2^+$  to the  $\text{NH}_2^-$  unit and now  $\text{Li}_2\text{NH}$  and  $\text{NH}_3$  are formed. Then, the newly formed  $\text{NH}_3$  rapidly interacts with  $\text{LiH}$  to form  $\text{LiNH}_2$  and  $\text{H}_2$  [138, 142]. The  $\text{LiNH}_2$  is again decomposed to the  $\text{Li}_2\text{NH}$  and  $\text{NH}_3$  and thus its amount is gradually decreased transforming completely to  $\text{Li}_2\text{NH}$  (as present in Eq. 4.2).

In paper VI, all possible reaction paths related to the  $\text{Li}^+$  and  $\text{H}^+$  migrations in both inside the  $\text{LiNH}_2$  and between  $\text{LiNH}_2$  and  $\text{LiH}$  are investigated and then we made the reaction energy comparison to obtain the most favorable reaction paths for the migration of charged species. For  $\text{LiNH}_2$  and  $\text{LiH}$  crystal

Reactions	Reaction energy (eV)
<b>A1.</b> $\text{Li}_{32}\text{N}_{32}\text{H}_{64} + \text{Li}_{32}\text{H}_{32} \rightarrow \text{Li}_{31}\text{N}_{32}\text{H}_{64}^- + \text{Li}_{33}\text{H}_{32}^+$	+3.0365
<b>A2.</b> $\text{Li}_{32}\text{N}_{32}\text{H}_{64} + \text{Li}_{32}\text{H}_{32} \rightarrow \text{Li}_{33}\text{N}_{32}\text{H}_{64}^+ + \text{Li}_{31}\text{H}_{32}^-$	+0.0399
<b>A3.</b> $\text{Li}_{32}\text{N}_{32}\text{H}_{64} + \text{Li}_{32}\text{H}_{32} \rightarrow \text{Li}_{32}\text{N}_{32}\text{H}_{65}^+ + \text{Li}_{32}\text{H}_{31}^-$	+2.2418
<b>A4.</b> $\text{Li}_{32}\text{N}_{32}\text{H}_{64} + \text{Li}_{32}\text{H}_{32} \rightarrow \text{Li}_{32}\text{N}_{32}\text{H}_{63}^- + \text{Li}_{32}\text{H}_{33}^+$	+3.3966
• $\text{Li}^+$ and $\text{H}^+$ migrations from reaction <b>A2</b>	
<b>A5.</b> $\text{Li}_{33}\text{N}_{32}\text{H}_{64}^+ + \text{Li}_{31}\text{H}_{32}^- \rightarrow \text{Li}_{34}\text{N}_{32}\text{H}_{64}^{2+} + \text{Li}_{30}\text{H}_{32}^{2-}$	-0.3049
<b>A6.</b> $\text{Li}_{33}\text{N}_{32}\text{H}_{64}^+ + \text{Li}_{31}\text{H}_{32}^- \rightarrow \text{Li}_{33}\text{N}_{32}\text{H}_{63} + \text{Li}_{31}\text{H}_{33}$	+2.5718
• $\text{Li}^+$ and $\text{H}^+$ migrations from reaction <b>A5</b>	
<b>A7.</b> $\text{Li}_{34}\text{N}_{32}\text{H}_{64}^{2+} + \text{Li}_{30}\text{H}_{32}^{2-} \rightarrow \text{Li}_{35}\text{N}_{32}\text{H}_{64}^{3+} + \text{Li}_{29}\text{H}_{32}^{3-}$	-0.3827
<b>A8.</b> $\text{Li}_{34}\text{N}_{32}\text{H}_{64}^{2+} + \text{Li}_{30}\text{H}_{32}^{2-} \rightarrow \text{Li}_{34}\text{N}_{32}\text{H}_{63}^+ + \text{Li}_{30}\text{H}_{33}^-$	+2.8645
<b>A9.</b> $\text{Li}_{34}\text{N}_{32}\text{H}_{63}^+ + \text{Li}_{30}\text{H}_{33}^- \rightarrow \text{Li}_{34}\text{N}_{32}\text{H}_{62} + \text{Li}_{30}\text{H}_{34}$	+2.8006
• $\text{H}^+$ migrations from reaction <b>A7</b>	
<b>A10.</b> $\text{Li}_{35}\text{N}_{32}\text{H}_{64}^{3+} + \text{Li}_{29}\text{H}_{32}^{3-} \rightarrow \text{Li}_{35}\text{N}_{32}\text{H}_{63}^{2+} + \text{Li}_{29}\text{H}_{33}^{2-}$	+3.3301
<b>A11.</b> $\text{Li}_{35}\text{N}_{32}\text{H}_{63}^{2+} + \text{Li}_{29}\text{H}_{33}^{2-} \rightarrow \text{Li}_{35}\text{N}_{32}\text{H}_{62}^+ + \text{Li}_{29}\text{H}_{34}^-$	+3.1366
<b>A12.</b> $\text{Li}_{35}\text{N}_{32}\text{H}_{62}^+ + \text{Li}_{29}\text{H}_{34}^- \rightarrow \text{Li}_{35}\text{N}_{32}\text{H}_{61} + \text{Li}_{29}\text{H}_{35}$	+3.0833

Table 4.1: the  $\text{Li}^+$  and  $\text{H}^+$  migrations between the  $\text{Li}_{32}\text{N}_{32}\text{H}_{64}$  and  $\text{Li}_{32}\text{H}_{32}$ . The plus/minus reaction energies indicate endothermic/exothermic reaction.

Reactions	Reaction energy (eV)
<b>B1.</b> $\text{Li}_{32}\text{N}_{32}\text{H}_{64} + \text{Li}_{32}\text{N}_{32}\text{H}_{64} \rightarrow \text{Li}_{31}\text{N}_{32}\text{H}_{64}^- + \text{Li}_{33}\text{N}_{32}\text{H}_{64}^+$	+0.8566
<b>B2.</b> $\text{Li}_{32}\text{N}_{32}\text{H}_{64} + \text{Li}_{32}\text{N}_{32}\text{H}_{64} \rightarrow \text{Li}_{32}\text{N}_{32}\text{H}_{63}^- + \text{Li}_{32}\text{N}_{32}\text{H}_{65}^+$	+2.0278
• $\text{Li}^+$ and $\text{H}^+$ migrations from reaction <b>B1</b>	
<b>B3.</b> $\text{Li}_{31}\text{N}_{32}\text{H}_{64}^- + \text{Li}_{33}\text{N}_{32}\text{H}_{64}^+ \rightarrow \text{Li}_{30}\text{N}_{32}\text{H}_{64}^{2-} + \text{Li}_{34}\text{N}_{32}\text{H}_{64}^{2+}$	+0.5768
<b>B4.</b> $\text{Li}_{31}\text{N}_{32}\text{H}_{64}^- + \text{Li}_{33}\text{N}_{32}\text{H}_{64}^+ \rightarrow \text{Li}_{31}\text{N}_{32}\text{H}_{65} + \text{Li}_{33}\text{N}_{32}\text{H}_{63}$	+0.9241
• $\text{Li}^+$ and $\text{H}^+$ migrations from reaction <b>B3</b>	
<b>B5.</b> $\text{Li}_{30}\text{N}_{32}\text{H}_{64}^{2-} + \text{Li}_{34}\text{N}_{32}\text{H}_{64}^{2+} \rightarrow \text{Li}_{29}\text{N}_{32}\text{H}_{64}^{3-} + \text{Li}_{35}\text{N}_{32}\text{H}_{64}^{3+}$	+0.2559
<b>B6.</b> $\text{Li}_{30}\text{N}_{32}\text{H}_{64}^{2-} + \text{Li}_{34}\text{N}_{32}\text{H}_{64}^{2+} \rightarrow \text{Li}_{30}\text{N}_{32}\text{H}_{65}^- + \text{Li}_{34}\text{N}_{32}\text{H}_{63}^+$	+1.5688
<b>B7.</b> $\text{Li}_{30}\text{N}_{32}\text{H}_{65}^- + \text{Li}_{34}\text{N}_{32}\text{H}_{63}^+ \rightarrow \text{Li}_{30}\text{N}_{32}\text{H}_{66} + \text{Li}_{34}\text{N}_{32}\text{H}_{62}$	+0.8656
• $\text{H}^+$ migrations from reaction <b>B5</b>	
<b>B8.</b> $\text{Li}_{29}\text{N}_{32}\text{H}_{64}^{3-} + \text{Li}_{35}\text{N}_{32}\text{H}_{64}^{3+} \rightarrow \text{Li}_{29}\text{N}_{32}\text{H}_{65}^{2-} + \text{Li}_{35}\text{N}_{32}\text{H}_{63}^{2+}$	+1.6517
<b>B9.</b> $\text{Li}_{29}\text{N}_{32}\text{H}_{65}^{2-} + \text{Li}_{35}\text{N}_{32}\text{H}_{63}^{2+} \rightarrow \text{Li}_{29}\text{N}_{32}\text{H}_{66}^- + \text{Li}_{35}\text{N}_{32}\text{H}_{62}^+$	+1.6743
<b>B10.</b> $\text{Li}_{29}\text{N}_{32}\text{H}_{66}^- + \text{Li}_{35}\text{N}_{32}\text{H}_{62}^+ \rightarrow \text{Li}_{29}\text{N}_{32}\text{H}_{67} + \text{Li}_{35}\text{N}_{32}\text{H}_{61}$	+0.5360

Table 4.2:  $\text{Li}^+$  and  $\text{H}^+$  migrations inside the  $\text{Li}_{32}\text{N}_{32}\text{H}_{64}$ . The positive sign of the reaction energies is referred as endothermic reaction.

structures, we employed  $2 \times 2 \times 1$  and  $2 \times 2 \times 2$  supercells for lithium amide and lithium hydride corresponding to stoichiometry  $\text{Li}_{32}\text{N}_{32}\text{H}_{64}$  and  $\text{Li}_{32}\text{H}_{32}$ , respectively. The total reaction energy can be simply calculated as the total energy difference between products and reactants. However, the reaction energies do not include zero-point vibrational energy. As shown by Miceli *et al.* [149], the zero-point vibrational energy shows to be rather small contributions in  $\text{LiNH}_2$  system, namely less than 0.1 eV. All considered reactions due to  $\text{Li}^+$  and  $\text{H}^+$  migrations between these compounds and the corresponding reaction energies are reported in Tables 4.1 and 4.2.

From Tables 4.1 and 4.2, we can see that  $\text{Li}^+$  migrations both between  $\text{LiH}$  and  $\text{LiNH}_2$  (Table 4.1) and inside  $\text{LiNH}_2$  (Table 4.2) seem to be easy because of rather low reaction energy. However,  $\text{H}^+$  migrations from lithium amide to lithium hydride (forming  $\text{H}_2$  in  $\text{LiH}$ ) are found to be very difficult (see reactions A6, A8–A12 in Table 4.1), namely ranged from 2.57 to 3.33 eV. As can be seen from reactions B4 and B6–B10 of Tables 4.2, the  $\text{H}^+$  ions moved from one  $\text{NH}_2^-$  unit to another  $\text{NH}_2^-$  unit by forming  $\text{NH}_3$  via Grotthuss mechanism [150] (see Figure 1 of paper VI) are easier than the  $\text{H}^+$  diffusions from  $\text{LiNH}_2$  to  $\text{LiH}$  because of lowering in the reaction energies. The easiness in the  $\text{H}^+$  migrations inside lithium amide results in favoring the formation of  $\text{NH}_3$  as an intermediate step in the process of releasing  $\text{H}_2$  gas. Hence our results support the reaction mechanism proposed by Ichikawa *et al.* [142] and David *et al.* [145].

From our thermodynamic results, the  $\text{Li}^+$  and  $\text{H}^+$  diffusions inside the  $\text{LiNH}_2$  are found to be more favorable than those between  $\text{LiNH}_2$  and  $\text{LiH}$ . This finding is in good agreement with the experimental results [142, 145]. The reaction mechanism found by us is described with the following steps.  $\text{Li}^+$  ions are non-stoichiometrically migrated from one site in lithium amide to another site to form  $\text{Li}_2\text{NH}_2^+$  and  $\text{NH}_2^-$  units. Then  $\text{H}^+$  ions migrate back from the  $\text{Li}_2\text{NH}_2^+$  to  $\text{NH}_2^-$  via the Grotthuss mechanism resulting in the formation of  $\text{Li}_2\text{NH}$  and  $\text{NH}_3$ . However, it is well known that  $\text{NH}_3$  can interact with  $\text{LiH}$  resulting in forming  $\text{LiNH}_2$  and  $\text{H}_2$  [151, 152]. Hence, the reaction between  $\text{NH}_3$  and  $\text{LiH}$  will not be considered here. The newly formed  $\text{LiNH}_2$  is gradually decomposed and finally it will be completely transformed into  $\text{Li}_2\text{NH}$ . It should be noted that this work deals with charge migrations between two isolated compounds, namely between  $\text{LiNH}_2$  and  $\text{LiH}$  and inside  $\text{LiNH}_2$ . Although the interaction at interfaces between these compounds which plays an significant role for this system is beyond our scope.

In conclusion, we investigate the reaction mechanisms of  $\text{Li}^+$  and  $\text{H}^+$  migrations both inside  $\text{LiNH}_2$  and between  $\text{LiNH}_2$  and  $\text{LiH}$  based on two suggested reaction mechanisms from experiments [142, 148]. Our results reveal that  $\text{Li}^+$  migrations for both cases are rather easy. However, the  $\text{H}^+$  migrations from  $\text{LiNH}_2$  to  $\text{LiH}$  are rather difficult in comparison to the  $\text{H}^+$  migrations inside  $\text{LiNH}_2$ . This results in easiness to form  $\text{NH}_3$  by the  $\text{H}^+$  migration from

one  $\text{NH}_2^-$  unit to another one in the  $\text{LiNH}_2$  and finally our results support the reaction mechanism proposed by Ichikawa *et al.* [142] and David *et al.* [145].

## 5. Ab Initio Random Structure Searching

To find the global minimum energy configuration of complex systems (molecules, clusters or solids), using only information from first-principles theory, is a challenge task due to the complicated potential energy surface (PES). Consequently, the appropriate approach is needed in order to reach the correct ground state configuration. Pickard and Needs [28–30] proposed a newly successful and simple technique to find the global minimum of the complex systems by a method so called “*Ab Initio* Random Structure Searching (AIRSS)”. This approach has been proved to be a powerful tool for predicting the stable configuration at various conditions [153]. For example, it is used to predict high pressure phase of silane ( $\text{SiH}_4$ ) [28] by revealing that the  $I4_1/a$  is a stable phase at about 50 GPa and the  $C2/c$  is theoretically found to be a stable structure at the pressure above 262.5 GPa. The stability of the  $I4_1/a$  phase was recently confirmed by X-ray diffraction experiment from Eremets *et al.* [154]. In addition, this method can accurately predict the high pressure phases of solid  $\text{H}_2$  [29] and  $\text{NH}_3$  [30] and  $\text{TeO}_2$  [35]. Not only perfect crystals but also defects can be studied by using the AIRSS. For example, Morris *et al.* [155] used this method to find the lowest-energy structure of crystalline silicon with three types of point defects, namely interstitial hydrogen, nitrogen and oxygen.

The AIRSS has previously shown to be the successful method to find the global minimum configuration of the complex systems based on a simple idea that numerous configurations of crystal structures are randomly generated and the ground state structure can be further obtained by the lowest enthalpy configuration. Schematic method of the AIRSS [28–30] represented in Figure 5.1 is described as following steps.

- (i) Unit cell space group is randomly selected.
- (ii) The lattice vectors of the unit cell are randomized. However, volume of the cell is constrained by the desired either volume or pressure.
- (iii) Coordinates of atoms are randomly inserted into the unit cell (with particular sets of subgroup) based on the stoichiometry of materials. To prevent strong repulsive between ions, the configurations will be rejected when inter-atomic distance between these two ions is shorter than the summation of those atomic radii.
- (iv) To obtain the enthalpy, high accuracy method e.g. DFT is performed with the random crystal structure.

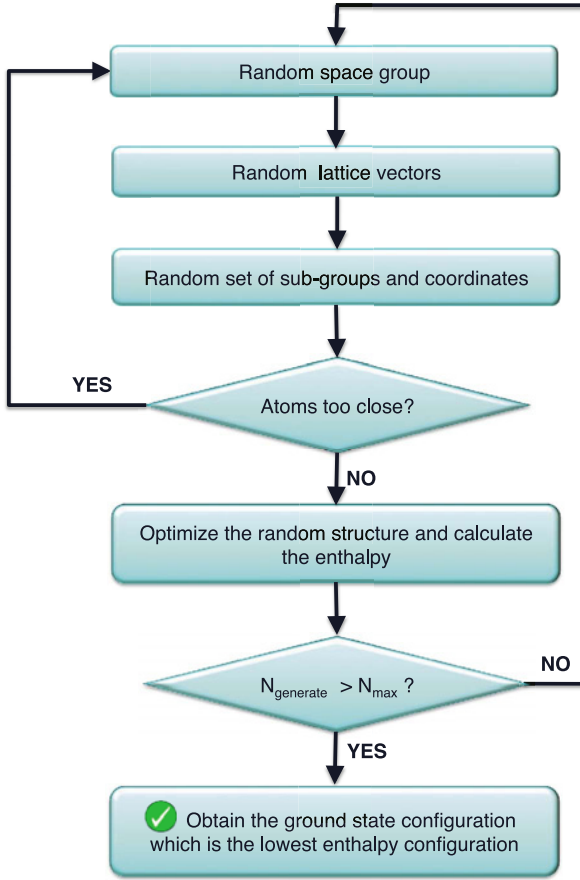


Figure 5.1: Schematic algorithm of the space group optimized *ab Initio* Random Structure Searching method.  $N_{\text{generate}}$  and  $N_{\text{max}}$  refer to number of generated random structures and maximum number of random structures, respectively.

(v) The random structures will be generated until numbers of generated random structure ( $N_{\text{generate}}$ ) larger than maximum number of random structures ( $N_{\text{max}}$ ).

To get the ground state configuration, enthalpy of each configuration is compared and the lowest enthalpy configuration is the ground state structure of the system. In next section, the AIRSS in conjunction with the DFT method will be applied to investigate the ground state structure of alkaline earth dicarbide systems.



## 5.1 Alkaline earth dicarbide systems

In 2007, Zaleski-Ejgierd *et al.* [156] investigated the crystal structures of alkaline earth dicarbide systems and they found that the lowest energy configuration of beryllium dicarbide ( $\text{BeC}_2$ ) is a sheet structure consisting of hexagonal rings of carbon surrounded by Be atoms. Various theoretical and experimental studies [157, 158] revealed that two dimensional carbonaceous materials consisting of hexagonal rings of carbon such as graphene have shown to be promising hydrogen storage materials. Based on this idea, the  $\text{BeC}_2$  might be possible to act as a promising hydrogen storage material. However, we encountered a serious problem for the application of this proposed  $\text{BeC}_2$  as hydrogen storage material because its structure is found to be dynamically unstable due to rather large imaginary frequencies at the center of Brillouin zone. Hence, this difficulty motivates us to investigate the crystal structure of the  $\text{BeC}_2$ . Not only  $\text{BeC}_2$ , but the crystal structures of other alkaline earth dicarbides are also theoretically studied as presented below.

In alkaline earth dicarbide systems, various experimental results were generally found to possess a linear-type crystal structure [159, 160]. In magnesium dicarbide ( $\text{MgC}_2$ ), its crystal structure at room temperature is tetragonal with the space group  $P4_2/mnm$ .  $\text{C}_2$  dumbbells are aligned in the perpendicular direction of the tetragonal  $c$ -axis with 1.215 Å of C–C bondlength [161]. For the  $\text{CaC}_2$  crystal structure,  $I4/mmm$  space group of its unit cell is found from both experimental and theoretical studies [162, 163]. However, the only difference in crystal structure of both structures is the direction of the  $\text{C}_2$  alignment, namely parallel and perpendicular orientation of the  $\text{C}_2$  dumbbells to the tetragonal  $c$ -axis for  $\text{CaC}_2$  and  $\text{MgC}_2$ , respectively. In  $\text{SrC}_2$  and  $\text{BaC}_2$ , X-ray diffraction experiments revealed that crystal structure of these dicarbides at room temperature is analogous to that of  $\text{CaC}_2$  [164, 165]. For  $\text{BeC}_2$ , there is no ground state structure experimentally reported in the literature. To investigate the ground state configuration of  $\text{BeC}_2$ , results from first-principles calculations performed by Zaleski-Ejgierd *et al.* [156] showed that total energy of the sheet structure is lower than that of the chain structure which was commonly found in experiments of the other alkaline earth dicarbides. Although, as mentioned before, the harmonic vibrational frequencies at the center of the Brillouin zone ( $\Gamma$ -point) of the lowest energy sheet show strong imaginary frequencies (order of  $300i \text{ cm}^{-1}$ ) and thus this structure is ruled out for the correct ground state structure.

In paper VII, the ground state crystal structure of  $\text{BeC}_2$  is investigated by the AIRSS and DFT calculations. Our results reveal that the ground state configuration consists of the five-membered carbon ring ( $\text{C}_5$ ) connected to a carbon atom forming an infinitely repeated  $\text{C}_5\text{--C--}$  chain with Be ions trapped around this chain as shown in Figure 5.2. For simplicity, this infinite chain of our reported structure will be named as the “poly[hexadehydro(methylcyclopentadiene)] (abbreviated as PH-MCP)-like chain”. Moreover, we also

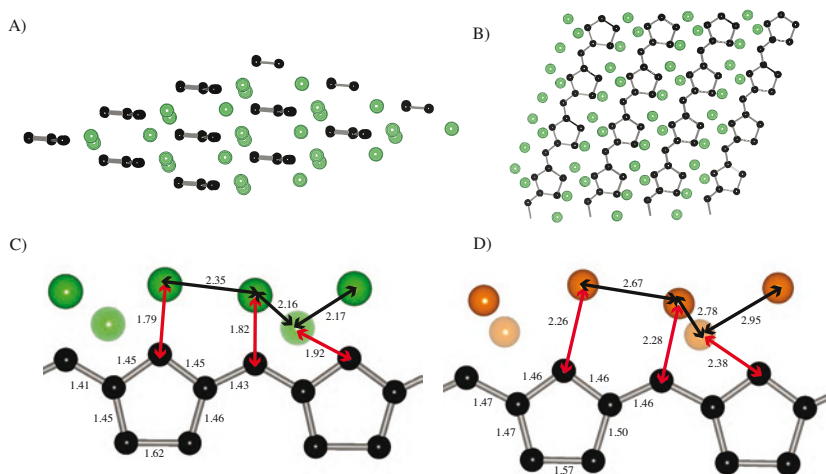


*Figure 5.2:* Lowest energy configuration of  $\text{BeC}_2$  and  $\text{MgC}_2$ . A) Side view. B) Top view. This configuration is rather similar to the PH-MCP anionic chain surrounded by alkaline earth ions. Light green and black spheres represent alkaline earth and carbon atoms, respectively. C) and D) structural parameters of  $\text{BeC}_2$  and  $\text{MgC}_2$  after optimization. The numbers which are in units of Å are denoted as the bond length between pair of atoms. For C) and D), Green, orange and black spheres are symbolized as Be, Mg and C atoms, respectively.

extend our study to other alkaline earth dicarbide systems e.g.  $\text{MgC}_2$ ,  $\text{CaC}_2$ ,  $\text{SrC}_2$  and  $\text{BaC}_2$ . Stability of all studied alkaline earth dicarbide systems is further discussed in Section 5.1.1. In Sections 5.1.2 and 5.1.3, the synthesis reaction paths and the electronic density of states of the PH-MCP-like structure of  $\text{BeC}_2$  and  $\text{MgC}_2$  will be illustrated.

### 5.1.1 Stability of alkaline earth dicarbide

It is well known that chain-type crystal structure is generally accepted as a ground state configuration for alkaline earth dicarbide systems [161–163]. This motivates us to make an energetic comparison between our PH-MCP-like and chain structures. As seen in Figure 5.3, the PH-MCP-like structure is found to be energetically more stable structure for  $\text{BeC}_2$  and  $\text{MgC}_2$ , whereas the chain-type crystal structures is more favorable than the PH-MCP-like structure for  $\text{CaC}_2$ ,  $\text{SrC}_2$  and  $\text{BaC}_2$ . A negative relative energy reported in Figure 5.3 is referred that the PH-MCP-like structure is energetically more favorable than the chain crystal structure, and vice versa, a positive value in relative-energy represents the chain type crystal structure as a stable structure.

For  $\text{BeC}_2$ , the PH-MCP-like crystal structure is found to be more energetically favorable than the chain crystal structure as shown in Figure 5.3.

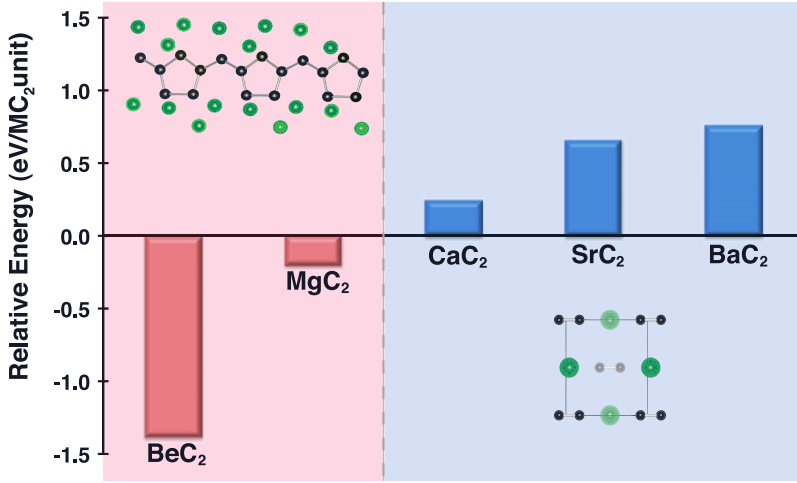


Figure 5.3: Energetic Comparison between the PH-MCP-like structure and chain structure in alkaline earth dicarbide systems. The PH-MCP-like structure is found to be stable (negative relative energy) for BeC<sub>2</sub> and MgC<sub>2</sub>, whereas the chain-type structure is seen to be the favoured crystal structure for other dicarbide systems.

Not only for chain crystal structure but also for all possible sheet structures proposed by Zaleski-Ejgierd *et al.* [156] are made an energetic comparison with this structure. We found that the PH-MCP-like crystal structure is significantly lower in energy than any of the sheet structures in the margin of 1.239 eV/MC<sub>2</sub> unit. This shows that the BeC<sub>2</sub> crystal structure proposed by us (Figure 5.2) yields a lower-energy configuration than both sheet and chain structures. Moreover, the PH-MCP-like crystal structure is found to be indeed stable confirmed by an *ab initio* molecular dynamics simulation (MD) at a simulated temperature of 500 K, because it is virtually unchanged in crystal structure after performing 5 ps of simulation time. To further test the dynamical stability of the BeC<sub>2</sub> ground state crystal structure, we calculated the vibrational frequencies at the center of the Brillouin zone ( $\Gamma$ -point) of the  $2 \times 2 \times 2$  BeC<sub>2</sub> supercell. The vibrational modes at the  $\Gamma$ -point can be more representative of the whole vibrational modes when large unit cell size is employed. Our results reveal that only negligibly small imaginary frequency ( $\sim 0.03i$  THz) is found in the PH-MCP-like crystal structure of BeC<sub>2</sub> due to the numerical inaccuracies. Based on our tests of both energetic and dynamical stabilities, the PH-MCP-like structure is the corrected ground state of BeC<sub>2</sub>.

For MgC<sub>2</sub>, Figure 5.3 shows that the PH-MCP-like crystal structure yields a lower total energy by about 0.203 eV/MC<sub>2</sub> unit than the common chain crystal structure reported from experiments [161]. Moreover, Zaleski-Ejgierd *et al.* [156] showed that chain structure is lower in total energy than the sheet structure for about 0.3 eV/MC<sub>2</sub> unit. As a results, the PH-MCP-like crystal

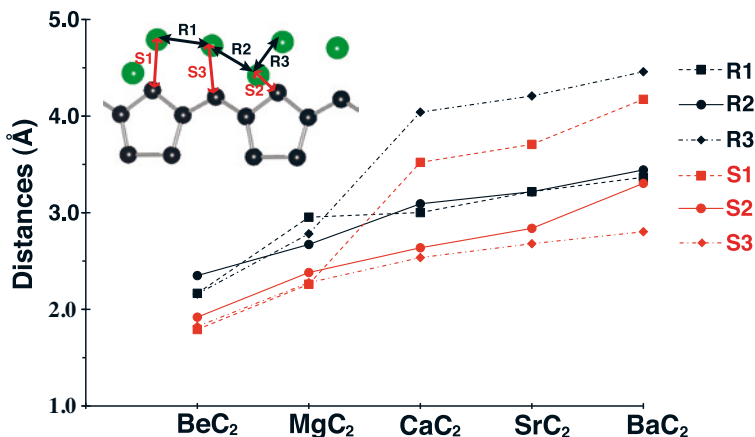


Figure 5.4: Structural parameters of PH-MCP-like crystal structure of all studied alkaline earth dicarbides. The  $M_{AE} - M_{AE}$  and  $M_{AE} - C$  ( $M_{AE} = \text{Be-Ba}$ ) distances are represented in black and red lines, respectively. The lines connected between points do not have any meaning but we just offer as a guide-line to represented the trend of the reported structural parameters. To avoid any ambiguousness of the S2 distances, We would like to note that the S2 distance is slightly larger than S3 distance because the corresponding Be atoms are trapped at deeper plane than the carbon chain's layer.

structure reported by us is the lowest energy compared to both sheet structures [156] and chain structures [161]. Again, to confirm the stability of this crystal structure, the vibrational frequencies at the  $\Gamma$ -point of the  $2 \times 2 \times 2$   $\text{MgC}_2$  supercell have been evaluated and our results reveal that no imaginary frequency exists at this point. In principle, these results imply that the chain crystal structure of  $\text{MgC}_2$  as observed in experiments could be a meta-stable state and its correct ground state is actually the predicted PH-MCP-like structure.

For  $\text{CaC}_2$ ,  $\text{SrC}_2$ , and  $\text{BaC}_2$ , our results show that the chain type crystal structure is the most favorable configuration, being lower in energy than the PH-MCP-like crystal structure. These findings are in very good agreement to the experimental results of these compounds[162, 164, 165].

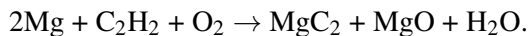
From Figure 5.3, it is clearly seen that increase in size of the alkaline earth metals leads to the chain crystal structure becoming more stabilized at the cost of a reduced stability of the PH-MCP-like crystal structure. This is due to the limited space for accommodating the alkaline earth ions around the PH-MCP-like chain resulting in the strong repulsion between each alkaline earth ions when size of alkaline earth ions are gained (sizes of alkaline earth metals based on Pauling ionic radii with charge +2 follows the trend: Be (0.31 Å) < Mg (0.65 Å) < Ca (0.99 Å) < Sr (1.18 Å) < Ba (1.35 Å)). As a result, the distance between each alkaline earth ion is increased (see R1–R3 in Figure 5.4) leading to an increase in total energy of the PH-MCP structure. Another possible reason to drop the stability of the PH-MCP-like structure is that equilibrium

distances between alkaline earth ion and the carbon atoms in the PH-MCP-like chain (shown as S1–S3 distances in Figure 5.4) are found to be gained with increasing ion size. This increasing in equilibrium distances leads to weakening in electrostatic interaction between ions and the chains.

In chain structure, the crystal structure is rather less disturbed when large ion is accommodated. This is because there is a lot of space between the alkaline earth ion and C<sub>2</sub> dumbbell. In addition, the repulsive interaction between each alkaline earth metal (which is strongly dominated in the PH-MCP-like crystal structure) is very weak due to rather far distance from each alkaline earth metal. Consequently, the disturbance to chain structure due to the alkaline earth ions is rather small when large ion is introduced, whereas this effect is rather dominant in the PH-MCP-like structure. Based on these reasons, stability of the PH-MCP-like crystal structure in the M<sub>AE</sub>C<sub>2</sub> (M<sub>AE</sub>= Be–Ba) is reduced when size of the M<sub>AE</sub> is increasing as seen in Figure 5.3 due to effects from repulsive interaction between each alkaline earth ion and from weaker interaction between the chain and M<sub>AE</sub>.

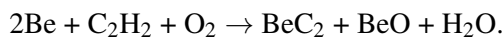
### 5.1.2 Reaction paths of beryllium and magnesium dicarbide

In experiment, MgC<sub>2</sub> can be synthesized by the following reaction:[161]



Based on our total energy calculations, the above reaction is exothermic reaction with  $-9.294$  eV/f. u. of reaction energy. To avoid any misunderstanding, the reaction energies reported here are the difference between total energy of reactants and products, and are not to be confused with the reaction enthalpies which are normally reported in experiments. In our studies, we found that the reaction energy of our reported MgC<sub>2</sub> is comparable to the calculated MgC<sub>2</sub> chain structure, namely  $-9.497$  and  $-9.294$  eV/f. u. for PH-MCP-like and chain MgC<sub>2</sub>, respectively. This result reveals that the crystal structure reported by us might be synthesized by using the above reaction.

For BeC<sub>2</sub>, we assume the analogous reaction,



From our calculations, this reaction exhibits exothermic behavior by releasing  $9.765$  eV/f. u. in the process. In comparison to the reaction energies between our BeC<sub>2</sub> and calculated chain structure of MgC<sub>2</sub> [161], our calculations found that the reaction energy of the BeC<sub>2</sub> is, again, comparable to the reaction energy of the experimental MgC<sub>2</sub> chain structure, namely  $-9.765$  and  $-9.294$  eV/f. u. for BeC<sub>2</sub> and chain MgC<sub>2</sub>, respectively. This can be regarded as an evidence that the new crystal structure of BeC<sub>2</sub> reported here by us might be synthesized by the above reaction.

It is important to note that choice of initial reagent may strongly affect the crystal structure of the final product. For instance, the chain-type crystal

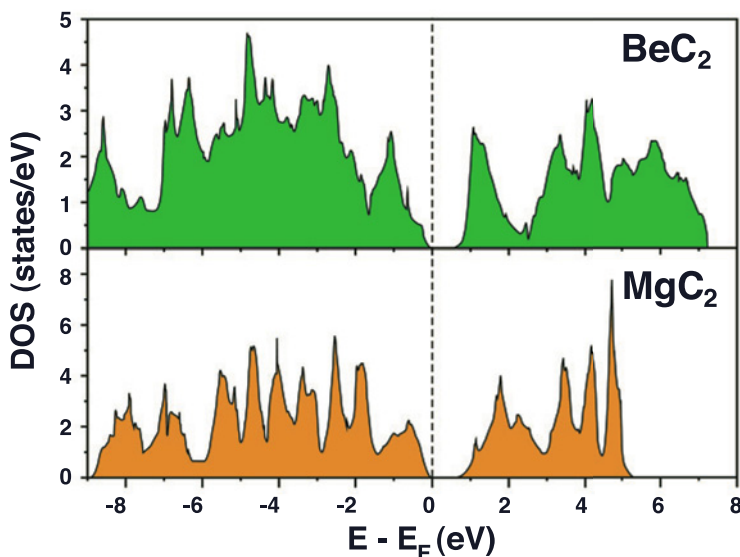


Figure 5.5: Density of states of the PH-MCP-like  $\text{BeC}_2$  and  $\text{MgC}_2$  crystal structures. Vertical dotted line is denoted as the Fermi energy level.

structure of  $\text{MgC}_2$  can be obtained when the acetylene ( $\text{C}_2\text{H}_2$ ), chain type molecules, is used as an initial reagent. Consequently, it might be possible to obtain the PH-MCP like structure as the final product if the five-membered carbon ring molecule such as cyclopentadienide is used as an initial reagents.

### 5.1.3 Density of states of beryllium and magnesium dicarbide

As can be seen in Figure 5.3, the lowest energy crystal structures of both  $\text{BeC}_2$  and  $\text{MgC}_2$  are the PH-MCP-like crystal structure. Here, the density of states of both systems is calculated as displayed in Figure 5.5.

As seen in Figure 5.5, the band gaps of the PH-MCP-like crystal structures are rather narrow, namely 0.51 and 0.60 eV for  $\text{BeC}_2$  and  $\text{MgC}_2$ , respectively, while the band gap of the chain  $\text{MgC}_2$  is about 3 eV. This band gap of the chain  $\text{MgC}_2$  reported by us is in very good agreement with that reported in the literature [160]. Due to rather significant difference in band gap, this might help the experimentalists to optically distinguish between these two structures.

In conclusion, we performed the AIRSS in combination with the DFT calculations to investigate the ground state crystal structure of  $\text{BeC}_2$ . From our results, the ground state structure of  $\text{BeC}_2$  is the PH-MCP-like chain with Be trapping around this chain. To extend our studies to other alkaline earth dicarbide systems such as  $\text{MgC}_2\text{--BaC}_2$ , we found that the lowest energy crystal structure of  $\text{MgC}_2$  is analogous to the  $\text{BeC}_2$  while chain-type crystal structure, commonly found in alkaline earth dicarbide systems, is the stable phase

for  $\text{CaC}_2$ ,  $\text{SrC}_2$  and  $\text{BaC}_2$ . Moreover, our results revealed that stability of the PH-MCP-like crystal structure is decreased in comparison to the chain type structure when ion size is increasing. This can be understood by the combination of the effects from repulsive interaction between each alkaline earth ions and weakening of the electrostatic interaction between alkaline earth ion and the PH-MCP-like chain. Based on our total energy calculations, the reaction,  $2\text{M} + \text{C}_2\text{H}_2 + \text{O}_2 \rightarrow \text{MC}_2 + \text{MO} + \text{H}_2\text{O}$  ( $\text{M} = \text{Be}$  and  $\text{Mg}$ ), exhibits exothermic reaction with reaction energy of  $-9.765$  and  $-9.497$  eV/f. u. for  $\text{BeC}_2$  and  $\text{MgC}_2$ , respectively. These reported reaction energies are comparable to  $-9.294$  eV/f. u. for the calculated reaction energy of the chain  $\text{MgC}_2$  observed in experiment. Finally, we also investigated the band gaps of these newly reported  $\text{BeC}_2$  and  $\text{MgC}_2$  structures and found that band gaps of these two systems are rather narrow i.e.  $0.51$  eV and  $0.60$  eV for  $\text{BeC}_2$  and  $\text{MgC}_2$ , respectively, whereas the band gap of the chain type  $\text{MgC}_2$  is found to be about  $3$  eV. This substantial difference in the electronic band gap leads possibility to optical distinction in experiments.





## 6. Sammanfattning på Svenska

Beräkningsvetenskap spelar idag en betydande roll som ett kraftfullt verktyg i flera områden inom materialvetenskap. Inom materialvetenskapen beräknar man numeriskt olika observerbara kvantiteter på atomär nivå. De stora fördelarna med materialberäkningsvetenskap är att den hjälper oss att förstå atomernas beteende i form av molekyler eller fasta ämnen genom teoretiska tolkningar. Dessutom kan man simulera tillstånd som är svåra att uppnå i experiment. En viktig faktor som bör beaktas i materialberäkningssammanhang är riktigheten i simuleringsresultaten. Tidigare klassiska metoder, baserat på Newtonsk mekanik, har visat sig vara ett kraftfullt verktyg i beräkningsvetenskapliga sammanhang eftersom de lätt kan behandla mycket stora system (miljoner atomer). Dock är noggrannheten för dessa metoder fortfarande problematisk. För närvarande visar sig förstaprinicipmetoden vara den mest lämpliga metoden för att studera fenomen på atomär nivå. Det på grund av att den ger mer exakta resultat än tidigare teoretiska metoder. Dessutom ger den allt större datorkraften möjlighet att simulera förhållandevis stora system, där det maximala antal atomer är i storleksordningen flera tusen. På grund av dessa skäl visar sig förstaprinicipmetoder, dvs densitetsfunktionalteori och Møller-Plesset störningsteori vara lämpliga val för att studera system i nanoskala. En detaljbeskrivning av densitetsfunktionalteori och Møller-Plesset störningsteori återfinns i kapitel 2.

Under 1900-talet kom det mesta av energiförsörjningen främst från fossila källor t.ex. råolja. Tyvärr producerar dessa energi källor skadliga gaser så som CO, CO<sub>2</sub> och SO<sub>2</sub>, vilka kommer ut i atmosfären och orsakar miljöproblem. Dessutom leder den enorma användningen av fossila bränslen, från huvudsakligen transporter och industrier, till en snabb utarmning icke förnybara energiresurser. Vätgasekonomin presenteras som en av de mer intressanta lösningarna för framtiden på grund av att väte är det vanligaste grundämnet på jorden (i form av vatten) och endast ger upphov till rena biprodukter vid förbränning. Ett annat skäl för att vätgasekonomin ses som en lovande energiresurs är att mass-energi-tätheten är ungefär tre gånger högre än hos nuvarande fossila bränslen. Men den volumetriska densiteten av vätgas är låg, 0,09 kg/m<sup>3</sup> för H<sub>2</sub>-gas, därför behövs det mycket plats för att lagra väte. Däri ligger problemet. För närvarande finns tre viktiga metoder för att lagra väte: i gasform, som flytande fas, eller bundet inuti ett material. Den mest lovande alternativet anses vara det tredje, där vätgas kan fångas in enligt

två huvudsakliga mekanismer, nämligen fysikalisk adsorption och kemisk absorption. I naturen förekommer vätgas som molekyl. När vätemolekylerna kommer i kontakt med det mottagande materialets yta binder de till ytan via inducerad dipol-dipol-interaktion eller van der Waals interaktion, och denna mekanism kallas fysikalisk adsorption. Vanligtvis är väteadsorptionsenergin enligt denna mekanism mycket svag, ofta mindre än 10 kJ/mol, och detta leder till att det går mycket snabbt att adsorbera/desorbera  $H_2$ . Dessutom har tidigare forskning funnit att material med stor intern adsorptionsyta skulle kunna ge ha en hög vätelagringskapacitet. Följaktligen förväntas t.ex. metallorganiska nätverk, kovalenta organiska nätverk, kolbaserade material m.m., vara lovande vätelagringsmaterial. Men det största hindret för att använda dessa material för vätelagring är främst att vätemolekyler desorberas i rumstemperatur, på grund av den mycket svaga växelverkan mellan  $H_2$  och värdmaterialet, vilket resulterar i förhållandevis låg gravimetrisk densitet av väte. På grund av dessa problem, undersöks i kapitel 3 metoder för att förbättra vätebindningsenergi i material med stor adsorptionsyta. I detta kapitel studeras ett antal tekniker för förbättra vätebindningsenergin i fysikaliskt adsorberande material, t.ex. metallorganiska nätverk och kovalenta organiska nätverk. En speciell typ av metallorganiskt nätverk är det s.k. MOF-5, som består av 1,4-bensendikarboxylatmolekyler (BDC), som i sin tur binds samman av  $Zn_4O$ -kluster, för att tillsammans bilda ett kubiskt repeterande nätverk. Våra studier visar att vätebindningsenergin i MOF-5 kan förbättras genom att öppna upp metalloxidklustren, vilket resulterar i högre polarisabilitet och kortare jämviktsbindningslängd mellan  $H_2$  och värdmaterialet, dvs en starkare bindning. Hos kovalenta organiska nätverk, här den s.k. COF-1-strukturen, består nätverket av två stycken identiskt staplade lager, precis som i grafit. I varje lager finns boroxinringar ( $B_3O_3$ ), där varje boratom binder till var sin bensenring, och på så sätt formar ett periodiskt nätverk. För COF-1 fann vi att effekter från  $H_2$ - $H_2$ -växelverkan också spelade en viktig roll i att förbättra vätebindningsenergierna. Men båda, ovan nämnda, tillvägagångssätt ger väteadsorptionsenergier som är lägre än den ideala bindingsstyrkan för praktiska tillämpningar, nämligen 10-60 kJ/mol. En annan strategi som har föreslagits är att introducera Li-atomer på ytan av den organiska bryggan i MOF-5, för att på detta sätt skapa ett isolerat, laddat, Li-tillstånd, som kan interagera med vätemolekylerna. Vi fann att väteadsorptionsenergierna är ca. 2-3 ggr högre än om  $H_2$ -molekylen adsorberas direkt på MOF-5-ytan. Uöver Li, så visades också att olika stora metallatomer, såsom Ca, Ti och Mg, kan förbättra väteadsorptionsenergin. Vi förväntade oss vidare att storleken på enhetscellen skulle kunna spela en signifikant roll i förbättringen av vätebindningsenergin. Dessa aspekter ledde oss till att i detalj undersöka effekterna av både metalldekoration och enhetscellens storlek på vätebindningsenergin. Tre stycken dekorerande metaller (Li, Na, K), och tre stycken isoretikulära MOF-16 nätverk (Zn-MOF-16, Mg-MOF-16, Ca-MOF-16) valdes i denna studie. Kristallstrukturen hos MOF-16 är nästan identisk med MOF-5, förutom en skillnad i den

organiska bryggan, som består av BDC i fallet MOF-5, och trifenyldikarboxylat (TPDC) i fallet MOF-16. Våra resultat avslöjar att Li-dekorat av M-MOF-16 (där  $M = \text{Zn, Mg, Ca}$ ) ger högre vätebidningsenergi än om dekorationen sker med Na eller K. Bland de studerade nätverken Zn-, Mg-, och Ca-MOF-16, fann vi att Zn-MOF-16 har den högsta vätebindningsenergi i närheten av metalloxidklustret, medan interaktionsenergierna med TPDC-ytan är närmast oförändrade för Zn-, Mg-, och Ca-MOF-16. Sammanfattningsvis verkar det som att Li-dekorat av Zn-MOF-16 är den bästa kombinationen för att få starkare vätebindningar.

En annan typ av material med stor potential som väteagransningsmaterial är de som uppvisar kemisk adsorption. Vid kemisk adsorption dissocieras vätemolekylerna först på värdmaterialens yta, och diffunderar sedan in i materialet, där de, i det fullt hydrerade tillståndet, bildar en hydrid. Exempel på kemiskt adsorberande material är t.ex.  $\text{MgH}_2$ , alanater:  $\text{NaAlH}_4$ ,  $\text{LiAlH}_4$ , borater:  $\text{LiBH}_4$ , Li-N-H-systemet m.m. I kapitel 4 diskuteras reaktionsmekanismer i dehydrogeneringsprocessen i blandningar mellan litiumamid ( $\text{LiNH}_2$ ) och litiumhydrid ( $\text{LiH}$ ). En upptäckt var att diffusion av  $\text{Li}^+$  joner och protoner lätt sker inom litiumamiden än mellan litiumamid och litiumhydrid. En annan intressant observation gjordes genom att studera väteatomernas rörelse i litiumimid och litiumamid via molekylodynamiksimuleringar gjorda ab initio. Våra resultat visar att väte har två roller, dels som promotor i  $\text{Li}_2\text{NH}$ , och dels som inhibitor i  $\text{LiNH}_2$ .

Avslutningsvis tillämpas en mycket kraftfull metod för att finna stabila kristallstrukturer, som kallas slumpmässig struktursökning från ab initio. Denna teknik baseras på en enkel strategi där man systematiskt genomsöker ett stort antal slumpmässigt genererade strukturer, och där konfigurationen med den lägsta entalpin identifieras som grundtillståndet. I kapitel 5 undersöks grundtillståndsstrukturer för berylliumdikarbid ( $\text{BeC}_2$ ) med denna metod. Våra resultat visar att grundtillståndet för  $\text{BeC}_2$  består av ringar med fem kolatomer som sammankopplas genom ytterligare en kolatom till en repeterande kedja med Be-atomerna infångade runt omkring. Vi utökar våra studier till de alkaliska jordartsmetallernas dikarbidssystem, nämligen  $\text{MgC}_2$  till  $\text{BaC}_2$ , och ser att kristallstrukturen med lägst energi hos  $\text{MgC}_2$  är analog med den för  $\text{BeC}_2$ , medan den stabila fasen hos  $\text{CaC}_2$ ,  $\text{SrC}_2$  och  $\text{BaC}_2$  har den, i dessa system, vanligt förekommande kedjestrukturen.



# Acknowledgements

First of all, I would like to thank my supervisor, Professor Rajeev Ahuja for giving me the opportunity to study in Division of Materials Theory. I am deeply grateful to Rajeev for all of his encouragements, kindness and continuous supports throughout my study. Acknowledgement also goes to Associate Professor Udomsilp Pinsook of Chulalongkorn University for fruitful collaborations, useful ideas and thought-provoking discussion. In addition, special thanks to him for introducing me to Rajeev paving the way for me to be part of this prestigious research group. Most importantly, the Royal Thai Government Scholarship is the crucial part in continuous financial support for me to complete this study.

Very special thanks directly go to my brilliant colleagues and best friends: Ralph. H Scheicher, C. Moysés Araújo and Andreas Blomqvist. Ralph, thank you very much for productive collaborations and generosity especially for being always nice, kind and friendly to me. I never hesitate to go to him whenever I have any problems. Moysés, whom I have great appreciation to work with. Thank you very much for superb discussion and suggestions. Anden, thank you so much for such fruitful ideas from him. He is always ready to help me with smile. I can not forget to thank Ralph, Moysés and Anden again for reading and providing valuable comments on the thesis.

During my PhD study, several special thanks are to be mentioned here with pleasure and gratitude: to Zhimei for teaching me to learn VASP, to Duck Young for friendship and tasty homemade Gim-Bahp, to Love and Moysés for helping me during the first stage of my study, and to Fredrik Silvearv and Peter Larsson for translating the Swedish summary. Cordially thanks to my friends at the Division of Materials Theory: Pooja, Yunsuk, Diana, Johan, Jailton, Karel, Peter (L), Fredrik (S), Wei, Cecelia and others.

My student life in Uppsala would have been lonely if I had not met such wonderful friends. I would like to express my sincerest gratitude to P' Jeab and Pum for their meaningful friendship and all the hands they have been offering to me, as well as for entertaining with relaxing chats over lunchtime for the past four years. From the bottom of my heart, let me say "khob khun mak mak krub" to P' Jate, P' Joy, R Slil, R Tassanee, P' Jang, P' On and others for your kindness and super-delicious food at different occasions. Thanks to P' Ping for introducing me to the world of Python. I would like to thank all Thai friends in Uppsala: Jum, Jub, Alin, A, Aom, Fiat, M, Coam and Noina for fulfilling my life in Uppsala with pleasure and joy.

Last, but not least, I would like to thank my family for the warmest supporting me all the time.

# Bibliography

- [1] L. Schlapbach and A. Züttel. Hydrogen-storage materials for mobile applications. *Nature*, 414:353–358, 2001.
- [2] J. Graetz. New approaches to hydrogen storage. *Chem. Soc. Rev.*, 38:73–82, 2009.
- [3] K. L. Lim, H. Kazemian, Z. Yaakob, and W. R. Wan Daud. Solid-state materials and methods for hydrogen storage: A critical review. *Chem. Eng. Technol.*, 33:213–226, 2010.
- [4] R. B. Gupta (Ed). *Hydrogen Fuel: Production, Transport, and Storage*. CRC Press, Taylor & Francis Group, Boca Raton, 2009.
- [5] A. Züttel, A. Borgschulte, and L. Schlapbach (Ed). *Hydrogen as a Future Energy Carrier*. Wiley-VCH Verlag GmbH & Co. KGaA, Weinheim, 2008.
- [6] R. A. Varin, T. Czujko, and Z. S. Wronski. *Nanomaterials for Solid State Hydrogen Storage*. Springer, New York, 2009.
- [7] A. Züttel. Materials for hydrogen storage. *Mater. Today*, 6:24–33, 2003.
- [8] <http://www.almc.army.mil/alog/issues/MayJun00/MS492.htm>.
- [9] M. Fichtner. Nanotechnological aspects in materials for hydrogen storage. *Adv. Eng. Mater.*, 7:443–455, 2005.
- [10] Van der Waal Force [http://en.wikipedia.org/wiki/Van\\_der\\_Waals\\_force](http://en.wikipedia.org/wiki/Van_der_Waals_force).
- [11] N. L. Rosi, J. Eckert, M. Eddaoudi, D. T. Vodak, J. Kim, M. O’Keeffe, and O. M. Yaghi. Hydrogen storage in microporous metal-organic frameworks. *Science*, 300:1127–1129, 2003.
- [12] A. P. Côté, A. I. Benin, N. W. Ockwig, M. O’Keeffe, A. J. Matzger, and O. M. Yaghi. Porous, crystalline, covalent organic frameworks. *Science*, 310:1166–1170, 2005.
- [13] P. Srepusharawoot, R. H. Scheicher, C. Moysés Araújo, A. Blomqvist, U. Pinsook, and R. Ahuja. Ab initio study of molecular hydrogen adsorption in covalent organic framework-1. *J. Phys. Chem. C*, 113:8498–8504, 2009.

- [14] A. C. Dillon, K. M. Jones, T. A. Bekkedahl, C. H. Kiang, D. S. Bethune, and M. J. Heben. Storage of hydrogen in single-walled carbon nanotubes. *Nature*, 386:377–379, 1997.
- [15] K. P. Prasanth, R. S. Pillai, H. C. Bajaj, R. V. Jasra, H. D. Chung, T. H. Kim, and S. D. Song. Adsorption of hydrogen in nickel and rhodium exchanged zeolite X. *Int. J. Hydrogen Energy*, 33:735–745, 2008.
- [16] A. Blomqvist, C. Moysés Araújo, P. Srepusharawoot, and R. Ahuja. Li-decorated metal-organic framework 5: A route to achieving a suitable hydrogen storage medium. *Proc. Nat. Acad. Sci. U.S.A.*, 104:20173–20176, 2007.
- [17] Q. Sun, P. Jena, Q. Wang, and M. Marquez. First-principles study of hydrogen storage on  $\text{Li}_{12}\text{C}_{60}$ . *J. Am. Chem. Soc.*, 128:9741–9745, 2006.
- [18] J. L. C. Rowsell and O. M. Yaghi. Strategies for hydrogen storage in metal-organic frameworks. *Angew. Chem. Int. Ed.*, 44:4670–4679, 2005.
- [19] L. Wang and R. T. Yang. New sorbents for hydrogen storage by hydrogen spillover – A review. *Energy Environ. Sci.*, 1:268–279, 2008.
- [20] B. Bogdanović and M. Schwickardi. Ti-doped alkali metal aluminium hydrides as potential novel reversible hydrogen storage materials. *J. Alloys Compd.*, 253-254:1–9, 1997.
- [21] V. Bhat, A. Rougier, L. Aymard, G. Nazri, and J. Tarascon. Enhanced hydrogen storage property of magnesium hydride by high surface area Raney nickel. *Int. J. Hydrogen Energy*, 32:4900–4906, 2007.
- [22] C. Moysés Araújo, R. Ahuja, J. M. Osorio Guillén, and P. Jena. Role of titanium in hydrogen desorption in crystalline sodium alanate. *Appl. Phys. Lett.*, 86:251913, 2005.
- [23] J. K. Kang, J. Y. Lee, R. P. Muller, and W. A. Goddard III. Hydrogen storage in  $\text{LiAlH}_4$ : Predictions of the crystal structures and reaction mechanisms of intermediate phases from quantum mechanics. *J. Chem. Phys.*, 121:10623–10633, 2004.
- [24] J. F. Mao, Z. Wu, T. J. Chen, B. C. Weng, N. X. Xu, T. S. Huang, Z. P. Guo, H. K. Liu, D. M. Grant, G. S. Walker, and X. B. Yu. Improved hydrogen storage of  $\text{LiBH}_4$  catalyzed magnesium. *J. Phys. Chem. C*, 111:12495–12498, 2007.
- [25] J. K. Kang, S. Y. Kim, Y. S. Han, R. P. Muller, and W. A. Goddard III. A candidate  $\text{LiBH}_4$  for hydrogen storage: Crystal structures and reaction mechanisms of intermediate phases. *Appl. Phys. Lett.*, 87:111904, 2005.
- [26] P. Chen, Z. Xiong, J. Luo, J. Lin, and K. L. Tan. Interaction of hydrogen with metal nitrides and imides. *Nature*, 420:302–304, 2002.
- [27] F. H. Stillinger. Exponential multiplicity of inherent structures. *Phys. Rev. E*, 59:48–51, 1999.



- [28] C. J. Pickard and R. J. Needs. High-Pressure phases of silane. *Phys. Rev. Lett.*, 97:045504, 2006.
- [29] C. J. Pickard and R. J. Needs. Structure of phase III of solid hydrogen. *Nat. Phys.*, 3:473–476, 2007.
- [30] C. J. Pickard and R. J. Needs. Highly compressed ammonia forms an ionic crystal. *Nat. Mater.*, 7:775–779, 2008.
- [31] C. J. Pickard and R. J. Needs. When is H<sub>2</sub>O not water? *J. Chem. Phys.*, 127:244503, 2007.
- [32] C. J. Pickard and R. J. Needs. High-Pressure phases of nitrogen. *Phys. Rev. Lett.*, 102:125702, 2009.
- [33] G. Csányi, C. J. Pickard, B. D. Simons, and R. J. Needs. Graphite intercalation compounds under pressure: A first-principles density functional theory study. *Phys. Rev. B*, 75:085432, 2007.
- [34] J. Feng, R. G. Hennig, N. W. Ashcroft, and R. Hoffmann. Emergent reduction of electronic state dimensionality in dense ordered Li-Be alloys. *Nature*, 451:445–448, 2008.
- [35] G. I. G. Griffiths, R. J. Needs, and C. J. Pickard. Post-cotunnite phase of TeO<sub>2</sub> obtained from first-principles density-functional theory methods with random-structure searching. *Phys. Rev. B*, 80:184115, 2009.
- [36] C. J. Pickard and R. J. Needs. Stable phases of iron at terapascal pressures. *J. Phys. Condens. Matter*, 21:452205, 2009.
- [37] A. Szabo and N. S. Ostlund. *Modern Quantum Chemistry: Introduction to advanced electronic structure theory*. Dover Publications, Inc., New York, 1996.
- [38] P. Hohenberg and W. Kohn. Inhomogeneous electron gas. *Phys. Rev.*, 136:B864–B871, 1964.
- [39] W. Kohn and L. J. Sham. Self-consistent equations including exchange and correlation effects. *Phys. Rev.*, 140:A1133–A1138, 1965.
- [40] R. M. Martin. *Electronic Structure: Basic Theory and Practical Methods*. Cambridge University Press, Cambridge, 2004.
- [41] D. M. Ceperley and B. J. Alder. Ground state of the electron gas by a stochastic method. *Phys. Rev. Lett.*, 45:566–569, 1980.
- [42] J. P. Perdew and Y. Wang. Accurate and simple analytic representation of the electron-gas correlation energy. *Phys. Rev. B*, 45:13244–13249, 1992.
- [43] J. P. Perdew, K. Burke, and M. Ernzerhof. Generalized gradient approximation made simple. *Phys. Rev. Lett.*, 77:3865–3868, 1996.

- [44] Y. Zhang and W. Yang. Comment on generalized gradient approximation made simple. *Phys. Rev. Lett.*, 80:890, 1998.
- [45] J. P. Perdew, A. Ruzsinszky, G. I. Csonka, O. A. Vydrov, G. E. Scuseria, L. A. Constantin, X. Zhou, and K. Burke. Restoring the density-gradient expansion for exchange in solids and surfaces. *Phys. Rev. Lett.*, 100:136406, 2008.
- [46] P. Srepusharawoot, C. Moysés Araújo, A. Blomqvist, R. H. Scheicher, and R. Ahuja. A comparative investigation of H<sub>2</sub> adsorption strength in Cd- and Zn-based metal organic framework-5. *J. Chem. Phys.*, 129:164104, 2008.
- [47] W. Koch and M. C. Holthausen. *A Chemist's Guide to Density Functional Theory*. Wiley-VCH, Weinheim, 2001.
- [48] K. Kim and K. D. Jordan. Comparison of density functional and MP2 calculations on the water monomer and dimer. *J. Phys. Chem.*, 98:10089–10094, 1994.
- [49] P. J. Stephens F. J. Devlin C. F. Chabalowski and M. J. Frisch. Ab initio calculation of vibrational absorption and circular dichroism spectra using density functional force fields. *J. Phys. Chem.*, 98:11623–11627, 1994.
- [50] W. H. Press, S. A. Teukolsky, W. T. Vetterling, and B. P. Flannery. *Numerical Recipes in C: The Art of Scientific Computing*. Cambridge University Press, Cambridge, 1992.
- [51] C. Kittel. *Introduction to Solid State Physics: 8<sup>th</sup> edition*. John Wiley & Sons, USA, 2005.
- [52] P. E. Blöchl. Projector augmented-wave method. *Phys. Rev. B*, 50:17953–17979, 1994.
- [53] S. Yip (Ed). *Handbook of Materials Modeling: Chapter 1*. Springer, Dordrecht, 2005.
- [54] M. W. Finnis and J. E. Sinclair. A simple empirical N-body potential for transition-metals. *Philos. Mag. A*, 50:45–55, 1984.
- [55] J. Tersoff. Modeling solid-state chemistry: Interatomic potentials for multi-component systems. *Phys. Rev. B*, 39:5566–5568, 1989.
- [56] J. D. Kubicki and A. C. Lasaga. Molecular dynamics simulations of SiO<sub>2</sub> melt and glass: Ionic and covalent models. *Am. Mineral.*, 73:941–955, 1988.
- [57] S-N. Luo, L. Zheng, and O. Tschauner. Solid-state disordering and melting of silica stishovite: the role of defects. *J. Phys. Condens. Matter*, 18:659–668, 2006.
- [58] M. Durandurdu and D. A. Drabold. Pressure-induced structural phase transition of paracrystalline silicon. *Phys. Rev. B.*, 66:205204, 2002.

- [59] D. Hohl and R. O. Jones. Polymerization in liquid phosphorus: Simulation of a phase transition. *Phys. Rev. B.*, 50:17047–17053, 1994.
- [60] T. Mueller and G. Ceder. A density functional theory study of hydrogen adsorption in MOF-5. *J. Phys. Chem. B*, 109:17974–17983, 2005.
- [61] F. Jensen. *Introduction to Computational Chemistry: 2<sup>nd</sup> edition*. John Wiley & Sons, Chichester, 2007.
- [62] M. G. Nijkamp, J. E. M. J. Raaymakers, A. J. van Dillen, and K.P. de Jong. Hydrogen storage using physisorption - materials demands. *Appl. Phys. A*, 72:619–623, 2001.
- [63] [http://www1.eere.energy.gov/hydrogenandfuelcells/storage/pdfs/targets\\_onboard\\_hydro\\_storage.pdf](http://www1.eere.energy.gov/hydrogenandfuelcells/storage/pdfs/targets_onboard_hydro_storage.pdf).
- [64] J. Yang, A. Sudik, C. Wolverton, and D. J. Siegel. High capacity hydrogen storage materials: attributes for automotive applications and techniques for materials discovery. *Chem. Soc. Rev.*, 39:656–675, 2010.
- [65] V. Bérubé, G. Radtke, M. Dresselhaus, and G. Chen. Size effects on the hydrogen storage properties of nanostructured metal hydrides: A review. *Int. J. Energy Res.*, 31:637–663, 2007.
- [66] C. Liu, Y. Y. Fan, M. Liu, H. T. Cong, H. M. Cheng, and M. S. Dresselhaus. Hydrogen storage in single-walled carbon nanotubes at room temperature. *Science*, 286:1127–1129, 1999.
- [67] V. Meregalli and M. Parrinello. Review of theoretical calculations of hydrogen storage in carbon-based materials. *Appl. Phys. A*, 72:143–146, 2001.
- [68] R. H. Baughman, A. A. Zakhidov, and W. A. de Heer. Carbon nanotubes—the route toward applications. *Science*, 297:787–792, 2002.
- [69] T. Yildirim and M. R. Hartman. Direct observation of hydrogen adsorption sites and nanocage formation in metal-organic frameworks. *Phys. Rev. Lett.*, 95:215504, 2005.
- [70] L. J. Murray, M. Dinçă, and J. R. Long. Hydrogen storage in metal-organic frameworks. *Chem. Soc. Rev.*, 38:1294–1314, 2009.
- [71] J. L. C. Rowsell, A. R. Millward, K. S. Park, and O. M. Yaghi. Hydrogen sorption in functionalized metal-organic frameworks. *J. Am. Chem. Soc.*, 126:5666–5667, 2004.
- [72] J. L. C. Rowsell and O. M. Yaghi. Effects of functionalization, catenation, and variation of the metal oxide and organic linking units on the low-pressure hydrogen adsorption properties of metal-organic frameworks. *J. Am. Chem. Soc.*, 128:1304–1315, 2006.

- [73] D. Cao, J. Lan, W. Wang, and B. Smit. Lithium-doped 3D covalent organic frameworks: High-capacity hydrogen storage materials. *Angew. Chem. Int. Ed.*, 48:4730–4733, 2009.
- [74] E. Klontzas, E. Tylianakis, and G. E. Froudakis. Designing 3D COFs with enhanced hydrogen storage capacity. *Nano Lett.*, 10:452–454, 2010.
- [75] B. Assfour and G. Seifert. Hydrogen adsorption sites and energies in 2D and 3D covalent organic frameworks. *Chem. Phys. Lett.*, 489:86–91, 2010.
- [76] F. Li, J. Zhao, B. Johansson, and L. Sun. Improving hydrogen storage properties of covalent organic frameworks by substitutional doping. *Int. J. Hydrogen Energy*, 35:266–271, 2010.
- [77] S. S. Han, H. Furukawa, O. M. Yaghi, and W. A. Goddard III. Covalent organic frameworks as exceptional hydrogen storage materials. *J. Am. Chem. Soc.*, 130:11580–11581, 2008.
- [78] J. Weitkamp, M. Fritz, and S. Ernst. Zeolites as media for hydrogen storage. *Int. J. Hydrogen Energy*, 20:967–970, 1995.
- [79] H. W. Langmi, A. Walton, M. M. Al-Mamouri, S. R. Johnson, D. Book, J. D. Speight, P. P. Edwards, I. Gameson, P.A. Anderson, and I.R. Harris. Hydrogen adsorption in zeolites A, X, Y and RHO. *J. Alloys Compd.*, 356-357:710–715, 2003.
- [80] Z. Yang, Y. Xia, and R. Mokaya. Enhanced hydrogen storage capacity of high surface area Zeolite-like carbon materials. *J. Am. Chem. Soc.*, 129:1673–1679, 2007.
- [81] Y. Liu, H. Liu, Y. Hu, and J. Jiang. Development of a density functional theory in three-dimensional nanoconfined space: H<sub>2</sub> storage in metal-organic frameworks. *J. Phys. Chem. B*, 113:12326–12331, 2009.
- [82] M. Zhou, Q. Wang, L. Zhang, Y. Liu, and Y. Kang. Adsorption sites of hydrogen in zeolitic imidazolate frameworks. *J. Phys. Chem. B*, 113:11049–11053, 2009.
- [83] R. B. Rankin, J. Liu, A. D. Kulkarni, and J. K. Johnson. Adsorption and diffusion of light gases in ZIF-68 and ZIF-70: A simulation study. *J. Phys. Chem. C*, 113:16906–16914, 2009.
- [84] H. Jin, Y. S. Lee, and I. Hong. Hydrogen adsorption characteristics of activated carbon. *Catal. Today*, 120:399–406, 2007.
- [85] F. Darkrim and D. Levesque. High adsorptive property of opened carbon nanotubes at 77 K. *J. Phys. Chem. B*, 104:6773–6776, 2000.
- [86] Y. Ye, C. C. Ahn, C. Witham, B. Fultz, J. Liu, A. G. Rinzler, D. Colbert, K. A. Smith, and R. E. Smalley. Hydrogen adsorption and cohesive energy of single-walled carbon nanotubes. *Appl. Phys. Lett.*, 74:2307–2309, 1999.

- [87] F. L. Darkrim, P. Malbrunot, and G. P. Tartaglia. Review of hydrogen storage by adsorption in carbon nanotubes. *Int. J. Hydrogen Energy*, 27:193–202, 2002.
- [88] D. J. Tranchemontagne, J. L. Mendoza-Cortés, M. O’Keeffe, and O. M. Yaghi. Secondary building units, nets and bonding in the chemistry of metal-organic frameworks. *Chem. Soc. Rev.*, 38:1257–1283, 2009.
- [89] Y. Li, L. Xie, Y. Liu, R. Yang, and X. Li. Favorable hydrogen storage properties of M(HBTC)(4,4’-bipy)·3DMF (M = Ni and Co). *Inorg. Chem.*, 47:10372–10377, 2008.
- [90] A. G. Wong-Foy, A. J. Matzger, and O. M. Yaghi. Exceptional H<sub>2</sub> saturation uptake in microporous metal-organic frameworks. *J. Am. Chem. Soc.*, 128:3494–3495, 2006.
- [91] L. Pan, M. B. Sander, X. Huang, J. Li, M. Smith, E. Bittner, B. Bockrath, and J. K. Johnson. Microporous metal organic materials: Promising candidates as sorbents for hydrogen storage. *J. Am. Chem. Soc.*, 126:1308–1309, 2004.
- [92] V. Krungleviciute, K. Lask, L. Heroux, A. D. Migone, J.-Y. Lee, J. Li, and A. Skoulidas. Argon adsorption on Cu<sub>3</sub>(Benzene-1,3,5-tricarboxylate)<sub>2</sub>(H<sub>2</sub>O)<sub>3</sub> metal-organic framework. *Langmuir*, 23:3106–3109, 2007.
- [93] G. Garberoglio, A. I. Skoulidas, and J. K. Johnson. Adsorption of gases in metal organic materials: Comparison of simulations and experiments. *J. Phys. Chem. B*, 109:13094–13103, 2005.
- [94] M. Eddaoudi, J. Kim, N. Rosi, D. Vodak, J. Wachter, M. O’Keeffe, and O. M. Yaghi. Systematic design of pore size and functionality in isorecticular MOFs and their application in methane storage. *Science*, 295:469–472, 2002.
- [95] B. Chen, S. Ma, F. Zapata, F. R. Fronczek, E. B. Lobkovsky, and H.-C. Zhou. Rationally designed micropores within a metal-organic framework for selective sorption of gas molecules. *Inorg. Chem.*, 46:1233–1236, 2007.
- [96] J. A. Rood, B. C. Noll, and K. W. Henderson. Synthesis, structural characterization, gas sorption and guest-exchange studies of the lightweight, porous metal-organic framework  $\alpha$ -[Mg<sub>3</sub>(O<sub>2</sub>CH)<sub>6</sub>]. *Inorg. Chem.*, 45:5521–5528, 2006.
- [97] S. Ma, D. Sun, J. M. Simmons, C. D. Collier, D. Yuan, and H.-C. Zhou. Metal-organic framework from an anthracene derivative containing nanoscopic cages exhibiting high methane uptake. *J. Am. Chem. Soc.*, 130:1012–1016, 2008.
- [98] Q. Yang and C. Zhong. Molecular simulation of carbon dioxide/methane/hydrogen mixture adsorption in metal-organic frameworks. *J. Phys. Chem. B*, 110:17776–17783, 2006.
- [99] B. Xiao, P. S. Wheatley, X. Zhao, A. J. Fletcher, S. Fox, A. G. Rossi, I. L. Megson, S. Bordiga, L. Regli, K. M. Thomas, and R. E. Morris. High-capacity hydrogen and nitric oxide adsorption and storage in a metal-organic framework. *J. Am. Chem. Soc.*, 129:1203–1209, 2007.

- [100] Y.-S. Bae, D. Dubbeldam, A. Nelson, K. S. Walton, J. T. Hupp, and R. Q. Snurr. Strategies for characterization of large-pore metal-organic frameworks by combined experimental and computational methods. *Chem. Mater.*, 21:4768–4777, 2009.
- [101] Y. Li and R. T. Yang. Hydrogen storage in metal-organic and covalent-organic frameworks by spillover. *AIChE J.*, 54:269–279, 2008.
- [102] Y. Li and R. T. Yang. Significantly enhanced hydrogen storage in metal-organic frameworks via spillover. *J. Am. Chem. Soc.*, 128:726–727, 2006.
- [103] S. S. Han and W. A. Godard III. Lithium-doped metal-organic frameworks for reversible H<sub>2</sub> storage at ambient temperature. *J. Am. Chem. Soc.*, 129:8422–8423, 2007.
- [104] K. L. Mulfort and J. T. Hupp. Chemical reduction of metal-organic framework materials as a method to enhance gas uptake and binding. *J. Am. Chem. Soc.*, 129:9604–9605, 2007.
- [105] T. Yildirim and S. Ciraci. Titanium-decorated carbon nanotubes as a potential high-capacity hydrogen storage medium. *Phys. Rev. Lett.*, 94:175501, 2005.
- [106] H. Lee, J. Ihm, M. L. Cohen, and S. G. Louie. Calcium-decorated graphene-based nanostructures for hydrogen storage. *Nano Lett.*, 10:793–798, 2010.
- [107] F. Schüth, B. Bogdanović, and M. Felderhoff. Light metal hydrides and complex hydrides for hydrogen storage. *Chem. Commun.*, pages 2249–2258, 2004.
- [108] W. Grochala and P. P. Edwards. Thermal decomposition of the non-interstitial hydrides for the storage and production of hydrogen. *Chem. Rev.*, 104:1283–1315, 2004.
- [109] A. Zaluska, L. Zaluski, and J. O. Ström-Olsen. Nanocrystalline magnesium for hydrogen storage. *J. Alloys Compd.*, 288:217–225, 1999.
- [110] A. Ibikunle, A. J. Goudy, and H. Yang. Hydrogen storage in a CaH<sub>2</sub>/LiBH<sub>4</sub> destabilized metal hydride system. *J. Alloys Compd.*, 475:110–115, 2009.
- [111] J. Chen, N. Kuriyama, Q. Xu, H. T. Takeshita, and T. Sakai. Reversible hydrogen storage via titanium-catalyzed LiAlH<sub>4</sub> and Li<sub>3</sub>AlH<sub>6</sub>. *J. Phys. Chem. B.*, 105:11214–11220, 2001.
- [112] H. Morioka, K. Kakizaki, S.-C. Chung, and A. Yamada. Reversible hydrogen decomposition of KAlH<sub>4</sub>. *J. Alloys Compd.*, 353:310–314, 2003.
- [113] A. Züttel, S. Rentsch, P. Fischer, P. Wenger, P. Sudan, Ph. Mauron, and Ch. Emmenegger. Hydrogen storage properties of LiBH<sub>4</sub>. *J. Alloys Compd.*, 356-357:515–520, 2003.
- [114] S. Orimo, Y. Nakamori, J. R. Eliseo, A. Züttel, and C. M. Jensen. Complex hydrides for hydrogen storage. *Chem. Rev.*, 107:4111–4132, 2007.

- [115] M. Polanski, T. Płociński, I. Kuncce, and J. Bystrzycki. Dynamic synthesis of ternary  $\text{Mg}_2\text{FeH}_6$ . *Int. J. Hydrogen Energy*, 35:1257–1266, 2010.
- [116] R. J. Kuppler, D. J. Timmoms, Q.-R. Fang, J.-R. Li, T. A. Makal, M. D. Young, D. Yuan, D. Zhao, W. Zhuang, and H.-C. Zhou. Potential applications of metal-organic frameworks. *Coor. Chem. Rev.*, 253:3042–3066, 2009.
- [117] O. M. Yaghi, M. O’Keeffe, N. W. Ockwig, H. K. Chae, M. Eddaoudi, and J. Kim. Reticular synthesis and the design of new materials. *Nature*, 423:705–714, 2003.
- [118] T. Sagara, J. Klassen, and E. Ganz. Computational study of hydrogen binding by metal-organic framework-5. *J. Chem. Phys.*, 121:12543–12547, 2004.
- [119] S. F. Boys and F. Bernardi. The calculation of small molecular interactions by the differences of separate total energies. Some procedures with reduced errors. *Mol. Phys.*, 19:553–566, 1970.
- [120] S. Simon, M. Duran, and J. J. Dannenberg. How does basis set superposition error change the potential surfaces for hydrogen-bonded dimers? *J. Chem. Phys.*, 105:11024–11031, 1996.
- [121] G. Henkelman, A. Arnaldsson, and H. Jónsson. A fast and robust algorithm for Bader decomposition of charge density. *Comput. Mater. Sci.*, 36:354–360, 2006.
- [122] Y. Y. Sun, K. Lee, Y.-H. Kim, and S. B. Zhang. Ab initio design of Ca-decorated organic frameworks for high capacity molecular hydrogen storage with enhanced binding. *Appl. Phys. Lett.*, 95:033109, 2009.
- [123] Q. Wang, Q. Sun, P. Jena, and Y. Kawazoe. Theoretical study of hydrogen storage in Ca-coated fullerenes. *J. Chem. Theory Comput.*, 5:374–379, 2009.
- [124] F. Nouar, J. Eckert, J. F. Eubank, P. Forster, and M. Eddaoudi. Zeolite-like metal-organic frameworks (ZMOFs) as hydrogen storage platform: Lithium and magnesium ion-exchange and  $\text{H}_2$ -(rho-ZMOF) interaction studies. *J. Am. Chem. Soc.*, 131:2864–2870, 2009.
- [125] K. S. Walton and R. Q. Snurr. Applicability of the BET method for determining surface areas of microporous metal-organic frameworks. *J. Am. Chem. Soc.*, 129:8552–8556, 2007.
- [126] S. Brunauer, P. H. Emmett, and E. Teller. Adsorption of gases in multimolecular layers. *J. Am. Chem. Soc.*, 60:309–319, 1938.
- [127] S. Kolmann, B. Chan, and M. J. T. Jordan. Modelling the interaction of molecular hydrogen with lithium-doped hydrogen storage materials. *Chem. Phys. Lett.*, 467:126–130, 2008.
- [128] Z. H. Zhu and G. Q. Lu. Comparative study of Li, Na, and K adsorptions on graphite by using ab initio method. *Langmuir*, 20:10751–10755, 2004.

- [129] G. Mpourmpakis and G. Froudakis. Why alkali metals preferably bind on structural defects of carbon nanotubes: A theoretical study by first principles. *J. Chem. Phys.*, 125:204707, 2006.
- [130] K. L. Mulfort and J. T. Hupp. Alkali metal cation effects on hydrogen uptake and binding in metal-organic frameworks. *Inorg. Chem.*, 47:7936–7938, 2008.
- [131] P. Boolchand and W. J. Bresser. Mobile silver ions and glass formation in solid electrolytes. *Nature*, 410:1070–1073, 2001.
- [132] J. W. Fergus. Ceramic and polymeric solid electrolytes for lithium-ion batteries. *J. Power Sources*, 195:4554–4569, 2010.
- [133] B. Zhu. Solid oxide fuel cell (SOFC) technical challenges and solutions from nano-aspects. *Int. J. Energy Res.*, 33:1126–1137, 2009.
- [134] S. M. Haile, C. R. I. Chisholm, K. Sasaki, D. A. Boysen, and T. Uda. Solid acid proton conductors: from laboratory curiosities to fuel cell electrolytes. *Faraday Discuss.*, 134:17–39, 2007.
- [135] R. C. Agrawal and R. K. Gupta. Superionic solids: composite electrolyte phase – an overview. *J. Mater. Sci.*, 34:1131–1162, 1999.
- [136] C. Moysés Araújo, A. Blomqvist, R. H. Scheicher, P. Chen, and R. Ahuja. Superionicity in the hydrogen storage material  $\text{Li}_2\text{NH}$ : Molecular dynamics simulations. *Phys. Rev. B*, 79:172101, 2009.
- [137] H. Maekawa, M. Matsuo, H. Takamura, M. Ando, Y. Noda, T. Karahashi, and S. Orimo. Halide-Stabilized  $\text{LiBH}_4$ , a room-temperature lithium fast-ion conductor. *J. Am. Chem. Soc.*, 131:894–895, 2009.
- [138] D. H. Gregory. Lithium nitrides, imides and amides as lightweight, reversible hydrogen stores. *J. Mater. Chem.*, 18:2321–2330, 2008.
- [139] K. Miwa, N. Ohba, S. Towata, Y. Nakamori, and S. Orimo. First-principles study on lithium amide for hydrogen storage. *Phys. Rev. B*, 71:195109, 2005.
- [140] F. E. Pinkerton. Decomposition kinetics of lithium amide for hydrogen storage materials. *J. Alloys Compd.*, 400:76–82, 2005.
- [141] G. P. Meisner, F. E. Pinkerton, M. S. Meyer, M. P. Balogh, and M. D. Kundrat. Study of the Lithium-Nitrogen-Hydrogen system. *J. Alloys Compd.*, 404-406:24–26, 2005.
- [142] T. Ichikawa, N. Hanada, S. Isobe, H. Leng, and H. Fujii. Mechanism of novel reaction from  $\text{LiNH}_2$  and  $\text{LiH}$  to  $\text{Li}_2\text{NH}$  and  $\text{H}_2$  as a promising hydrogen storage system. *J. Phys. Chem. B*, 108:7887–7892, 2004.
- [143] J. F. Herbst and L. G. Hector, Jr. Energetics of the Li amide/Li imide hydrogen storage reaction. *Phys. Rev. B*, 72:125120, 2005.



- [144] S. Orimo, Y. Nakamori, G. Kitahara, K. Miwa, N. Ohba, T. Noritake, and S. Towata. Destabilization and enhanced dehydriding reaction of  $\text{LiNH}_2$ : an electronic structure viewpoint. *Appl. Phys. A*, 79:1765–1767, 2004.
- [145] W. I. F. David, M. O. Jones, D. H. Gregory, C. M. Jewell, S. R. Johnson, A. Walton, and P. P. Edwards. A mechanism for non-stoichiometry in the lithium amide/ lithium imide hydrogen storage reaction. *J. Am. Chem. Soc.*, 129:1594–1601, 2007.
- [146] D. H. Gregory, P. M. O’Meara, A. G. Gordon, J. P. Hodges, S. Short, and J. D. Jorgensen. Structure of lithium nitride and transition-metal-doped derivatives,  $\text{Li}_{3-x-y}\text{M}_x\text{N}$  ( $\text{M} = \text{Ni}, \text{Cu}$ ): A Powder Neutron Diffraction Study. *Chem. Mater.*, 14:2063–2070, 2002.
- [147] M. H. Sørby, Y. Nakamura, H. W. Brinks, T. Ichikawa, S. Hino, H. Fujii, and B. C. Hauback. The crystal structure of  $\text{LiND}_2$  and  $\text{Mg(ND}_2)_2$ . *J. Alloys Compd.*, 428:297–301, 2007.
- [148] P. Chen, Z. Xiong, J. Luo, J. Lin, and K. L. Tan. Interaction between lithium amide and lithium hydride. *J. Phys. Chem. B*, 107:10967–10970, 2003.
- [149] G. Miceli, C. S. Cucinotta, M. Bernasconi, and M. Parrinello. First principle study of the  $\text{LiNH}_2 / \text{Li}_2\text{NH}$  transformation. *J. Phys. Chem. C*, 114:15174–15183, 2010.
- [150] N. Agmon. The Grotthuss mechanism. *Chem. Phys. Lett.*, 244:456–462, 1995.
- [151] Y. H. Hu and E. Ruckenstein. Ultrafast reaction between  $\text{LiH}$  and  $\text{NH}_3$  during  $\text{H}_2$  storage in  $\text{Li}_3\text{N}$ . *J. Phys. Chem. A*, 107:9737–9739, 2003.
- [152] T. Kar, S. Scheiner, and L. Li. Theoretical investigation on the mechanism of  $\text{LiH} + \text{NH}_3 \rightarrow \text{LiNH}_2 + \text{H}_2$  reaction. *J. Mol. Struct. THEOCHEM*, 857:111–114, 2008.
- [153] S. M. Woodley and R. Catlow. Crystal structure prediction from first principles. *Nat. Mater.*, 7:937–946, 2008.
- [154] M. I. Eremets, I. A. Trojan, S. A. Medvedev, J. S. Tse, and Y. Yao. Superconductivity in hydrogen dominant materials: Silane. *Science*, 319:1506–1509, 2008.
- [155] A. J. Morris, C. J. Pickard, and R. J. Needs. Hydrogen/nitrogen/oxygen defect complexes in silicon from computational searches. *Phys. Rev. B*, 80:144112, 2009.
- [156] P. Zaleski-Ejgierd, M. Hakala, and P. Pyykkö. Comparison of chain versus sheet crystal structures for the cyanides  $\text{MCN}$  ( $\text{M}=\text{Cu-Au}$ ) and dicarbides  $\text{MC}_2$  ( $\text{M}=\text{Be-Ba}, \text{Zn-Hg}$ ). *Phys. Rev. B*, 76:094104, 2007.
- [157] S. Patchkovskii, J. S. Tse, S. N. Yurchenko, L. Zhechkov, T. Heine, and G. Seifert. Graphene nanostructures as tunable storage media for molecular hydrogen. *Proc. Nat. Acad. Sci. U.S.A.*, 102:10439–10444, 2005.

- [158] Y. Okamoto and Y. Miyamoto. Ab initio investigation of physisorption of molecular hydrogen on planar and curved graphenes. *J. Phys. Chem. B*, 105:3470–3474, 2001.
- [159] U. Ruschewitz. Binary and ternary carbides of alkali and alkaline-earth metals. *Coord. Chem. Rev.*, 244:115–136, 2003.
- [160] B. Xiao, J. Feng, J. C. Chen, and L. Yu. Crystal structures and electronic properties of  $MC_2$  ( $M = \text{Mg, Ca, Sr, Ba}$ ) by comparative studies based on ab-initio calculations. *Chem. Phys. Lett.*, 448:35–40, 2007.
- [161] P. Karen, A. Kjekshus, Q. Huang, and V. L. Karen. The crystal structure of magnesium dicarbide. *J. Alloys Compd.*, 282:72–75, 1999.
- [162] M. Atoji and R. C. Medrud. Structures of calcium dicarbide and uranium dicarbide by neutron diffraction. *J. Chem. Phys.*, 31:332–337, 1959.
- [163] E. Ruiz and P. Alemany. Electronic structure and bonding in  $\text{CaC}_2$ . *J. Phys. Chem.*, 99:3114–3119, 1995.
- [164] O. Reckeweg, A. Baumann, H. A. Meyer, J. Glaser, and H-J. Meyer. On the coexistence of tetragonal and monoclinic  $\text{CaC}_2$ : structural and spectroscopic studies on alkaline earth metal acetylides,  $MC_2$  ( $M = \text{Ca, Sr, Ba}$ ). *Z. Anorg. Allg. Chem.*, 625:1686–1692, 1999.
- [165] V. Vohn, W. Kockelmann, and U. Ruschewitz. On the synthesis and crystal structure of  $\text{BaC}_2$ . *J. Alloys Compd.*, 284:132–137, 1999.



# Acta Universitatis Upsaliensis

*Digital Comprehensive Summaries of Uppsala Dissertations  
from the Faculty of Science and Technology 712*

Editor: The Dean of the Faculty of Science and Technology

A doctoral dissertation from the Faculty of Science and Technology, Uppsala University, is usually a summary of a number of papers. A few copies of the complete dissertation are kept at major Swedish research libraries, while the summary alone is distributed internationally through the series Digital Comprehensive Summaries of Uppsala Dissertations from the Faculty of Science and Technology. (Prior to January, 2005, the series was published under the title “Comprehensive Summaries of Uppsala Dissertations from the Faculty of Science and Technology”.)



ACTA  
UNIVERSITATIS  
UPSALIENSIS  
UPPSALA  
2010

Distribution: [publications.uu.se](http://publications.uu.se)  
urn:nbn:se:uu:diva-132875